2015

Processing and Interpretation of Three-Component Borehole/Surface Seismic Data over Gabor Gas Storage Field

Li Wei

Wright State University

Repository Citation

Wei, Li, "Processing and Interpretation of Three-Component Borehole/Surface Seismic Data over Gabor Gas Storage Field" (2015). *Browse all Theses and Dissertations*. 1587.
https://corescholar.libraries.wright.edu/etd_all/1587

PROCESSING AND INTERPRETATION OF THREE-COMPONENT BOREHOLE/SURFACE SEISMIC DATA OVER GABOR GAS STOTAGE FIELD

A thesis submitted in partial fulfillment of the
requirements for the degree of
Master of Science

By

LI WEI
M.S., Taiyuan University of Technology 2013
B.S., Taiyuan University of Technology 2011

2015
Wright State University

WRIGHT STATE UNIVERSITY

GRADUATE SCHOOL

August 31, 2015

I HEREBY RECOMMEND THAT THE THESIS PREPARED UNDER MY SUPERVISION BY Li Wei ENTITLED Processing and Interpretation of Three-Component Borehole/Surface Seismic Data over Gabor Gas Storage Field BE ACCEPTED IN PARTIAL FULFILLMENT OF THE REQUIREMENTS FOR THE DEGREE OF Master of Science

____

Ernest Hauser, Ph.D.
Thesis Director

____

David Dominic, Ph.D.
Department Chair

Committee on
Final Examination

____

Ernest Hauser, Ph.D.

____

Doyle Watts, Ph.D.

____

David Dominic, Ph.D.

____

Robert E. W. Fyffe, Ph.D.
Vice President For Research and
Dean of the Graduate School

ABSTRACT

Wei, Li. M.S. Department of Earth and Environmental Sciences, Wright State University, 2015. Processing and Interpretation of Three-Component Borehole/Surface Seismic Data over Gabor Gas Storage Field.

Analysis of a seismic dataset recorded as part of a collaborative project between Wright State University, Spectraseis, Precision Geophysical, and Dominion East Ohio over the Gabor gas storage field, Canton, Ohio, is the topic of this study. Two types of sources (vibroseis and small seismic shot-holes) as well as three types of recording systems (passive 3C broadband on the surface, experimental 3C borehole sondes, and conventional 2D surface geophone profiles) were employed with different purposes. The shot hole explosives were calibration check-shots for the 3C borehole array repeatedly deployed at multiple levels. The vibrators of the conventional 2D seismic profiles were also recorded with the borehole array, a series of 3C surface seismometers along the 2D seismic lines and a spiral array of 3C seismometers centered at the wellhead. Processed and migrated seismic data from the pair of 2D surface seismic lines crossing directly over the well location were provided by Tom McGovern of Seismic Earth Resources Technology. The particular aims of this project are to determine wave velocities from first breaks, to apply VSP processing procedures on the borehole data, and to analyze spectral attributes in the low frequency range from a beat-sweep test.

This VSP study was attempted despite the fact that the data were not collected for that purpose, and unfortunately the analysis of the borehole data failed to show expected subsurface reflectors. The raw borehole records have many characteristics unique to the borehole environment, which include effects of poor geophone clamping, bad cementation and tube waves. A frequency filter combined with trace mutes was very effective in enhancing wanted events as well as improving wave shapes. Time shifts between successive traces were obtained through cross-correlation. The true wave velocities were determined based on a single layer model, and were compared to the stacking velocities obtained from surface-recorded seismic data. Several VSP processing procedures were applied attempting to track up-going reflections from the borehole records, including static time shifting, FK filtering, NMO correction, and trace stacking. The stacked VSP trace was tied to surface seismic section, however, showed poor correlation in terms of subsurface horizons.

Data from a beat-sweep test was also analyzed with the hope of verifying a low frequency spectral anomaly over the gas field. During the beat sweep tests and for minutes afterward the phenomenon of distinctly increased amplitude at 3Hz was present in both surface and borehole measurements. This beat-sweep test survey provided a tantalizing first look at a way of generating low frequency seismic energy to examine the low frequency anomaly over hydrocarbon reservoirs, and in this case successfully verified the production of a 3Hz anomaly.

TABLE OF CONTENTS

LIST OF FIGURES

LIST OF TABLES

LIST OF EQATIONS

I Introduction

The three-component (3C) seismic survey was performed in a borehole and at surface over the Gabor Gas storage field. The borehole survey not only served the initial purpose of providing the field-worthiness of the new multilevel tool, but also provided comprehensive datasets that enabled seismic wave analysis and spectral attributes analysis over the hydrocarbon reservoir. The 3C borehole survey was conducted using different types of sources including dynamite and vibrators. Noises unique to borehole environment were found in the raw data to be related with the effects of casing, cementation, and tubing dominated noises. Distinct source-receiver arrays prompt distinct processing methods to be used on the data. Surface data was recorded in a spiral array centered at the wellhead and will be only processed for spectral attributes analysis.

Geology of Survey Location

Geology History

The 3C seismic survey was carried on in northeastern Ohio (Figure 1). The earliest record of the geological history of northeastern Ohio is preserved in the Precambrian rocks of the deep subsurface at more than 1 billion years old. By Late Cambrian time, shallow seas covered Ohio and sediments were deposited and preserved, beginning a record of mainly marine and deltaic deposition, interrupted by periods of erosion, which lasted until Early Permian time. Non-marine deposition was intermittently common in the Pennsylvanian and Permian periods. In Late Paleozoic time, North America was part of a northern landmass called Laurasia, which collided with a southern landmass called Gondwana to form the supercontinent of Pangea. Laurasia and Gondwana broke up in the Mesozoic, and the plates separated to create the Atlantic Ocean and the Gulf of Mexico. The area of Ohio remained high and dry, undergoing erosion for most of the past 245 million years of Earth history. The next substantial record is preserved as glacial deposits at the surface of Ohio (Coogan 1996).

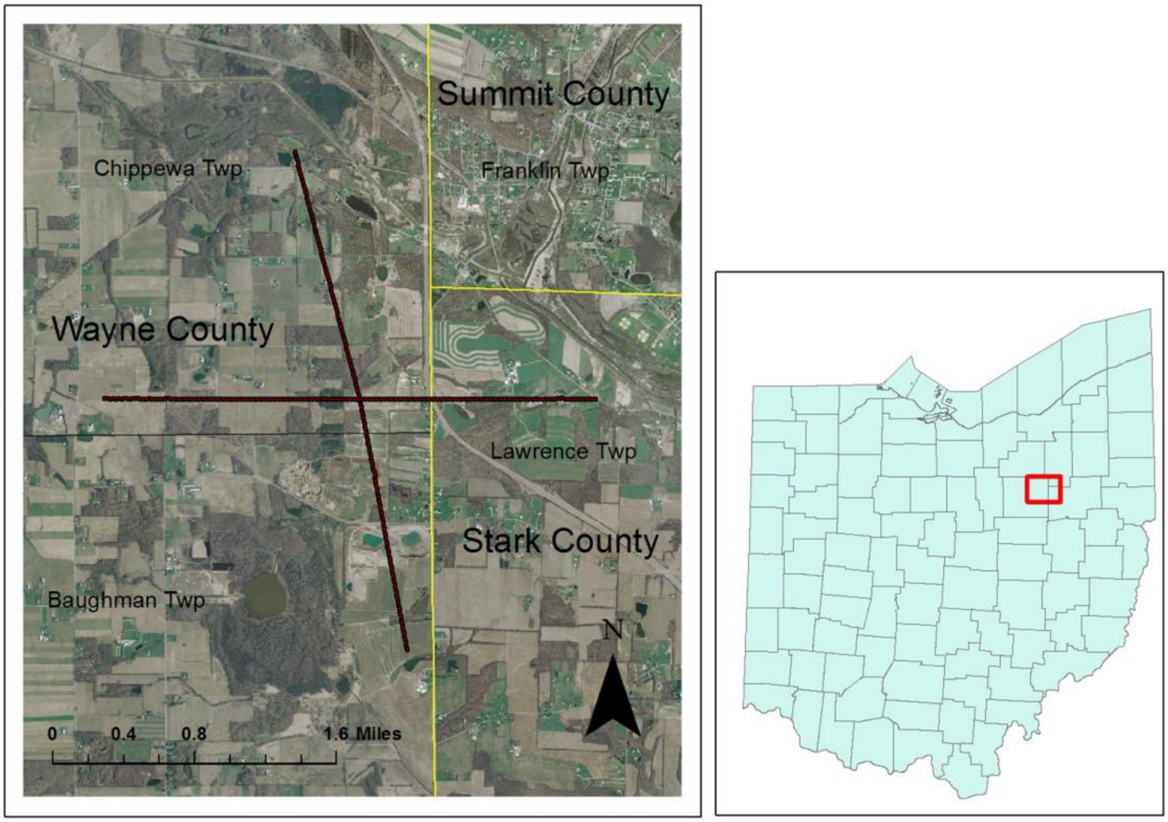

Figure 1: Location map of the study area. The borehole is located at the center of the two crossing surface seismic lines.

Sedimentary Strata

The following table (Table 1) gives a brief classification of the sedimentary strata of a gas storage well that was 10m away from the monitoring borehole used for the borehole sonde tests, and includes the name and character of the chief subdivisions, the thickness, and the terms in general use by the well driller. Many of the details of the classification have been omitted for clarity.

Table 1: Generalized section of rocks penetrated in well API: 3416921788.

SYSTEM	FORMATION	DRILLERS NAME	TOP (ft)	BASE (ft)	THICKNESS (ft)	CHARACTER
Quaternary	Glacial	Sand and Gravel	0	572	572	Boulder, clay, sand, pebbles
Mississippian	Logan and Cuyahoga	Shale and Sandstone				Dark shale with sandstone
	Sunbury					
	Berea sandstone	Berea	572	637	65	Medium grained sandstone
	Bedford shale	Ohio shale	637	2297	1660	Black and brown shale
Devonian	Ohio shale					
	Delaware Limestone	Big Lime	2297	3643	1346	Limestone-salt-Dolomite
	Columbus Limestone					
Silurian	Monroe					
	Salina fm					
	Niagara fm					
	Brassfield lm					
	Medina fm	Packer Shell	3643	3763	120	Dolomite
		Clinton Sand	3763	3863	100	Grey or red sandstone
		Medina Red Rock	3863	?	?	Drilling stopped

The Clinton Interval from 3763ft (1147m) to 3863ft (1177m) is the hydrocarbon reservoir from which the oil and gas are produced in largest quantities in the area. This interval is a Lower Silurian deltaic deposit composed of interbedded sandstone and shale. The color of the Clinton is gray to reddish and the thickness is as much as 100ft (30m). It was deposited on the distal flank of the Appalachian basin as a result of the Taconic orogeny. The section extends vertically from the Queenstone unconformity to the base of the upper Dayton Formation, referred to by driller's as the "Packer Shell". The Packer Shell, so-called because the drillers generally use this hard unit as a seat for casing or production tubing, is a medium to coarsely crystalline limestone or magnesium limestone containing some interbedded greenish-grey shale that serve as the cap rock to seal the Clinton reservoir.

The “Big Lime” is a term applied by the driller to the great thickness of limestone which occurs everywhere in the field under the Ohio shale. It includes gray, blue, and brown limestone that in the middle portion includes dolomite and salt, whereas the upper and lower portions are low in magnesium. The Big Lime includes both late Devonian and early Silurian strata and comprises the Delaware and Columbus limestones, the Detroit River and Bass Island dolomites and the Niagara dolomites. Overlying the Big Lime is 1660ft (506m) of shale varying in color from black to brown, red and gray, which is known to drillers as the Ohio Shale.

The Berea Sandstone is one of the best-known horizons in eastern Ohio and composed of Mississippian sandstone. Although seldom more than 65ft (20m) in thickness, it is a very regionally persistent formation and is used as a key rock interval for drillers over a large area. The Berea sandstone is a medium-to-fine grained gray rock that was deposited above the Bedford shale, at first subaerially as a delta and later as a marine pavement that formed as the sea inundated this delta. The Bedford shale was deposited in part subaerially upon a delta and in part subaqueously as offshore beds along the delta front. The Bedford and Berea formations, therefore, represent a cycle of deposition during an oscillation of the land and sea between two periods of quiescence (Conrey 1921).

Overlying the Berea sandstone is a succession of black, blue and gray shale and gray sandstone of Mississippian age, which the driller usually simply describes as Shale and Sandstone. Locally, the total thickness of the rocks overlying the Berea including the covering of glacial drift is 572ft (174m).

Seismic Expression of Strata

Figure 2 is a migrated seismic section measured at two surface lines crossing over the borehole location with receiver spacing of 82.5ft (25m) and vibroseis sources every 165ft (50m). The borehole array in green and a gamma ray log in red are both plotted at the correct positions. The borehole array was deployed from ~364ft (111m) below the surface at a various spacing which penetrated from base of the glacial tills through Berea sandstone, Bedford shale, till the upper part of the Big Lime. The Clinton Interval is ~1000ft (305m) below the bottom of the borehole array. The top of the Big Lime and the Clinton Interval are labeled on the seismic section as strong reflection horizons. Another strong reflection horizon at 3200ft (975m) in depth is the top of Packer Shell. Migrated seismic section also indicates little dip in the vicinity of borehole.

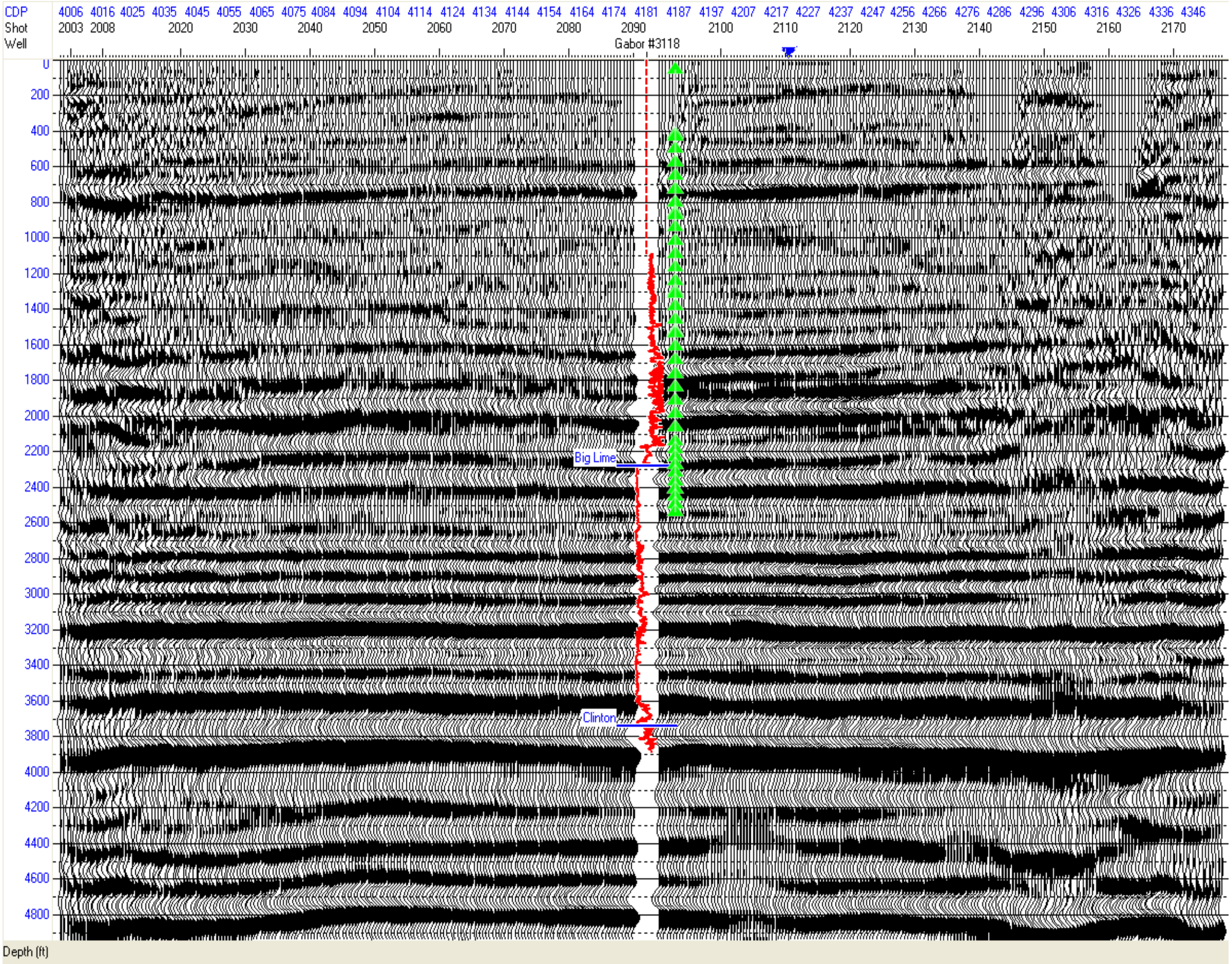

Figure 2: Migrated seismic section measured from surface 2D seismic survey over the borehole location (FFID2093-FFID2095). Green: Deployment of borehole receiver. Red: Gamma ray log from well #3118 that is 10m from the borehole.

Borehole Seismic Basics

The Concept of Borehole Seismic

Borehole seismic survey is a measurement procedure in which a seismic signal generated at the surface of the earth is recorded by geophones secured at various depths to the wall of a drilled borehole. Unlike surface geophone that is planted into ground, borehole geophone is rigidly clamped to the borehole wall so that it could move in phase with the borehole particle displacements created by seismic disturbances. The basic setup of borehole seismic survey is illustrated in Figure 3. A borehole seismic survey commonly includes check shot velocity survey and vertical seismic profile (VSP) with VSP being simply a precision level step change up from the check shot velocity survey. The basic difference between check shot survey and VSP is that the VSP measures all seismic waveforms in the well bore whereas the check shot velocity survey measures basically only the first break down-going energy.

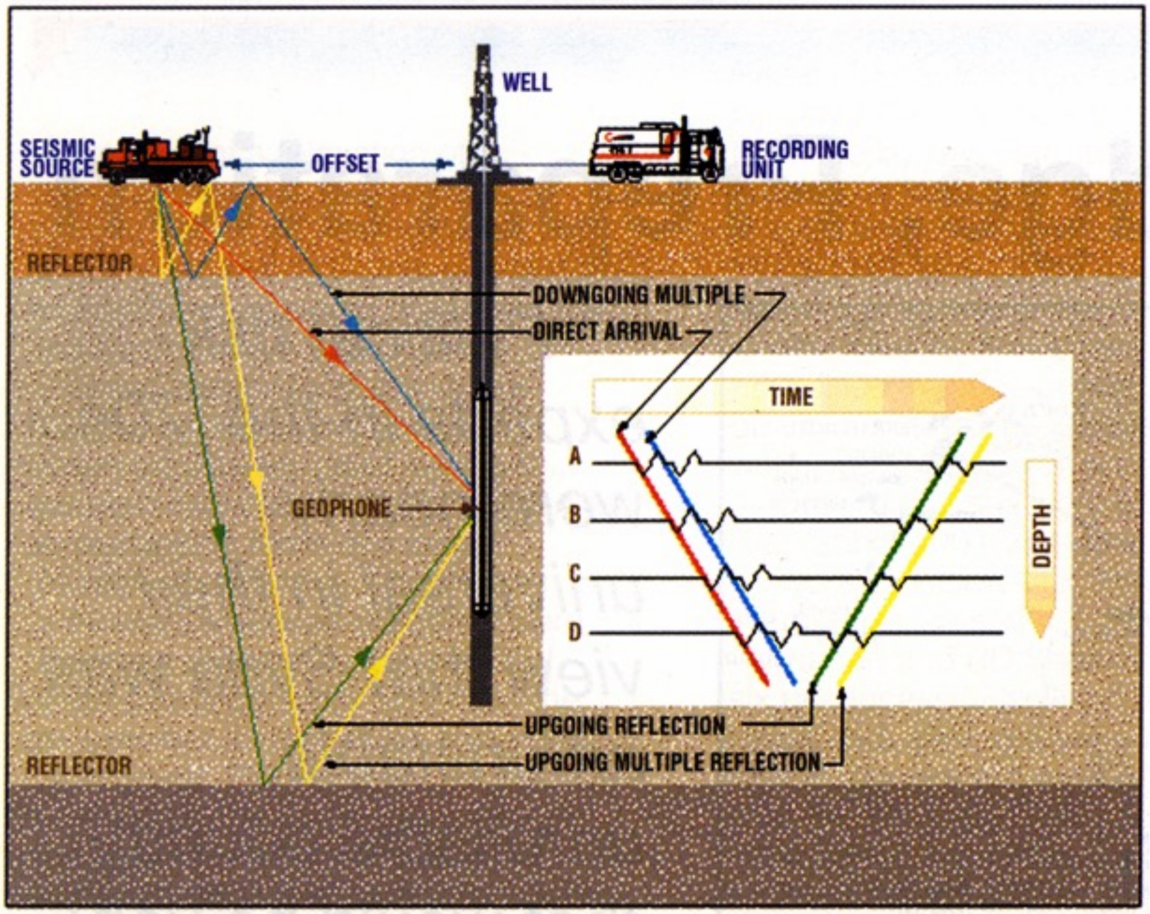

Figure 3: Typical equipment setup and seismic ray paths in a borehole seismic survey **(Brewer 2002)**.

Types of Borehole Waves and Noises

The main wave types recorded in a borehole seismic survey are illustrated in Figure 4, which is an example of a synthetic borehole record based on a simple four-layer model over an infinite substratum. The thickness and velocity of each layer is shown in the left plot of the figure. Events that are visible on the borehole record can be classified into two categories: down-going events that are direct arrivals and down-going multiples, up-going events that are primary reflections and up-going multiples, while if recorded at surface down-going events cannot be identified. The family of direct arrival rays defines a true one-way time-depth relationship for measuring wave propagation velocity. The cross point of direct arrival and up-going reflection defines a subsurface reflector. In a borehole section it is easier to distinguish primaries from multiples as to multiples do not intersect direct arrivals as primaries do.

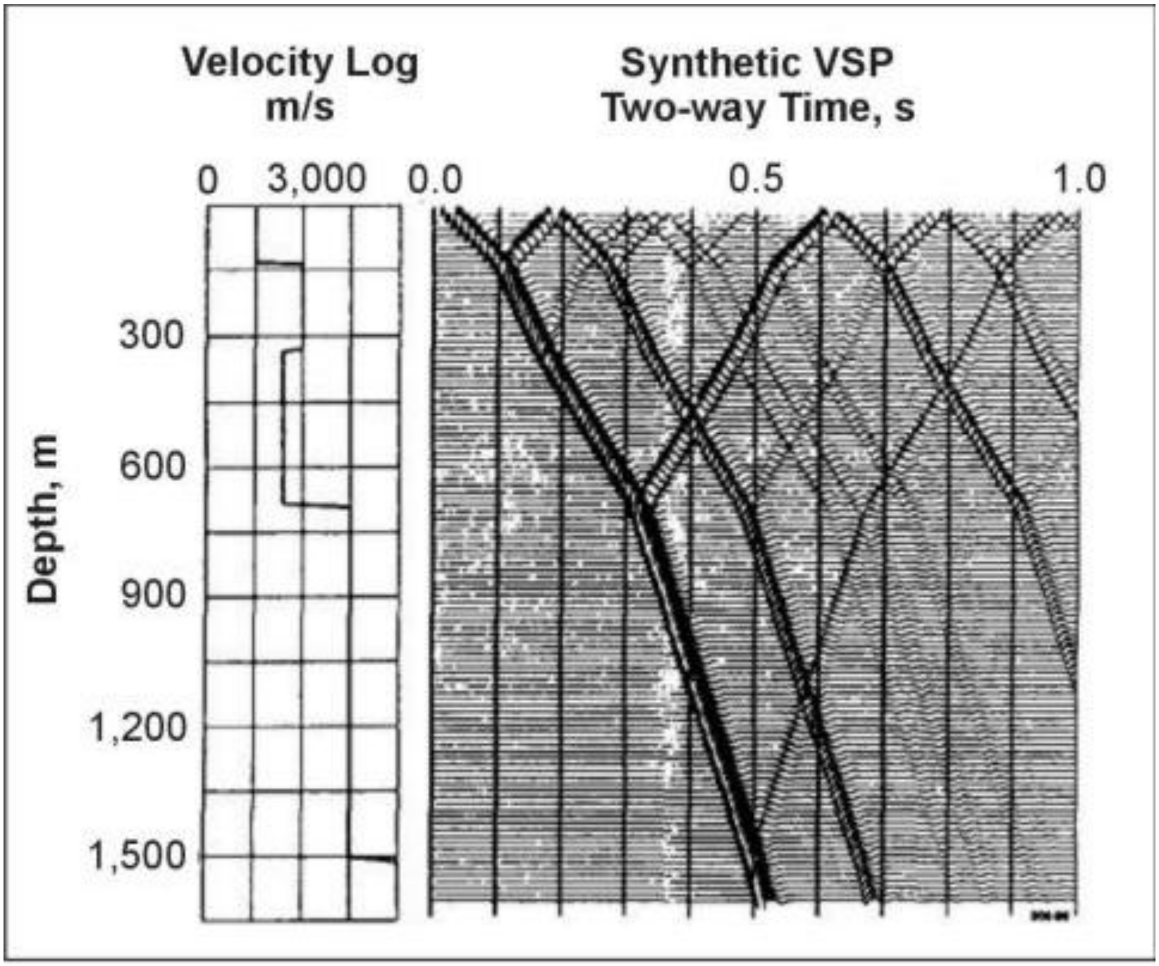

Figure 4: Example of synthetic vertical seismic profile based on a simple 4-layer model **(Wightman 2004)**.

Effects of ground roll, air blast, wind, and electrical power transmission lines that contaminate surface seismic survey are considerably reduced in a borehole seismic survey where a geophone is rigidly locked at great depths. However, there are still noise problems that are unique to borehole environment that contaminate borehole seismic data badly. Prominent noise modes that are frequently observed in borehole seismic recordings are related to the effects of geophone clamping, poor coupling, cable waves, and tube waves, which are shown in Figure 5 through Figure 9 correspondingly. In a borehole survey in a cased well it is necessary that the cementation be very well done and the geophone be rigidly clamped and coupled between casing and formation since the well related noised cannot be eliminated through processing successfully.

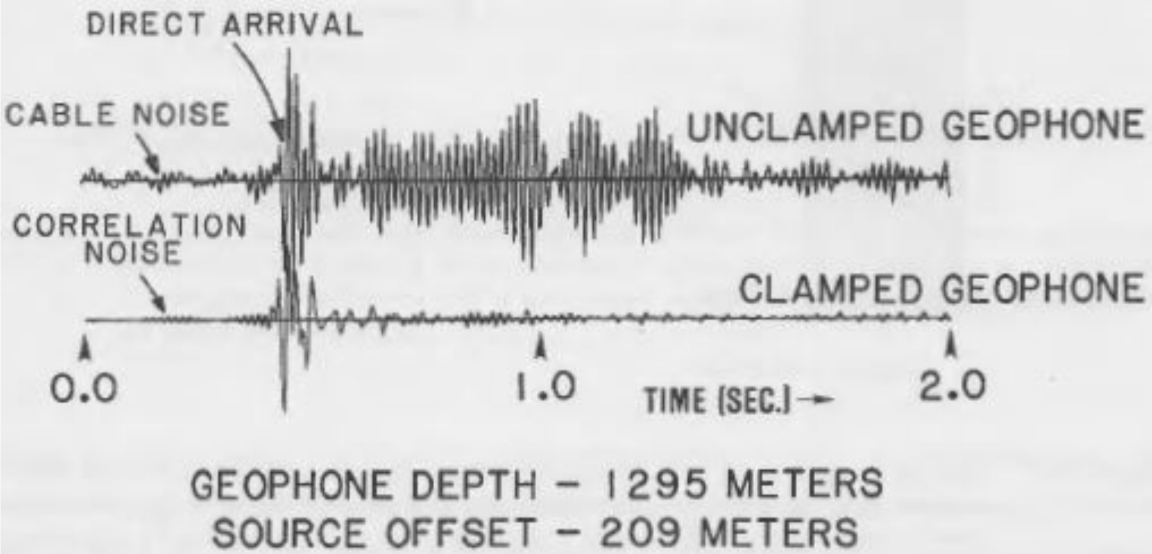

Figure 5: Effects of geophone clamping on signal response. Even though the geophone is 1295m below ground level and far removed from surface noise sources, the geophone cannot simply hang free in the fluid column and record meaningful data. The response of the unlocked geophone before the high amplitude direct arrival represents noise that is transmitted down the cable (Hardage 1983).

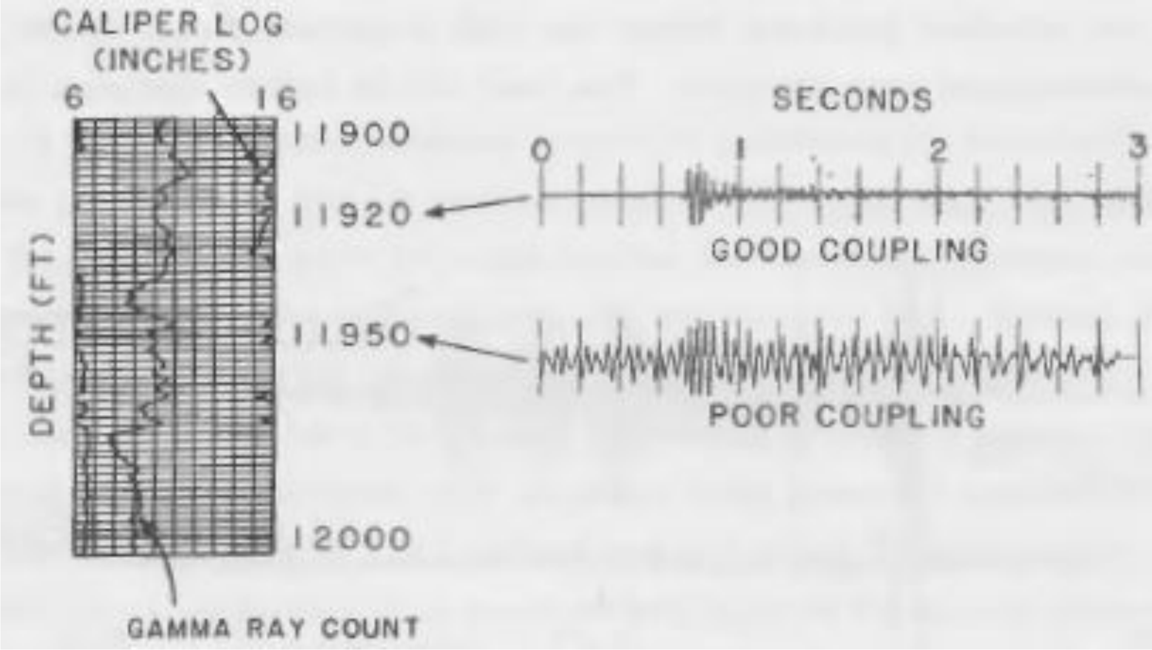

Figure 6: The locking arm of the downhole geophone assembly used in this well could extend only 16 inches. Consequently, the geophone could not be coupled to the formation in those depth intervals where large washouts occurred. If a caliper log were not available, a field observer would have no idea where the nearest depth would be where he could achieve good geophone-formation coupling (Hardage 1983).

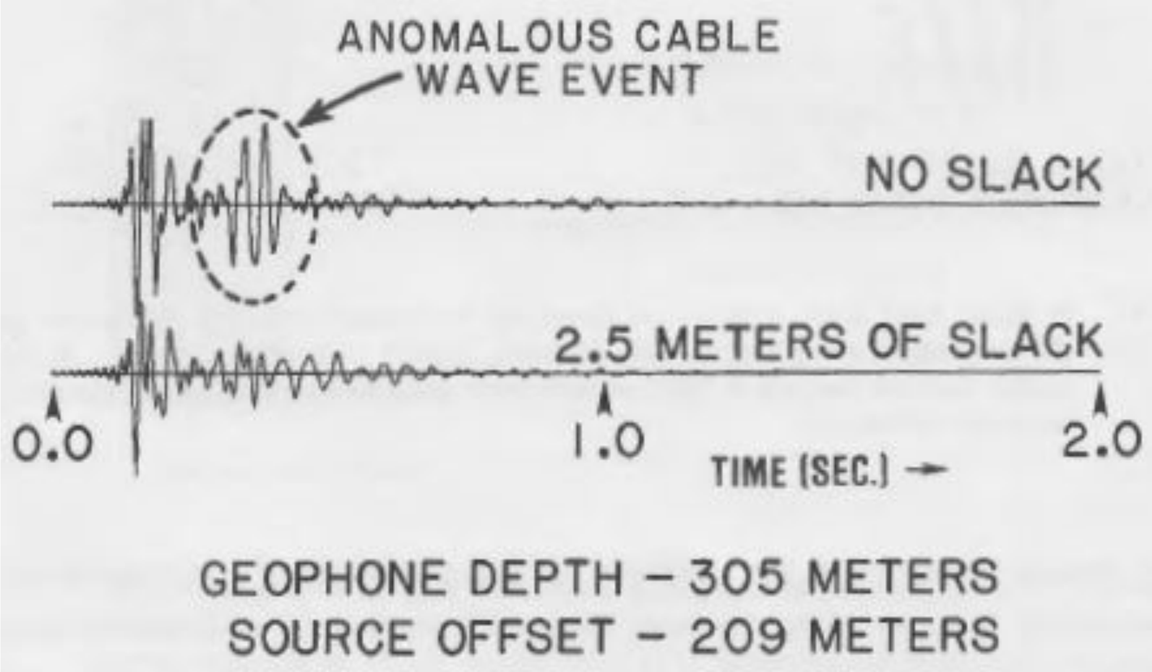

Figure 7: Effect of cable slack on geophone signal. When the Rayleigh wave created by the seismic surface source swept past the wellhead, the ground roll it created caused the mast supporting the recording cable to sway. This type of noise can be reduced by slacking the cable after the tool is locked downhole (Hardage 1983).

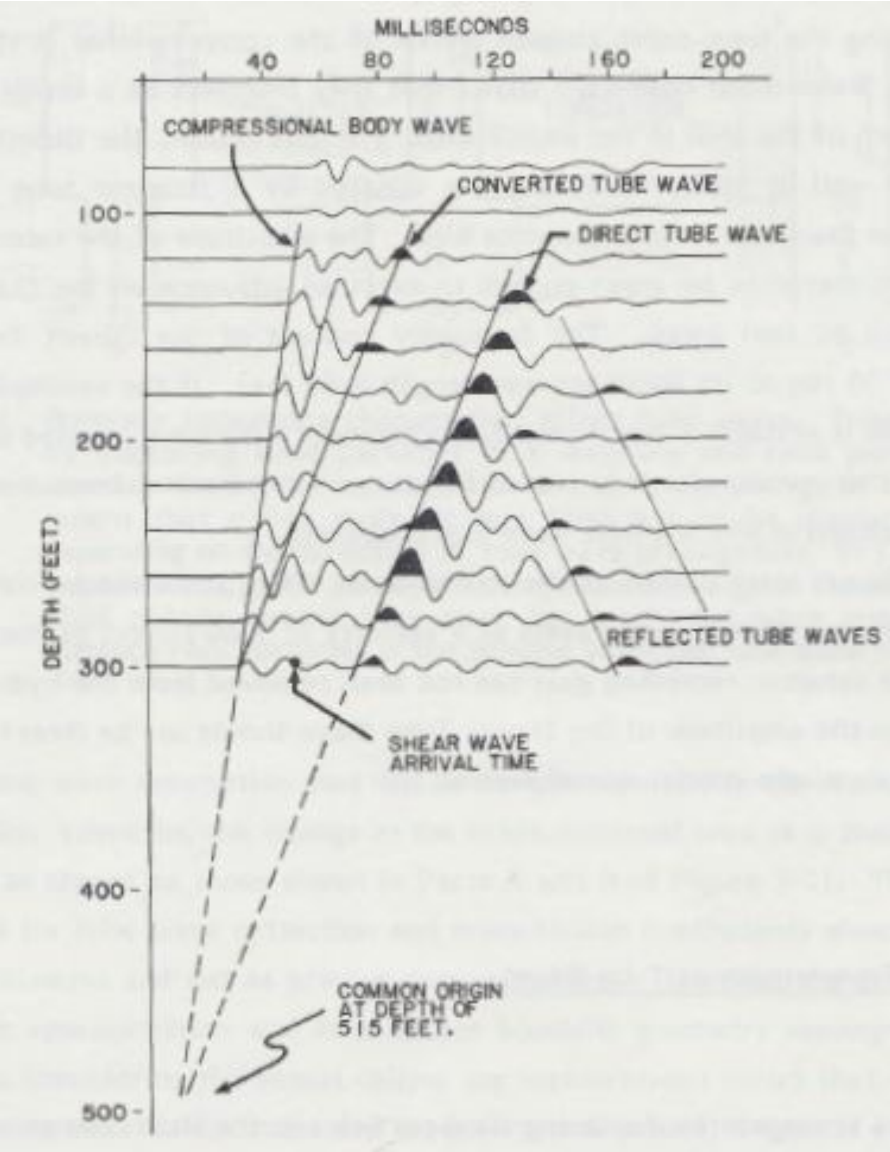

Figure 8: Data recorded by hydrophone hanging in the receiver well which is fluid-filled. The second events following the first arrivals are tube waves: they propagate at a velocity of 1500m/s and reflect downward when encountering changes in borehole impedance (Hardage 1983).

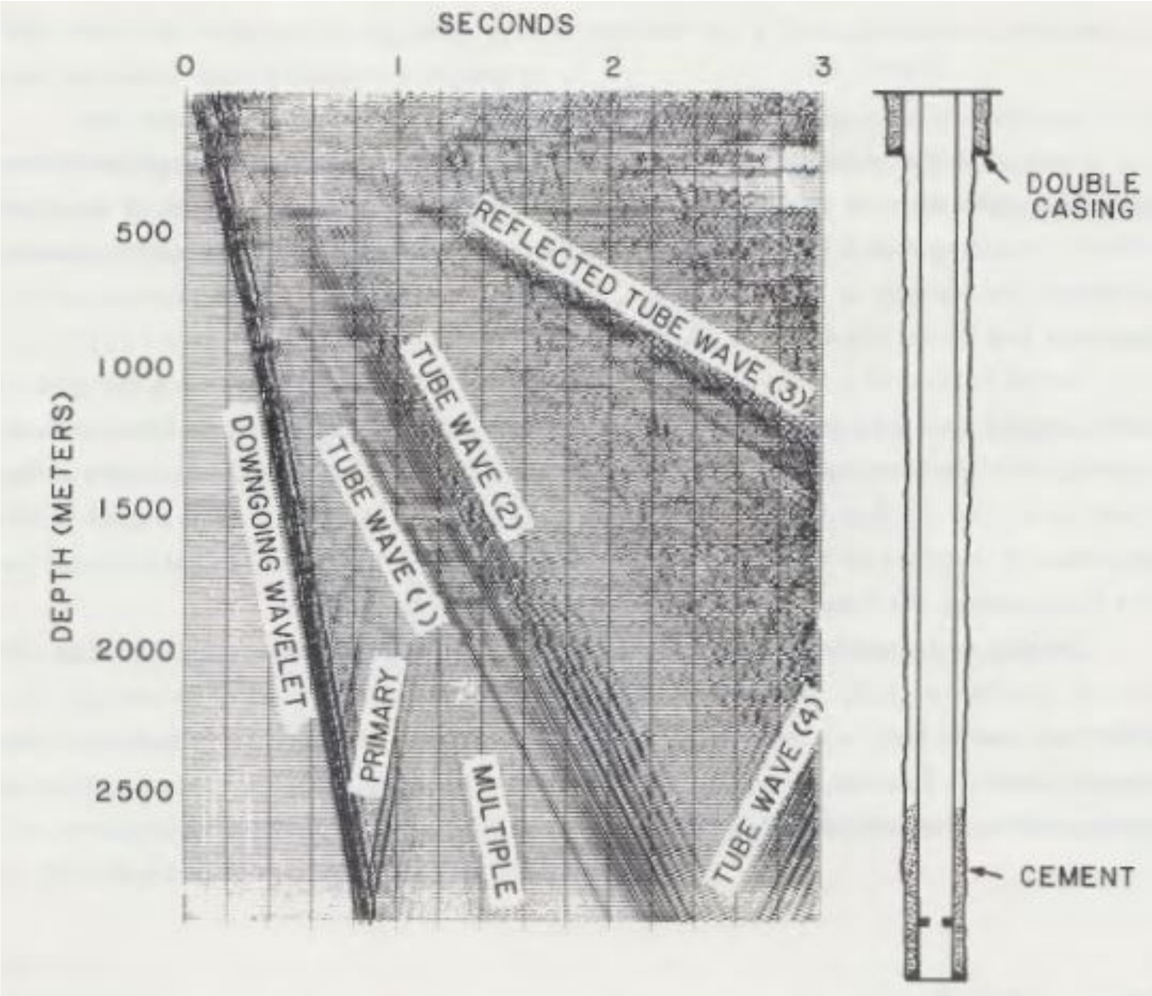

Figure 9: A borehole data set dominated by tube waves of four different modes. The data was recorded onshore using vibrators. The casing and cementing conditions in the well at the time the data were recorded are shown at the right. The objective that is to identify primary reflections is not completely achievable because the strong tube waves obliterate so many up-going events (Hardage 1983).

Application of Borehole Seismic

The data recorded in borehole permits the actual measurement of seismic energy as a function of depth and gives insights into some of the fundamental properties of propagating seismic wavelets. The increase in resolution resulting from retention of higher frequencies permits more confident measurement of lithological effects than from a surface seismic profile. First break times recorded from the borehole are the critical information needed to get layer interval velocity. By defining up-going and down-going events in the borehole record one can determine which events arriving at the surface are primary reflections and which events are multiples. By shifting up-going reflections to two-way time one can convert borehole seismic section to surface seismic section and process the borehole data as a surface seismic section. The advent of shear-wave seismic technology has brought with it the difficulty of resolving both P- and S-waves to the same lithologic boundary. The borehole seismic survey is one of the more effective means to provide quality control for both surface seismic profile and the generation of a reasonable synthetic seismogram. Other applications of borehole seismic data include estimation of reflector dip, correlation of shear wave reflections with compressional wave reflections, location of fault planes, looking for reflections ahead of the drill bit, determining hydrocarbon effects on propagating wavelets, and estimation of the conversion of compressional to shear and shear to compressional energy modes within the earth.

Hydrocarbon Low Frequency Anomaly

Low frequency (<10Hz) spectral anomalies at ~3Hz have been measured over hydrocarbon reservoir worldwide and have been used as hydrocarbon indicators (Saenger 2009). Dangel et al. (2003) investigated microtremor data to locate hydrocarbon bearing structures in the subsurface and found an empirical relationship between low frequency spectral anomalies in microtremor wavefields and the presence of hydrocarbon reservoirs. Natural mechanisms may be related to the partial saturation of the reservoir rocks, which can lead to pore-fluid oscillations (Frehner 2009) and/or abnormally high attenuation compared to the surrounding, fully saturated rocks (Quintal 2009). Most of the empirical observations are based on the surface surveys of vertical oriented records of the microtremor wavefield while in this study both vertical and horizontal components and combined surface and borehole arrays were applied. Lambert (2007) reported a coincidence between anomalies in the V/H ratio and the reservoir locations. Spectral ratios of the vertical (V) component over horizontal (H) are especially useful because they show much less temporal noise variations than single component or absolute, spectra and they are especially stable in the modifications of the microtremor wavefield. Two types of spectral attributes are analyzed to quantify the characteristic features of the wavefield's Fourier spectra in the low frequency range. The peak amplitude of the vertical and horizontal component spectrum focus on the amplitudes in the low frequency range. Peak amplitude of the V/H-ratio quantifies the magnitude of a dominant maximum in the V/H spectral ratio in the low frequency range.

Purpose

The 3C seismic data was collected with initial purpose of testing the field-worthiness of the new borehole tool, which turned out very satisfactory. With different types of sources involved in the survey, the present author processed the data as separate surveys: a check shot velocity survey, a VSP (vertical seismic profile), and a beat test survey. Thus, the purpose of the study was to determine rock velocities, to apply types of processing procedures exhaustively on the borehole records for determination of subsurface reflectors, and to verify whether low frequency anomalies are present in the wavefield over the Gabor gas field, meanwhile to find good practices to use in the future when faced with similar borehole seismic data.

II Methods

The seismic acquisition over Dominion East Ohio's Gabor gas storage field was performed by Spectraseis, Precision Geophysical, and Wright State University. Additional information was provided in the form of processed and migrated surface seismic sections by Tom McGovern of Seismic Earth Resources Technology and well log driller's log information with formation tops. Processing procedures of borehole data are different from that of conventional surface seismic data and were performed differently upon different source types. Processing of the check shot data was done separately on two different data sets: a 42-level array with sources at multi-azimuths and 9-level array with sources at the same locations. The former was focused on direct arrival that was processed with a basic processing flow followed by cross-correlation on MATLAB, allowing the determination of wave velocities; the latter focused on reflected waves and commenced with a general processing flow followed by FK filtering, arithmetic NMO correction and vertical summation, resulting in a corridor that was then tied to the migrated surface seismic section. The beat-sweep test data were recorded by both surface and borehole three-component broadband receivers and was processed on Geopsy software for spectral attributes.

Data Acquisition

Borehole data was collected with the experimental multilevel seismic array in an 807.7m (2650ft) deep monitoring well that was reported to be cased and well cemented. The deployments of the multilevel array took place in February 2011 during which time the reservoir at this location was filled and shut-in for possible extraction late in the heating season. The deployment was part of a multi-faceted combined borehole/surface seismic campaign shown in Figure 10. The borehole well was located at the cross point of a pair of 2D surface seismic lines having a receiver spacing of 82.5ft (25m). The overall receiver coverage vertically inside the borehole is depicted on the right side of Figure 10 and consisted of repeated deployments of 7 sondes at incrementally greater depths. The borehole sondes were deployed at a 23m (75ft) spacing starting from the water level at about 350ft (107m) depth, and was densified to 46ft (14m) in the lowermost part of the well. The eventual 42 levels were occupied in 6 different deployments of the 7-level array, acquiring 24-48hrs of continuous overnight data each at 1000sps sampling rate, before moving the array to the next greater depth range. The borehole data gathering procedure consisted of the following sequence:

- Incorporate sondes into the tubing string
- Lower the tubing to depth level N
- Record data (24-48 hrs)
- Pull the tubing and remove sondes
- Transfer data to the computer
- Reincorporate sondes onto the tubing
- Lower the tubing to depth level N+1 for next data recording

Small 80g calibration shots with microsecond precision universal timing were fired in a ring pattern around the receiver well for the check shot survey. In each ring sources were shot at 7-8 different azimuths while the 7 sondes or receivers were deployed at a certain range of depths in the borehole. Four rings of source points (9001 through 9032) were shot with the ring of shots being greater for greater depth of sonde deployment. The lower three sonde arrays shared the same ring of shot point locations with repeated shots.

The beat test data was acquired by operating two vibroseis sources slightly out-of frequency-phase to produce beats of low frequency. Two vibroseis sources were placed close together at the vicinity of wellhead labeled with a blue cross on the map (Figure 10). Three sweeps were generated with each lasting for 30s with a subsequent 5 minute listening time. The recording systems of beat test data included a surface spiral array, two linear arrays along the two seismic lines, and a single deployment of the 7-level borehole array. The surface spiral array was centered at the wellhead location and labeled with 301 through 316 on the map.

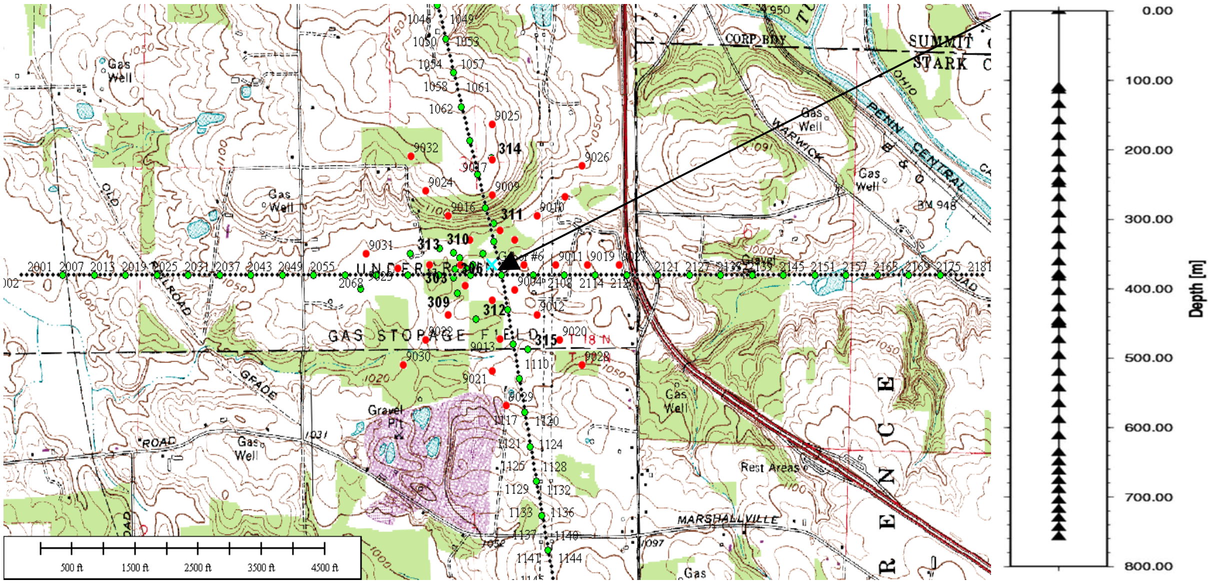

Figure 10: Deployment of the survey array. Left: Deployment of two types surface arrays that are 2D seismic lines crossing at borehole wellhead and a spiral array (Station301-316) centered at wellhead. (Green: Surface broadband stations. Red: Calibration shots.) Right: Borehole receiver geometry.

The surface recording system used 3C broadband seismometers, and borehole equipment applied actively boosted geophones with low eigen frequency and very high sensitivity. The electronic boosting system increases the sensitivity of a 4.5 Hz phone to 4800V/m/s. Coupling to the casing was ensured by a conveyance on standard production tubing, and resting part of the weight of the tubing string at TD of the well. This allowed a completely autonomous system where no cables of any kind and no moving part on the shuttle are required (Figure 11). It is also flexible and scalable in the sense that each sonde can be combined to a multilevel array at almost arbitrary spacing. The main specifications are (Goertz 2011):

- 4.4’’ OD shuttle—fits inside 5.5’’ casing
- Max temperature 65°C
- Max depth 2438.4m (8000ft) /5000psi
- Deployed on standard 2 3/8’’ (0.7239m) production tubing
- Gimbaled 3C sensor elements (up to 24° tilt)
- 24-bit 3-chan digitizer 200-2000sps
- Self-noise less than -200dB
- Up to 10 days of recording
- 0.05 ppm time accuracy before clock drift correction

Figure 11: Borehole data recording system **(Goertz 2011)**.

Processing Software and Flows

The borehole data were provided in Passcal SEGY format and was converted to standard SEGY in MATLAB in order to be readable in other software. Data were processed and viewed on Promax which supplies a user interface with processing flows that can be altered easily. For the check shot records noises problematic in the raw shots (i.e., possibly related to loose geophones, poor coupling, poor cementation, and tube waves) interfered with seismic signals of some records and made primaries hard to recognize. Such noises are hard to remove through frequency filtering as they either have wide range of frequency or resonate after the direct arrival and completely mask seismic events. After careful examination of each individual trace, all traces badly contaminated with borehole noises were omitted leaving the best check shot records to be processed.

Processing of check shot data started with bandpass filtering in order to improve the wave shape and reduce noise as much as possible. Direct arrivals were isolated and transferred into MATLAB for determination of wave velocities using cross-correlation method. FK filtering and NMO correction were administrated on the data with the goal of enhancing up-going reflections and converting borehole reflection to surface reflection. Vertical summation was done on the aligned reflections, which resulted in a composite trace. The basic flow procedures on processing check shot data were as follows:

- Write as SEGY Format
- Read SEGY Data
- Set Geometry
- Trace Mute
- Band-pass Filtering
- Pick First Breaks
- Cross-Correlation
- Determine Velocity
- Compare Velocity with Stacking Velocity
- FK Filtering
- Trace Mute
- NMO Correction
- Restricted Vertical Summation

- Phase Rotation
- Tie to Surface Seismic Section

Spectral Attributes

Beat test data was processed using Geopsy software which contains various processing and analysis routines for spectral attributes. Processing has been largely automated so that relatively simple cases can be processed with minimum of human interaction. Two types of spectral attributes were analyzed: amplitude spectrum and V/H-ratio in the low frequency range (1-10Hz). The data at a relatively quiet time immediately before the beat test was used to represent the background signal level to be compared to the data after the beats were generated. Beat test data was tracked through time and showed the change of spectral attributes in the low frequency range caused by beats. The beat test result measured from surface data was also compared with that measured in borehole. The basic processing flow of the beat test data was as follows:

- Set Header
- Raw Beat Test Record
- Spectrum Analysis of the Surface Data
- Spectrum Analysis of the Borehole Data
- V/H-ratio Analysis of the Surface Data
- V/H-ratio Analysis of the Borehole Data

III. Processing

The following sections illustrate several general data processing procedures that needed to be applied to the check shot data. The processing portion of check shot data was done on MATLAB and Promax. Raw borehole data was provided as a one hour fixed trace length of 3,600,000 samples in Passcal SEGY format, which prior to processing was converted by the author on MATLAB to standard SEGY format in order to be readable in Promax. Channels badly contaminated with borehole noises were omitted from further processing.

The first step when looking at the check shot data was to examine the first arrival on each individual trace, which was later isolated with top-mute and bottom-mute. Bandpass filtering was applied on each shot gather individually to remove noise as much as possible and to reconstruct the wave shape. Time shift between successive traces was determined by applying cross-correlation method on MATLAB. Average propagation P-wave velocity between two receiver depths was determined mathematically.

Data recorded from the deepest two arrays was sourced on different days from the same shot location, allowing a creation of check shot gather of 9 traces. The 9-trace gather was processed in Promax starting with mutes and F-K filtering in order to destruct down-going events and enhance up-going reflections. Static time shifting was applied on the data to convert the borehole-recorded reflections to surface-recorded reflections at two-way travel time. The time-shifted data was summed vertically after normal move-out correction so as to generate a composite trace containing up-going primaries.

Convert Passcal. SEG-Y to SEG-Y

In the check shot survey dynamite sources were applied at various offsets and azimuths, recorded using UTM system shown in Table 2. Shot time of each source was recorded in day/hour/minute/second/microsecond shown in Table 3. Considering that the data size limitation on Promax is 32000, the author created several new data files from the raw records (Appendix A). These files were 1s in length, starting from the shot time T_0 and sampled at 1ms. Each file is a shot gather record of 7 traces. As a result of this preprocessing 46 SEGY files of shot gather records were successfully created from the raw 1 hour data files.

Table 2: Shot locations using UTM-Easting, Northing and altitude.

FFID	UTMEasting	UTMNorthing	Altitude	FFID	UTMEasting	UTMNorthing	Altitude
Ring 1				Ring 2			
9001	444783	4528629	316	9010	444962	4528703	316
9002	444858	4528592	315	9011	445050	4528446	320
9003	444896	4528446	319	9012	444952	4528265	316
9004	444848	4528377	317	9013	444812	4528150	314
9005	444739	4528337	314	9014	444504	4528293	312
9007	444573	4528470	313	9015	444438	4528470	313
9008	444637	4528607	316	9016	444531	4528700	333
Ring 3				Ring 4; Ring 5; Ring 6			
9017	444751	4528940	351	9025	444754	4529092	352
9018	445037	4528815	318	9026	445179	4528917	320
9019	445202	4528471	322	9027	445354	4528465	317
9020	445061	4528154	320	9028	445235	4528126	316
9021	444735	4528025	313	9029	444802	4527821	318
9022	444409	4528178	310	9030	444305	4528059	311
9023	444287	4528436	314	9031	444137	4528575	315
9024	444425	4528811	341	9032	444403	4528979	349
well head	444744.85	4528488	315				

Table 3: Check-shot timing recorded in day/hour/minute/second/microsecond.

FFID	Date	hr:min:sec	microsec	FFID	Date	hr:min:sec	microsec
Ring 1				Ring 2			
9001	1/31/2011	15:07:16	660060	9010	1/31/2011	21:53:13	248161
9002	1/31/2011	15:12:29	368155	9011	1/31/2011	20:35:18	636189
9003	1/31/2011	15:20:05	580279	9012	1/31/2011	20:48:30	976182
9004	1/31/2011	15:25:30	728355	9013	1/31/2011	20:58:01	548172
9005	1/31/2011	14:38:55	295465	9014	1/31/2011	21:07:10	88165
9007	1/31/2011	14:50:25	147720	9015	1/31/2011	21:14:41	756163
9008	1/31/2011	15:00:24	107926	9016	1/31/2011	21:26:16	456158
Ring 3				Ring 4			
9017	2/3/2011	15:24:21	928779	9025	2/3/2011	22:26:59	93906
9018	2/3/2011	15:09:17	368533	9026	2/3/2011	22:42:45	809944
9019	2/3/2011	14:58:07	76301	9027	2/3/2011	21:48:56	105766
9020	2/3/2011	14:44:11	115970	9028	2/3/2011	22:03:48	561826
9021	2/3/2011	16:41:45	13282	9029	2/3/2011	22:21:05	741890
9022	2/3/2011	16:15:48	265198	9030	2/3/2011	22:59:12	305966
9023	2/3/2011	16:02:59	233122	9031	2/3/2011	21:50:23	997772
9024	2/3/2011	15:39:23	316955	9032	2/3/2011	22:07:40	645842
Ring 5				Ring 6			
9025	2/4/2011	17:52:23	898360	9025	2/6/2011	18:06:38	877468
9026	2/4/2011	17:57:56	278422	9026	2/6/2011	18:32:01	185727
9027	2/4/2011	18:05:56	22513	9027	2/6/2011	17:40:06	304969
9028	2/4/2011	18:13:14	110594	9028	2/6/2011	17:53:52	709260
9029	2/4/2011	18:20:56	466678	9029	2/6/2011	18:25:24	741674
9030	2/4/2011	18:35:29	782822	9030	2/6/2011	18:43:15	185801
9031	2/4/2011	17:35:05	270160	9031	2/6/2011	17:31:24	188753
9032	2/4/2011	17:43:33	358258	9032	2/6/2011	17:46:38	997114

Raw Shot Gather

46 SEGY files of shot gather records were input into Promax for viewing and processing. The raw shot gather record has many characteristics unique to the borehole environment that are not seen at surface seismic survey. Borehole seismic survey typically contains effects from geophone clamping, unbounded casing, poor cementation, tube waves and etc. The kind of noise seen on borehole seismic survey illustrated in Figure 5 through Figure 10 were also present in this borehole survey (Figure 47 and Figure 48 in Appendix B). Any geophone tool used to record borehole seismic data must be capable of rigidly and faithfully bonding the

geophone case to the borehole wall, otherwise, weak signals cannot be resolved. Noisy records as those in Appendix B were omitted from analysis, including: FFID9014, FFID9019, FFID9024, Ring4_FFID9025, Ring4_FFID9026, Ring4_FFID9027, Ring4_FFID9032, Ring5_FFID9025, Ring5_FFID9027, Ring5_FFID9029, Ring5_FFID9032, Ring6_FFID9025, Ring6_FFID9031, Ring6_FFID9032.

Figure 12 shows a shot gather record with good signal-noise-ratio (SNR) that was recorded at the fourth depth array where the borehole was single-cased and well-cemented with dynamite sourced at 2015.7ft (614.4m) well offset. The direct arrival was easily identified at ~250ms. Channel 1 and 2 referred to sensor 1 and 3 that were 3meters spaced, and had a very close first break time. Background noise appearing as the small wiggles prior to direct arrivals had a dominant frequency of ~250Hz therefore could be removed by applying a high cut frequency filtering. Later at ~450ms was a train of high amplitude but low velocity events which were possibly tube waves. Tube waves are fluid-borne borehole wave modes created when fluid particles in any part of the fluid column in a wellbore are displaced. Tube wave amplitudes do not diminish with travel distance since they cannot expand spherically in all directions as a body wave does. Tube waves may span the same frequency band that body waves do, therefore cannot be effectively eliminated by frequency filtering (Hardage 1981). The high amplitude event at ~500ms propagating at infinite velocity was possibly casing wave interference (wave velocity in casing is 5500m/s).

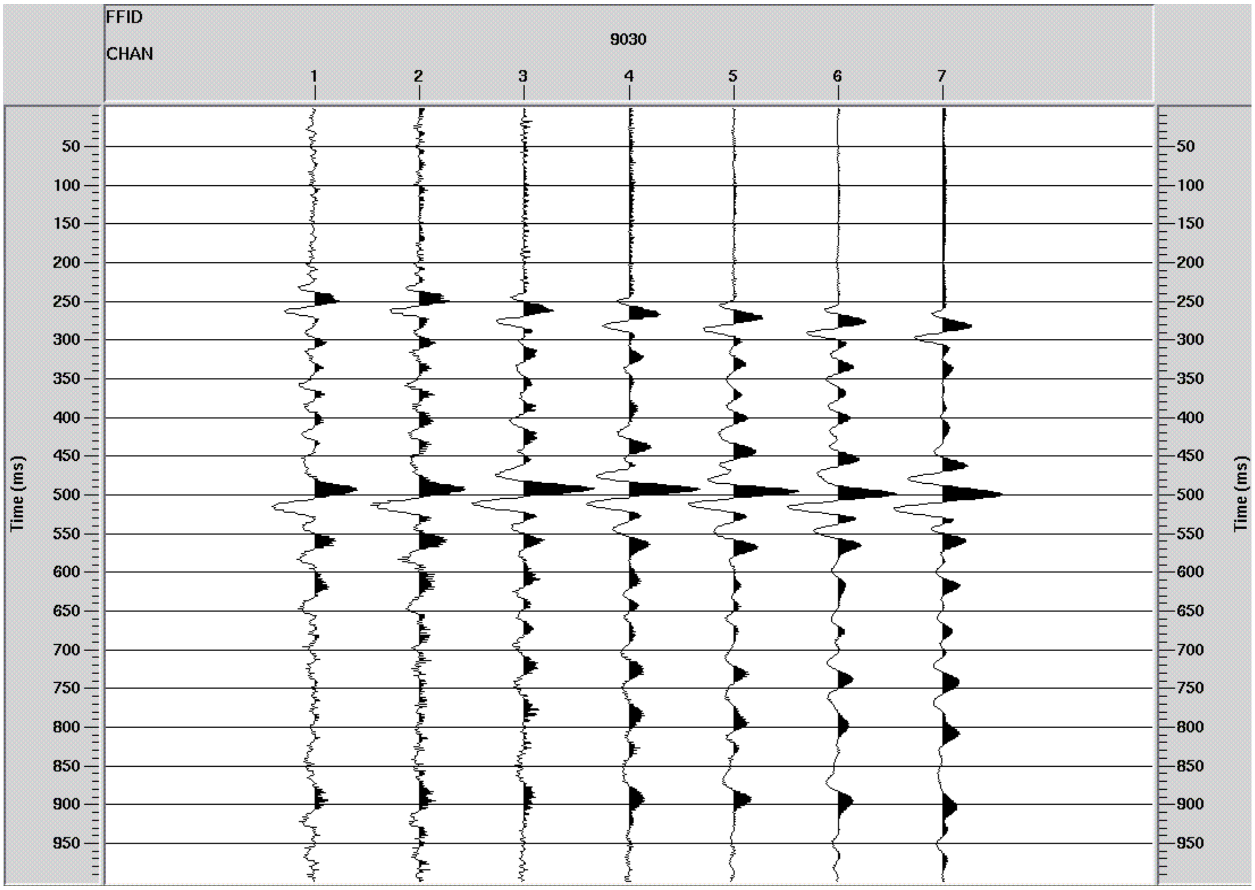

Figure 12: Shot gather with FFID 9030. Channel number 1-7 refers to 7 sensors displayed at the fourth depth level, from top to bottom correspondingly.

Set Header Information

Due to the unique data format and the source-receiver deployment, most built-in flow controls in Promax did not work easily on this borehole record. For example, header geometry was unable to be set with 2D Land Geometry processor that is the most widely used for land seismic data. A tedious but successful way to set geometry combined several IF-ENDIF flow controls together with Trace Header Math. The following flow is an example of such a Promax flow:

IF Include

FFID number

CHAN number

9030:1/

Trace Header Math

Fix Equation

FFID=9030

Trace Header Math

Fix Equation

SOU_X=444305.287

Trace Header Math

Fix Equation

SOU_Y=4528058.5

Trace Header Math

Fix Equation

SOU_ELEV=310.77

Trace Header Math

Fix Equation

REC_X=444732.08

Trace Header Math

Fix Equation

REC_Y=4528482.4

Trace Header Math

Fix Equation

```
        REC_ELEV=-133.06
ENDIF
```

First Break Examination

The onset of down-going first arrival is referred to as the first break (Mari 2003). Time picks allow the determination of the time-depth relationship and the calculation of average and interval velocities. First breaks occur in varying degrees of quality, depending on the source type, near-surface conditions, and subsurface anisotropy. Impulse sources give signature with a clean initial start allowing a precise time pick of the first arrival, whereas vibroseis sources often produce poor first breaks and the remainder of the sidelobes from sweep correlation may mask the onset of the first arrivals (Yilmaz 2000).

Figure 13 shows a receiver gather record from sensor 4 in the second depth array. 7 dynamite sources were shot at 7 different azimuths and offsets in a ring pattern from the wellhead. Shot FFID were labeled at the top of each trace to indicate the source that generated that individual trace. Data sourced by FFID9014 and FFID9015 were omitted due to bad noise contamination. This record shows clear onset of first breaks on every trace. Deviations from the linear trend of the first break times may largely be attributed to elevation differences, inconstant offsets and subsurface rock anisotropy. Wave shapes of direct arrivals appeared to be contaminated with an unknown noise that may already have existed before the first arrival, especially for traces labeled FFID9013 and FFID9010 in the record. In fact, background noise not only interfered with first arrivals, they also affected other events during the whole recording time, complicating wave shapes. Therefore, muting and bandpass filtering were necessary in order to remove this high frequency background noise and reconstruct wave shapes.

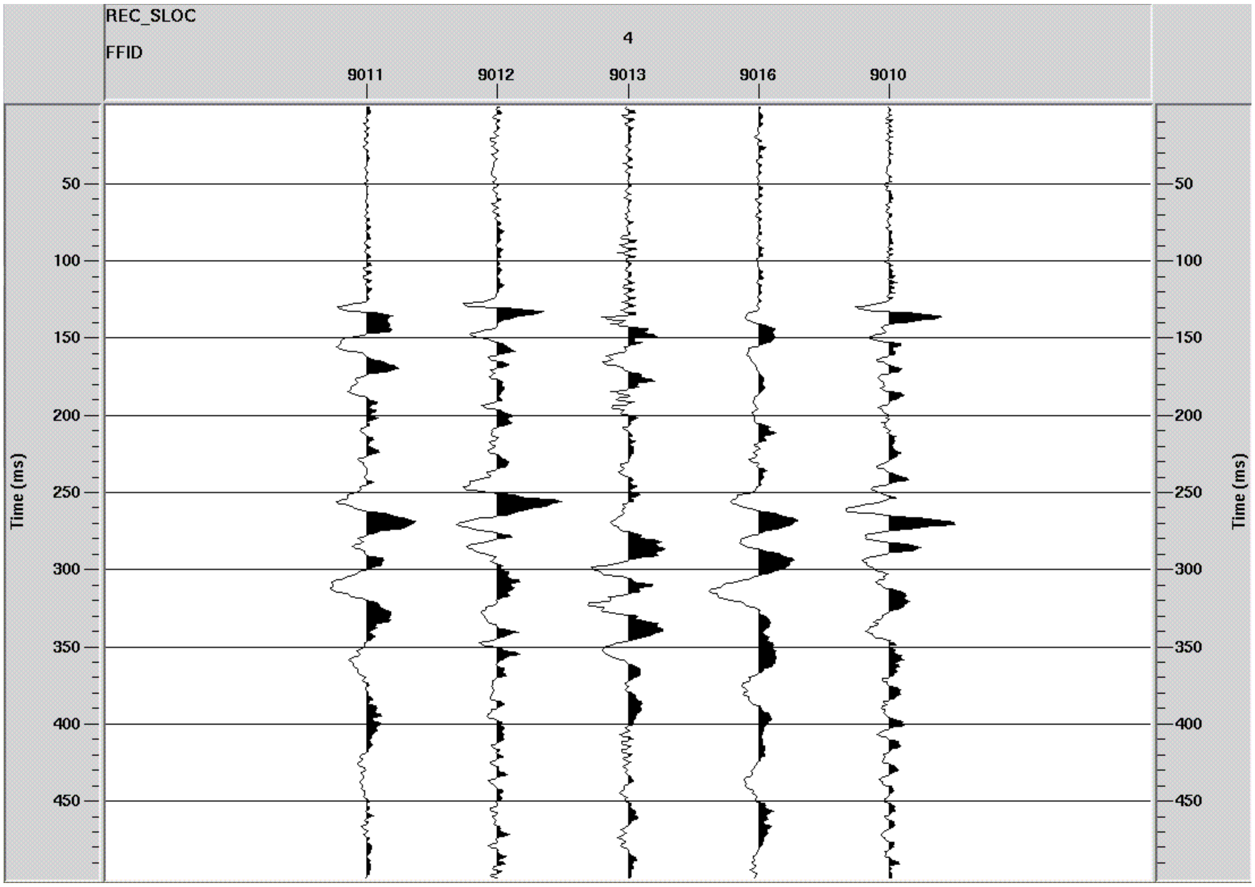

Figure 13: Receiver gather sensor 4 in the second depth deployment. Secondary trace header labeling is shot FFID of every individual trace: 9011, 9012, 9013, 9016, and 9010, from left to right.

A time window was selected which contained the least scattering and the least uncertainty (Knowlton and Spencer, 1996) to determine the dominant wave frequency and the first break time (Appendix C). The window covered a half period of the first arrival, starting from the time when wave amplitude was zero and ending with the time when wave amplitude went back to zero, shown in Table 4.

Table 4: Time windows (start time: end time) of first arrivals for each individual traces. (Continued on next page)

Ring 1	Elevation	FFID9001	FFID9002	FFID9003	FFID9004	FFID9005	FFID9007	FFID9008
Sensor 1	203.835	90:103	91:107	91:105	89:103	93:107	106:121	94:110
Sensor 3	200.177	90:103	91:107	91:104	89:102	93:107	106:120	94:109
Sensor 4	179.131	85:100	91:103	85:100	83:96	88:103	103:117	90:105
Sensor 5	155.981	98:109	97:112	96:109	95:106	98:111	111:126	101:114
Sensor 6	133.06	98:115	103:120	101:112	99:112	104:117	118:132	105:121
Sensor 7	109.926	112:128	113:130	112:123	111:122	115:130	122:142	116:133
Sensor 8	87.02	116:132	119:135	116:127	116:128	119:133	127:147	121:135
Ring 2	Elevation	FFID9010	FFID9011	FFID9012	FFID9013	FFID9015	FFID9016	
Sensor 1	68.854	120:131	120:132	119:129	130:140	123:133	128:140	
Sensor 3	65.197	120:131	121:131	115:128	131:139	121:132	129:138	
Sensor 4	44.882	122:133	126:133	120:131	135:143	124:134	130:141	
Sensor 5	21.671	128:138	130:138	123:135	137:146	129:139	136:146	
Sensor 6	-1.036	133:143	135:143	131:140	142:153	134:144	141:151	
Sensor 2	-23.957	139:148	138:151	137:146	145:158	139:150	144:157	
Sensor 8	-47.366	144:153	145:154	141:150	147:161	144:155	149:162	
Ring 3	Elevation	FFID9017	FFID9018	FFID9020	FFID9022	FFID9023		
Sensor 1	-65.532	189:201	172:186	172:185	172:185	186:198		
Sensor 3	-69.19	187:199	175:183	172:183	170:183	184:195		
Sensor 4	-90.465	180:193	166:177	166:178	163:178	177:189		
Sensor 5	-113.386	193:204	179:188	177:188	178:188	189:200		
Sensor 6	-136.489	199:209	182:192	183:192	181:191	193:203		
Sensor 2	-159.365	211:222	195:207	196:206	195:206	204:217		
Sensor 8	-182.27	212:222	197:205	197:206	194:205	204:217		
Ring 4	Elevation	FFID9028	FFID9029	FFID9030	FFID9031			
Sensor 1	-133.06	212:223	237:248	221:239	216:225			
Sensor 3	-136.718	213:212	236:247	226:236	218:225			
Sensor 4	-206.548	227:235	246:257	239:251	230:237			
Sensor 5	-228.935	231:242	252:262	243:255	235:243			
Sensor 6	-251.811	235:246	254:268	248:261	238:248			
Sensor 2	-274.564	242:252	259:274	254:267	244:253			
Sensor 8	-297.972	248:256	268:277	261:271	251:257			

Table 4: (Continued) Time windows (start time: end time) of first arrivals for each individual traces.

Ring 5	Elevation	FFID9026	FFID9029	FFID9030	FFID9031	
Sensor 1	-133.182	219:228	-	227:237	212:226	
Sensor 3	-136.84	219:229	-	228:238	217:227	
Sensor 4	-321.975	249:259	261:277	258:270	248:258	
Sensor 5	-335.646	258:266	273:283	266:277	256:265	
Sensor 6	-348.813	257:265	274:288	268:279	257:266	
Sensor 2	-362.224	263:272	280:292	272:282	263:272	
Sensor 8	-375.422	267:277	281:292	277:286	269:275	
Ring 6	Elevation	FFID9026	FFID9027	FFID9028	FFID9029	FFID9030
Sensor 1	-133.289	-	-	-	-	225:241
Sensor 3	-136.947	-	219:229	220:229	-	234:246
Sensor 4	-390.418	253:261	250:260	250:260	267:281	262:275
Sensor 5	-403.83	265:272	261:270	260:272	280:291	273:285
Sensor 6	-416.418	263:272	261:271	262:273	280:291	274:287
Sensor 2	-429.814	272:282	270:279	271:281	288:301	283:296

Trace Mute

After close examination of first arrivals on each individual trace muting was applied. Both top mute and bottom mute were applied to zero data above and below the first arrivals. This helped considerably in calculating maximum correlation in later process since mutes could minimize effects from any other seismic events irrelevant to the first arrival. Mutes were originally picked right at the time of start time and end time of first arrival wave cycle, but it turned out that the resulting waveforms were affected with artifacts produced by muting. To fully keep the raw waveform of first arrival and minimize artifacts that could be produced by muting, top mute was then adjusted to be ~2ms before the first break, and bottom mute was ~2ms after the total cycle of first arrival (Figure 14). The lower plot in the figure is the result of the mutes applied on FFID 9030.

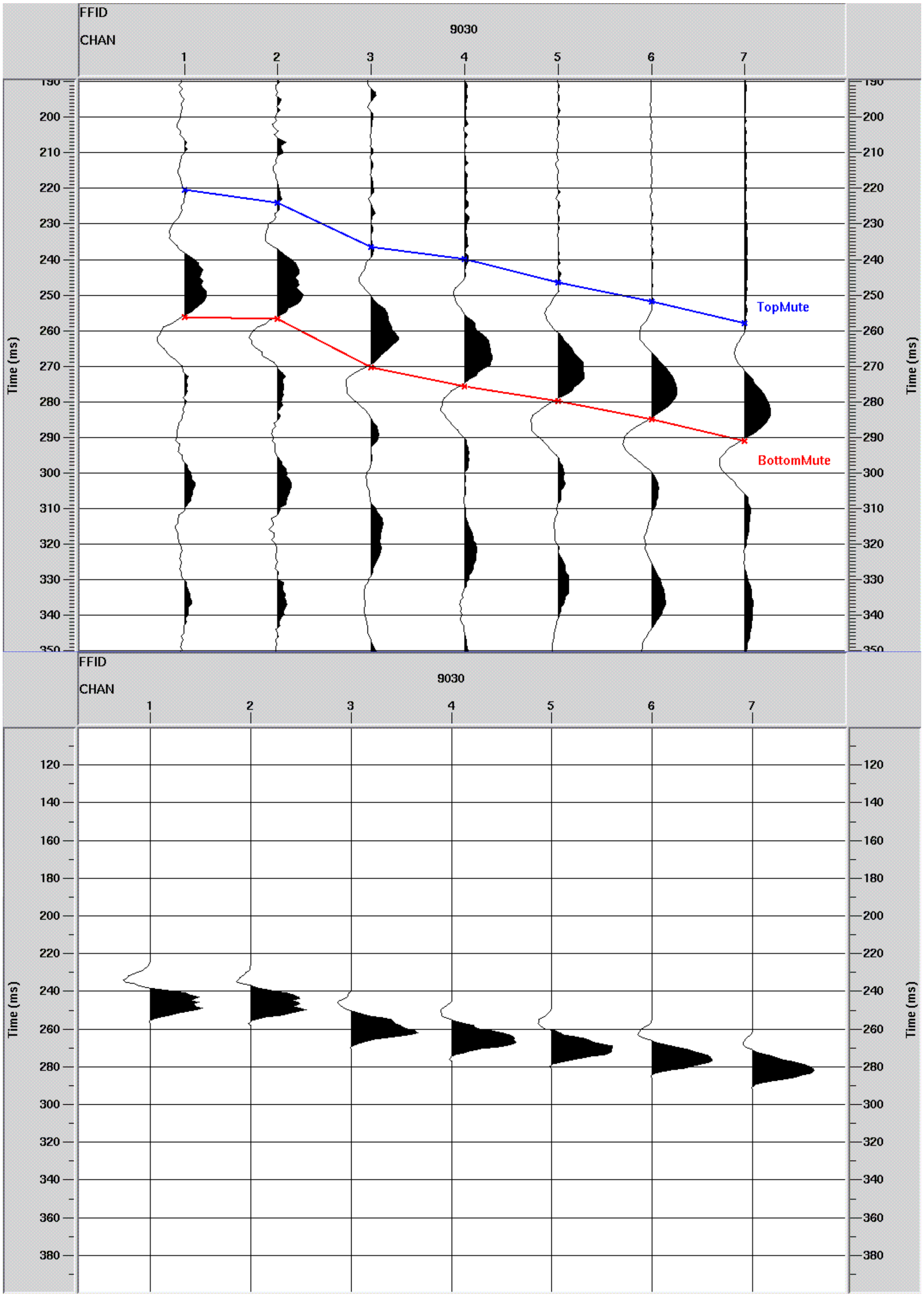

Figure 14: FFID 9030 with top mute and bottom mute above and below first arrival. The lower one is the result of mutes with first arrival isolated.

Bandpass Filtering

With the processing of mutes the first arrival was very well isolated but still had some kind of noise interference. A frequency filtering was then applied on the muted data to suppress any coherent or incoherent event whose dominant frequency is different from that of first arrivals. Dominant frequency of first arrivals was calculated as inverse of the wave period: f=1/T, in which T was determined from the previous selected time windows. As the frequency characteristics of first arrivals are influenced by the prevailing geology, high frequency absorption, the appropriate time variant frequency filtering may also vary as a function of depth. The resulted dominant frequency was 35-38Hz for data recorded at the first depth level, 40-45Hz for other depth levels.

A zero-phase Ormsby bandpass was applied on the data for all depths with changed frequency parameters. Frequency parameter for the first depth data was 20-30-40-50 which means that waves 30-40Hz were 0% filtered, waves lower than 20Hz or higher than 50Hz were 100% filtered, and waves 20-30Hz and 40-50Hz were 75% filtered. The frequency values applied on other 5 depth levels were 20-30-50-60. The frequency process was done in time domain which involved convolving the filter operator with the input time series. Convolution in the time domain is equivalent to multiplication in frequency domain. First arrival waveform was thus reconstructed which contained only those frequencies that made up the wavelet used in filtering, shown in Figure 15. The bandpass filtering process resulted in much better developed first arrival waves.

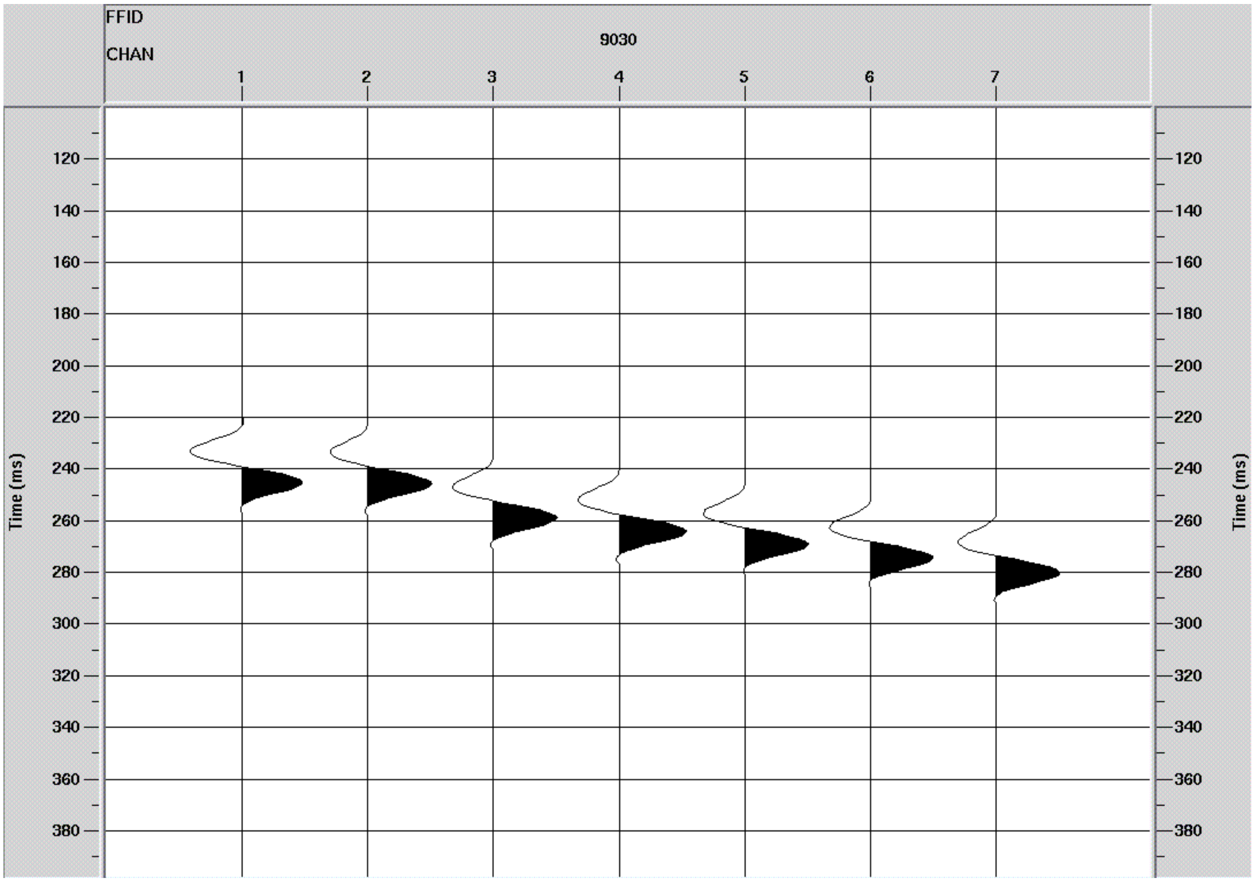

Figure 15: FFID 9030 with geometry, trace muting, and 20-30-50-60 bandpass filtering.

Cross-Correlation

After first arrivals were isolated and reconstructed from the above processing, a cross-correlation technique was used to determine the correct time shift which offered more accurate and efficient results compared with hand-picked values. Cross-correlation measures similarity or time alignment of two traces and determines the time lag at which they are most similar. If two identical waveforms are cross-correlated all the cross-multiplication products will sum at zero lag to give a maximum positive value. The cross-correlation on MATLAB applies a syntax: c (:, i)=xcorr(x, y) (Appendix A).

The result of cross-correlation of the data at the first depth array was shown in Figure 16. For the data at the first depth array the top sensor had the best developed waveform so it was selected to be cross-correlated by the other six traces. In Figure 16 the columns correspond to shot gathers and rows correspond to traces. For example, the plot at column 2 row 3 corresponds to cross-correlation of trace 3 and trace 1 in the shot gather FFID9007. The peak in the plot refers to the maximum correlation between traces. Upon inspection one can see that there is a positive time shift between successive traces with depth. By applying another MATLAB syntax: [value,index]=max(c), one can get the index of the maximum correlation from which the correct time shift could be calculated. Table 5 shows the index of the maximum correlation between traces.

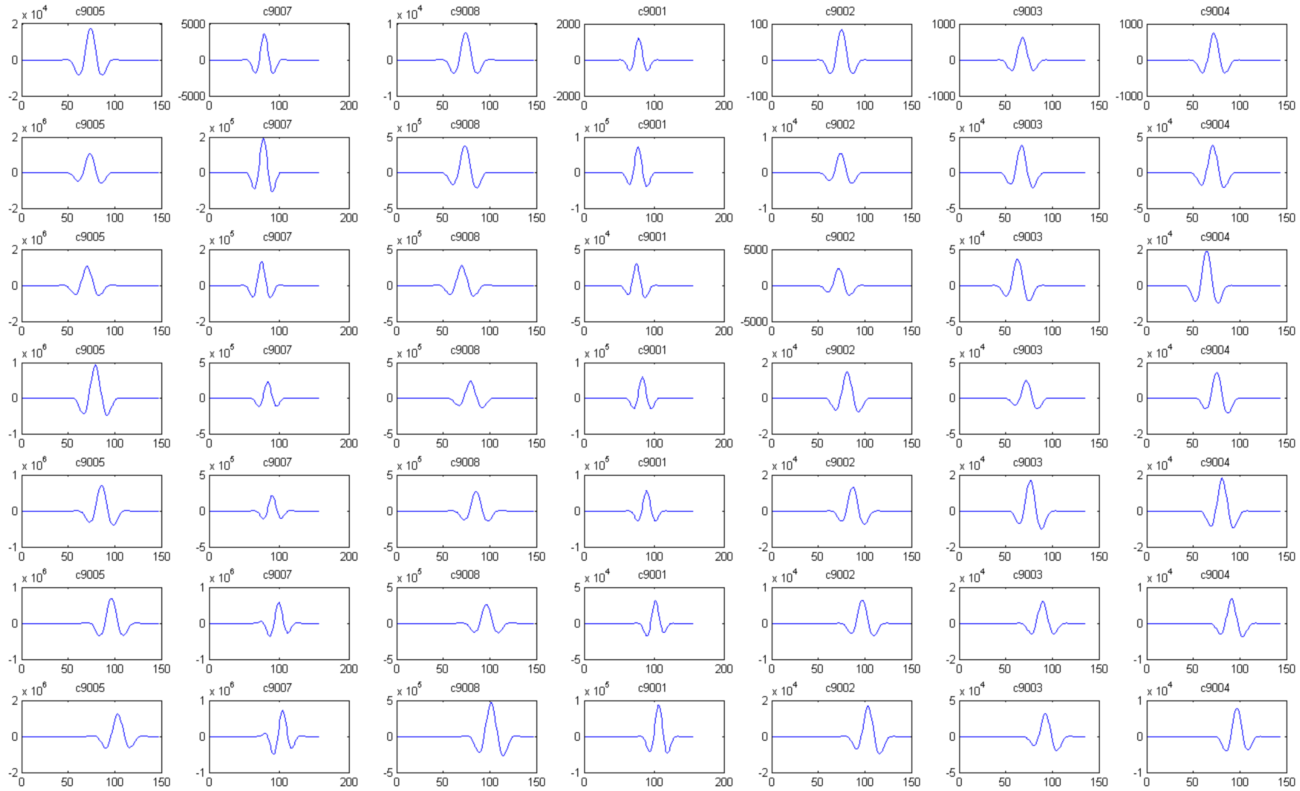

Figure 16: Cross-correlation of data recorded at the first depth level.

Table 5: Index of the maximum correlation of the first arrivals. (Continued on next page)

Ring 1`	Elevation	FFID9001	FFID9002	FFID9003	FFID9004	FFID9005	FFID9007	FFID9008
Sensor 1	203.835	78	75	68	72	74	79	74
Sensor 3	200.177	77	74	67	71	73	78	73
Sensor 4	179.131	75	72	63	64	70	75	70
Sensor 5	155.981	83	81	72	75	79	84	79
Sensor 6	133.06	89	87	76	81	86	90	85
Sensor 7	109.926	102	97	90	91	96	100	96
Sensor 8	87.02	107	103	92	97	103	105	101
Ring 2	Elevation	FFID9010	FFID9011	FFID9012	FFID9013	FFID9015	FFID9016	
Sensor 1	68.854	46	43	48	48	46	49	
Sensor 3	65.197	45	43	48	48	46	48	
Sensor 4	44.882	46	44	48	50	47	50	
Sensor 5	21.671	50	48	52	54	51	55	
Sensor 6	-1.036	56	54	58	60	57	61	
Sensor 2	-23.957	62	60	65	65	63	65	
Sensor 8	-47.366	67	65	69	69	68	71	
Ring 3	Elevation	FFID9017	FFID9018	FFID9020	FFID9022	FFID9023		
Sensor 1	-65.532	46	45	45	47	47		
Sensor 3	-69.19	44	43	44	45	45		
Sensor 4	-90.465	39	37	37	39	40		
Sensor 5	-113.386	49	48	48	50	50		
Sensor 6	-136.489	54	52	53	55	53		
Sensor 2	-159.365	67	66	67	69	67		
Sensor 8	-182.27	67	66	67	69	67		
Ring 4	Elevation	FFID9028	FFID9029	FFID9030	FFID9031			
Sensor 1	-133.06	37	36	46	34			
Sensor 3	-136.718	37	36	46	33			
Sensor 4	-206.548	50	47	59	46			
Sensor 5	-228.935	56	53	65	51			
Sensor 6	-251.811	60	57	70	56			
Sensor 2	-274.564	65	62	75	62			
Sensor 8	-297.972	71	69	81	67			

Table 5: (Continued) Index of the maximum correlation of the first arrivals.

Ring 5	Elevation	FFID9026	FFID9029	FFID9030	FFID9031
Sensor 1	-133.182	39	38	32	44
Sensor 3	-136.84	40	19	32	46
Sensor 4	-321.975	72	45	63	77
Sensor 5	-335.646	79	53	70	85
Sensor 6	-348.813	82	55	73	87
Sensor 2	-362.224	87	60	78	92
Sensor 8	-375.422	89	63	80	94

Ring 6	Elevation	FFID9026	FFID9027	FFID9028	FFID9029	FFID9030
Sensor 1	-133.289	1	1	69	51	66
Sensor 3	-136.947	1	57	59	59	70
Sensor 4	-390.418	58	89	90	63	100
Sensor 5	-403.83	69	100	101	74	111
Sensor 6	-416.418	70	100	102	74	112
Sensor 2	-429.814	78	109	111	83	120

Notice that index of sensor 1 and 3 were very similar, which indicated time shift between the two sensors was almost zero. There are several possible causes of this unreasonable phenomenon, one being that the offset was big compared to the receiver depth. Sensors were at ~115meters below surface whereas source offset was ~150meters, therefore ray path could propagate toward horizontal after refraction and could reach borehole receivers almost at the same time. Second reason could be related with receiver array: only sensor 1 and 3 were deployed at a shallower depth at only 3 meters interval, it is possible that the wave peak happened to be recorded by lower such that one would easily conclude that the wave reached the lower sensor first. A third possible reason that could explain this is the issue of clock-drift-correction: each borehole sensor had its own built-in clock for recording time. However, due to the lack of clock-drift information, nothing could be done to correct the time and data recorded by sensor 1 and sensor 3 was omitted in most analysis.

Average Velocity Calculation

Borehole seismic data if properly recorded is the best tool used to determine wave propagation velocity by simply picking the first arrivals recorded at different depth levels (Mari 2003). Compared to surface seismic data where the accuracy of the subsurface information is limited by the vertical resolution, in borehole seismic survey, one can expect more detailed subsurface information. Time shift of first arrivals between successive sensors could be calculated simply by: t=index(i)-index(i-1) (Appendix A). Table 6 is the calculation result of time shift t. There is high consistency of time shift between two receivers whatever the shot was. This indicates less subsurface anisotropy within borehole depth. For example, time shift between sensor 4 and 5 at the first depth level was 9ms with six different sources applied.

Table 6: Time shift between successive traces and estimated travel time (in ms). (Continued on next page)

Ring 1	Sensor Elevation	Sensor_Distance(m)	9001	9002	9003	9004	9005	9007	9008	Time Shift
Sensor 4-5	179.131~155.981	23.15	8	9	9	9	9	9	9	9
Sensor 5-6	155.981~133.06	22.92	6	6	5	6	5	6	6	6
Sensor 6-7	133.06~109.926	23.13	11	10	14	10	10	10	11	10
Sensor 7-8	109.926~87.02	22.91	5	6	2	6	7	5	5	6
Ring 2	Sensor Elevation	Sensor_Distance(m)	9010	9011	9012	9013	9015	9016		Time Shift
Sensor 4-5	44.882~21.671	23.21	4	4	4	4	4	5		4
Sensor 5-6	21.671~(-1.036)	22.71	6	6	6	6	6	6		6
Sensor 6-2	-1.036~(-23.957)	22.92	8	6	7	5	6	4		6
Sensor 2-8	-23.957~(-47.366)	23.41	5	5	4	4	5	6		5
Ring 3	Sensor Elevation	Sensor_Distance(m)	9017	9018	9020	9022	9023			Time Shift
Sensor 4-5	-90.465~(-113.386)	22.92	10	11	11	11	10			11
Sensor 5-6	-113.386-(-136.489)	23.10	5	4	5	5	3			5
Sensor 6-2	-136.489-(-159.365)	22.88	13	14	14	14	14			14
Ring 4	Sensor Elevation	Sensor_Distance(m)	9028	9029	9030	9031				Time Shift
Sensor 4-5	-206.548~(-228.935)	22.39	6	6	6	5				6
Sensor 5-6	-228.935~(-251.811)	22.88	4	4	5	5				4.5
Sensor 6-2	-251.811~(-274.564)	22.75	5	5	5	6				5
Sensor 2-8	-274.564~(-297.972)	23.41	6	7	6	5				6

Table 6: (Continued) Time shift between successive traces and estimated travel time (in ms).

Ring 5	Sensor Elevation	Sensor_Distance(m)	9026	9029	9030	9031		Time Shift
Sensor 4-5	-321.975~(-335.646)	13.67	7	8	7	8		7.5
Sensor 5-6	-335.646~(-348.813)	13.17	3	2	3	2		2.5
Sensor 6-2	-348.813~(-362.224)	13.41	5	5	5	5		5
Sensor 2-8	-362.224~(-375.422)	13.20	2	3	2	2		2
Ring 6	Sensor Elevation	Sensor_Distance(m)	9026	9027	9028	9029	9030	Time Shift
Sensor 4-5	-390.418~(-403.83)	13.41	11	11	11	11	11	11
Sensor 6-2	-416.418~(-429.814)	13.40	8	9	9	9	8	9

The travel time measured above together with depth of recording sensors offered a way of calculating velocity by simply: V_a=receiver distance/time shift. However, this velocity is typically measured along the line of receivers which is different from the direction of wave-front thus only represents apparent velocity symbolized by V_a. The results of V_a were shown in Table 7.

Table 7: Apparent velocity between successive traces (in m/s). (Continued on next page)

Ring 1	Sensor_Distance(m)	Time Shift(ms)	Apparent Velocity(m/s)
Sensor 4-5	23.15	9	2572
Sensor 5-6	22.92	6	3820
Sensor 6-7	23.13	10	2313
Sensor 7-8	22.91	6	3818
Ring 2	Sensor_Distance(m)	Time Shift(ms)	Apparent Velocity(m/s)
Sensor 4-5	23.21	4	5803
Sensor 5-6	22.71	6	3785
Sensor 6-2	22.92	6	3820
Sensor 2-8	23.41	5	4682
Ring 3	Sensor_Distance(m)	Time Shift(ms)	Apparent Velocity(m/s)
Sensor 4-5	22.92	11	2084
Sensor 5-6	23.10	5	4621
Sensor 6-2	22.88	14	1634
Ring 4	Sensor_Distance(m)	Time Shift(ms)	Apparent Velocity(m/s)
Sensor 4-5	22.39	6	3731
Sensor 5-6	22.88	4.5	5084
Sensor 6-2	22.75	5	4551
Sensor 2-8	23.41	6	3901

Table 7: (Continued) Apparent velocity between successive traces (in m/s).

Ring 5	Sensor_Distance(m)	Time Shift(ms)	Apparent Velocity(m/s)
Sensor 4-5	13.67	7.5	1823
Sensor 5-6	13.17	2.5	5267
Sensor 6-2	13.41	5	2682
Sensor 2-8	13.20	2	6599
Ring 6	**Sensor_Distance(m)**	**Time Shift(ms)**	**Apparent Velocity(m/s)**
Sensor 4-5	13.41	11	1219
Sensor 6-2	13.40	9	1488

However, to identify the real rock velocity the source offset and shot angle must be taken into consideration. Equation 2 was used to determine source offset, and Equation 3 and Equation 4 were used to determine shot angle (Appendix B). Table 8 is the calculation result of each source-receiver offset. Notice that offset from sources in the same ring pattern varied very slightly by only several meters, to make the later calculation easier the author took the average of offsets in the same ring such that each depth array had only one constant offset. Table 9 shows the calculation result of shot angle. Shot angle determines the direction of wave-front propagation if we assume the wave is propagating straight, and it also determines the relationship of apparent velocity and real rock velocity. Equation 5 in Appendix B was used to calculate real rock velocity, and the result was shown in Table 10.

Table 8: Estimation of offset for deployment of each source-receiver pair.

Ring1	FFID9001	FFID9002	FFID9003	FFID9004	FFID9005	FFID9007	FFID9008	Average Offset(m)
offset(m)	146.07	153.68	156.88	151.53	151.11	172.79	160.60	156.09
Ring2	FFID9010	FFID9011	FFID9012	FFID9013	FFID9015	FFID9016		Average Offset(m)
offset(m)	305.58	308.03	304.37	344.61	307.38	301.12		311.85
Ring3	FFID9017	FFID9018	FFID9020	FFID9022	FFID9023			Average Offset(m)
offset(m)	452.04	438.50	459.90	457.05	460.79			453.66
Ring4	FFID9028	FFID9029	FFID9030	FFID9031				Average Offset(m)
offset(m)	609.34	669.44	614.42	614.04				626.81
Ring5	FFID9026	FFID9029	FFID9030	FFID9031				Average Offset(m)
offset(m)	610.35	669.444	614.418	614.044				627.06
Ring6	FFID9026	FFID9027	FFID9028	FFID9029	FFID9030			Average Offset(m)
offset(m)	610.35	609.584	609.337	669.444	614.418			622.63

Table 9: Estimation of shot angle based on homogenous isotropy scenario.

Ring1	sensor 1	sensor 3	sensor 4	sensor 5	sensor 6	sensor 7	sensor 8
tan(shot angle)	0.72	0.74	0.88	1.02	1.17	1.32	1.47
shot angle	35.63	36.51	41.19	45.66	49.48	52.82	55.68
Ring2	sensor 1	sensor 3	sensor 4	sensor 5	sensor 6	sensor 2	sensor 8
tan(shot angle)	0.80	0.81	0.88	0.95	1.03	1.10	1.17
shot angle	38.70	39.10	41.28	43.60	45.71	47.69	49.57
Ring3	sensor 1	sensor 3	sensor 4	sensor 5	sensor 6	sensor 2	sensor 8
tan(shot angle)	0.86	0.86	0.91	0.96	1.01	1.06	1.11
shot angle	40.55	40.81	42.32	43.86	45.34	46.73	48.06
Ring4	sensor 1	sensor 3	sensor 4	sensor 5	sensor 6	sensor 2	sensor 8
tan(shot angle)	0.71	0.72	0.83	0.87	0.90	0.94	0.98
shot angle	35.56	35.78	39.76	40.95	42.12	43.25	44.36
Ring5	sensor 1	sensor 3	sensor 4	sensor 5	sensor 6	sensor 2	sensor 8
tan(shot angle)	0.72	0.72	1.02	1.04	1.06	1.08	1.10
shot angle	35.61	35.84	45.49	46.10	46.67	47.24	47.79
Ring6	sensor 1	sensor 3	sensor 4	sensor 5	sensor 6	sensor 2	
tan(shot angle)	0.72	0.73	1.14	1.16	1.18	1.20	
shot angle	35.84	36.06	48.62	49.16	49.65	50.16	

Table 10: Determination of P-wave velocity.

Ring 1	Apparent Velocity(m/s)	sin(a)	Real Velocity(m/s)
Sensor 4-5	2572	0.72	1840
Sensor 5-6	3820	0.76	2904
Sensor 6-7	2313	0.80	1843
Sensor 7-8	3818	0.83	3153
Ring 2	Apparent Velocity(m/s)	sin(a)	Real Velocity(m/s)
Sensor 4-5	5803	0.69	4002
Sensor 5-6	3785	0.72	2709
Sensor 6-2	3820	0.74	2825
Sensor 2-8	4682	0.76	3564
Ring 3	Apparent Velocity(m/s)	sin(a)	Real Velocity(m/s)
Sensor 4-5	2084	0.69	1444
Sensor 5-6	4621	0.71	3287
Sensor 6-2	1634	0.73	1190
Ring 4	Apparent Velocity(m/s)	sin(a)	Real Velocity(m/s)
Sensor 4-5	3731	0.66	2445
Sensor 5-6	5084	0.67	3410
Sensor 6-2	4551	0.69	3118
Sensor 2-8	3901	0.70	2728
Ring 5	Apparent Velocity(m/s)	sin(a)	Real Velocity(m/s)
Sensor 4-5	1823	0.72	1313
Sensor 5-6	5267	0.73	3831
Sensor 6-2	2682	0.73	1969
Sensor 2-8	6599	0.74	4888
Ring 6	Apparent Velocity(m/s)	sin(a)	Real Velocity(m/s)
Sensor 4-5	1219	0.76	922
Sensor 6-2	1488	0.77	1143

Compare to Stacking Velocity

The velocities obtained from above processing were compared to the velocities obtained from surface 2D seismic records. Table 11 shows the pairs of two-way time and stacking velocities obtained from surface 2D seismic lines, Line 2a and Line 2b, that crossed over the wellhead. The wellhead location was CDP2174 on line 2a and CDP4174 on line2b. To compare two velocities, the first step was to convert stacking velocities to interval velocities using Dix

Equation (Equation 6 in Appendix C). 16 pairs of two-way time and stacking velocities were given allowing a determination of 15 interval velocities. The thickness of each layer could be calculated as the interval velocity multiplied by one-way travel time within that layer (Equation 7 in Appendix C). The interval velocity and the thickness of the nth layer (n=1~15) were thus obtained and the results were shown in Table 12. Considering the length of the borehole array (750m), only velocities in the red squares would be used.

Table 11: Stacking velocities obtained from surface 2D seismic lines. Wellhead location is CDP2174 on line 2a and CDP4174 on line 2b.

Line 2a CDP_2174	Two-way Time (ms)	0	142	258	355	460	550	628	676
	Stacking Velocity (m/s)	2438	2810	3426	3660	3695	3962	4171	4246
	Two-way Time (ms)	754	835	956	1039	1179	1259	1551	1760
	Stacking Velocity (m/s)	4393	4510	4695	4916	4970	5023	5837	5679
Line 2b CDP_4174	Two-way Time (ms)	0	161	260	367	455	540	645	749
	Stacking Velocity (m/s)	2438	2982	3644	3727	3761	4070	4198	4329
	Two-way Time (ms)	830	948	1020	1157	1250	1359	1473	1646
	Stacking Velocity (m/s)	4416	4586	4789	4732	5018	5089	5129	5405

Table 12: Interval velocities calculated from stacking velocities using Dix Equation. Data in the red square is only used since it covered the total length of borehole array (750m).

Line_2a CDP_2174	layer	1	2	3	4	5	6	7	8
	Interval Velocity (m/s)	2810	4054	4219	3810	5113	5420	5127	5505
	One-way Time (ms)	71	58	49	53	45	39	24	39
	Thickness (m)	200	235	205	200	230	211	123	215
	Depth (m)	200	435	639	839	1069	1281	1404	1618
	layer	9	10	11	12	13	14	15	
	Interval Velocity (m/s)	5480	5813	6973	5353	5747	8496	4329	
	One-way Time (ms)	41	61	42	70	40	146	105	
	Thickness (m)	222	352	289	375	230	1240	452	
	Depth (m)	1840	2192	2482	2856	3086	4327	4779	
Line_2b CDP_4174	layer	1	2	3	4	5	6	7	8
	Interval Velocity (m/s)	2982	4518	3921	3899	5433	4802	5066	5151
	One-way Time (ms)	81	50	54	44	43	53	52	41
	Thickness (m)	240	224	210	172	231	252	263	209
	Depth (m)	240	464	673	845	1076	1328	1591	1800
	layer	9	10	11	12	13	14	15	
	Interval Velocity (m/s)	5638	6927	4283	7737	5841	5583	7346	
	One-way Time (ms)	59	36	69	47	55	57	87	
	Thickness (m)	333	249	293	360	318	318	635	
	Depth (m)	2133	2382	2675	3035	3354	3672	4307	

Figure 17 shows the comparison of the velocities obtained from borehole seismic data to that obtained from surface 2D lines. Depth was plotted at vertical axis from 0 to 750m, covering the whole borehole array. According to the driller’s information, from surface to a depth of 174m are glacial tills, shale and sandstone, 174m to 194m is Berea sandstone, 194m to 700m is Ohio shale, and below is Big lime of 400m in thickness. Borehole data offered 21 interval velocities of more detailed variations in the subsurface whereas surface stacking velocities offered only 4 velocities within the same depth. At the depth of ~200m both borehole data and surface data showed the similar features of velocity increase, and at the depth of ~480m both two results showed velocity decrease.

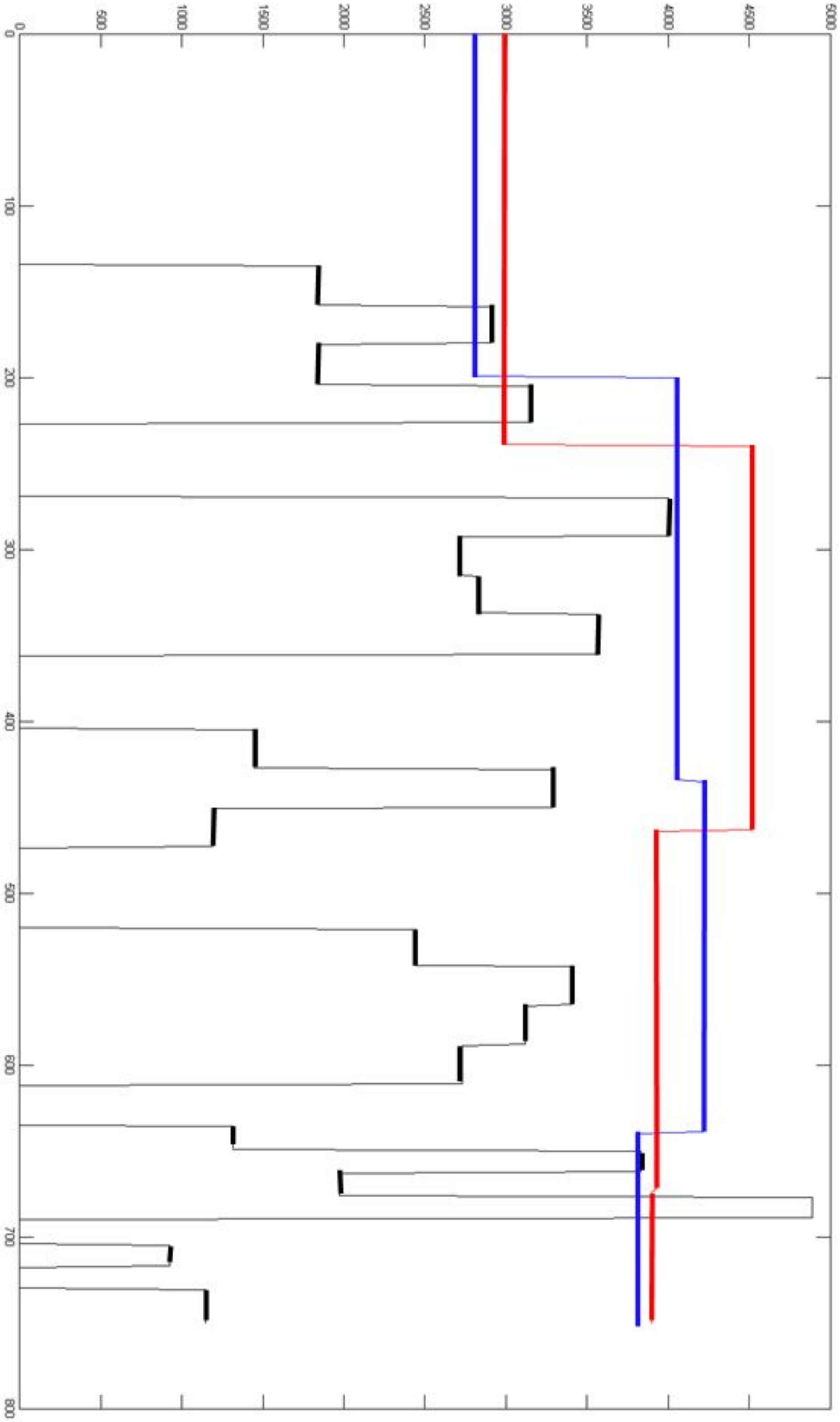

Figure 17: Compare velocities from borehole seismic data with velocities from surface seismic data. Y-axis is depth in meters from the ground level and X-axis is velocities in m/s. Black: velocities from borehole seismic data. Blue: velocities from surface line 2a. Red: velocities from surface line 2b.

Up-going Reflections

Although the initial purpose of the check-shot survey was to determine wave propagation velocity with focuses only on first breaks, the author tempted to process the data as an offset VSP (vertical seismic profile) in order to get as much subsurface information as possible. To do this, a shot-gather data file was created by the author on MATLAB from the data recorded at the lowest two arrays that had the common source location. Figure 18 shows such a shot gather record of 9 traces at regular receiver interval of 14meters. Traces 1 to 5 were data recorded at the fifth depth level from 636.97m to 690.42m in depth, and traces 6-9 were data at the sixth depth level from 705.42m to 733.81m in depth. Two arrays were both sourced by FFID9030 but in different days. Secondary trace header was receiver depth relative to ground level and was labeled at the top of every other trace. Spatial change of receivers was also illustrated as the receiver-depth header plot at the top of display. In such a check-shot survey, more energy may be input to the down-going wavelet as the geophone depth increases so that first break amplitudes are very well maintained, however, late arriving reflections are barely detected.

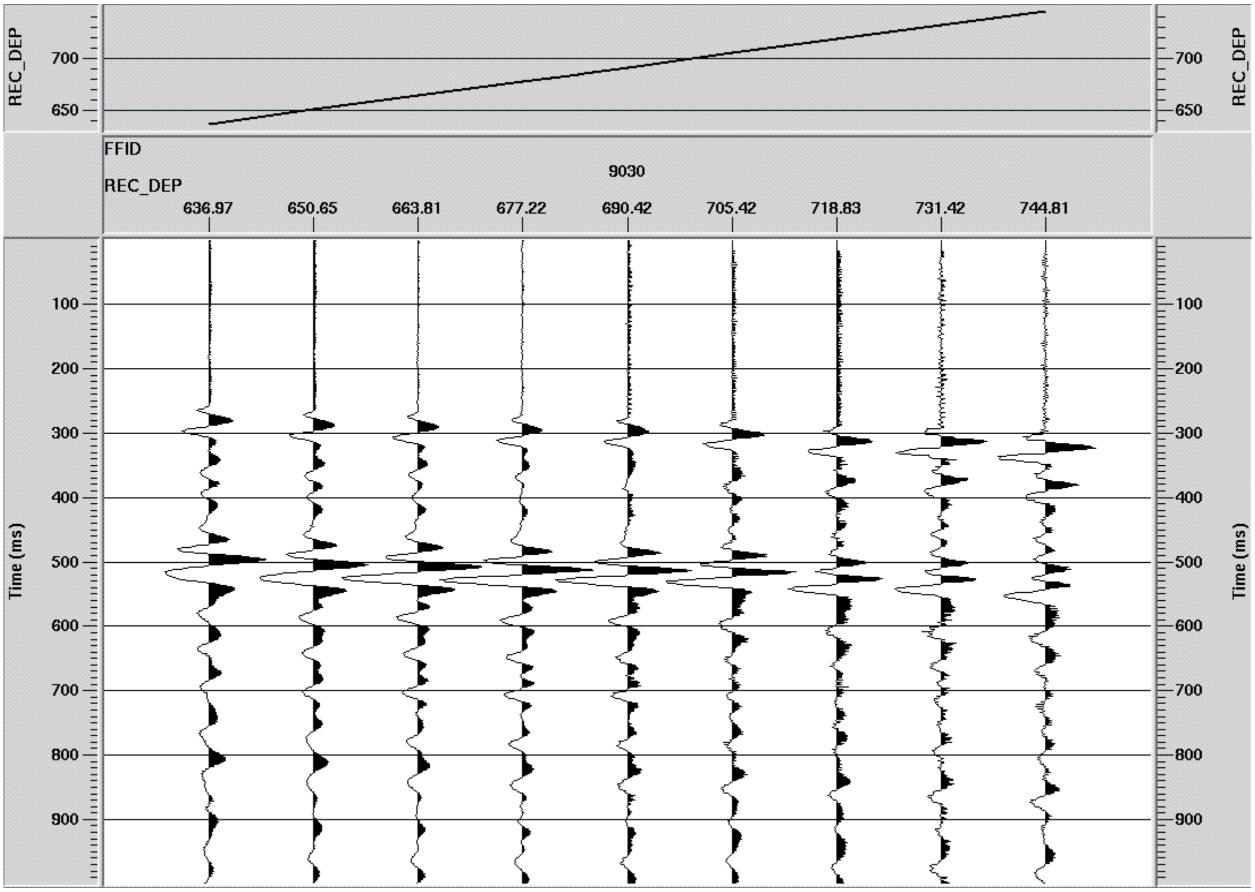

Figure 18: Raw shot gather with FFID9030 from the lowest two depth arrays.

Bandpass Filtering

A zero phase Ormsby bandpass filtering of 10-50Hz was applied on the raw shot data to remove background noise and resulted in a seismic section with better developed wave forms, shown in Figure 19. Different types of seismic events together with approximate propagation velocity were marked on corresponding traces illustrated in the lower plot. The first occurring seismic events at 250ms-330ms were first arrivals propagating downward at a velocity of 2800m/s approximately. The later seismic events occurring at 400ms-430ms was identified as tube waves generated by borehole fluids at a propagation velocity of 1437m/s. The tube waves were reflected from ~705.43meters at 500ms-600ms at a velocity of 1447m/s and recorded by upper sensors. At the depth of 2297ft (700m) was the top of a formation called “big lime” with high velocity, where reflected waves should originate, however, one can hardly tell primary reflections due to very weak amplitudes.

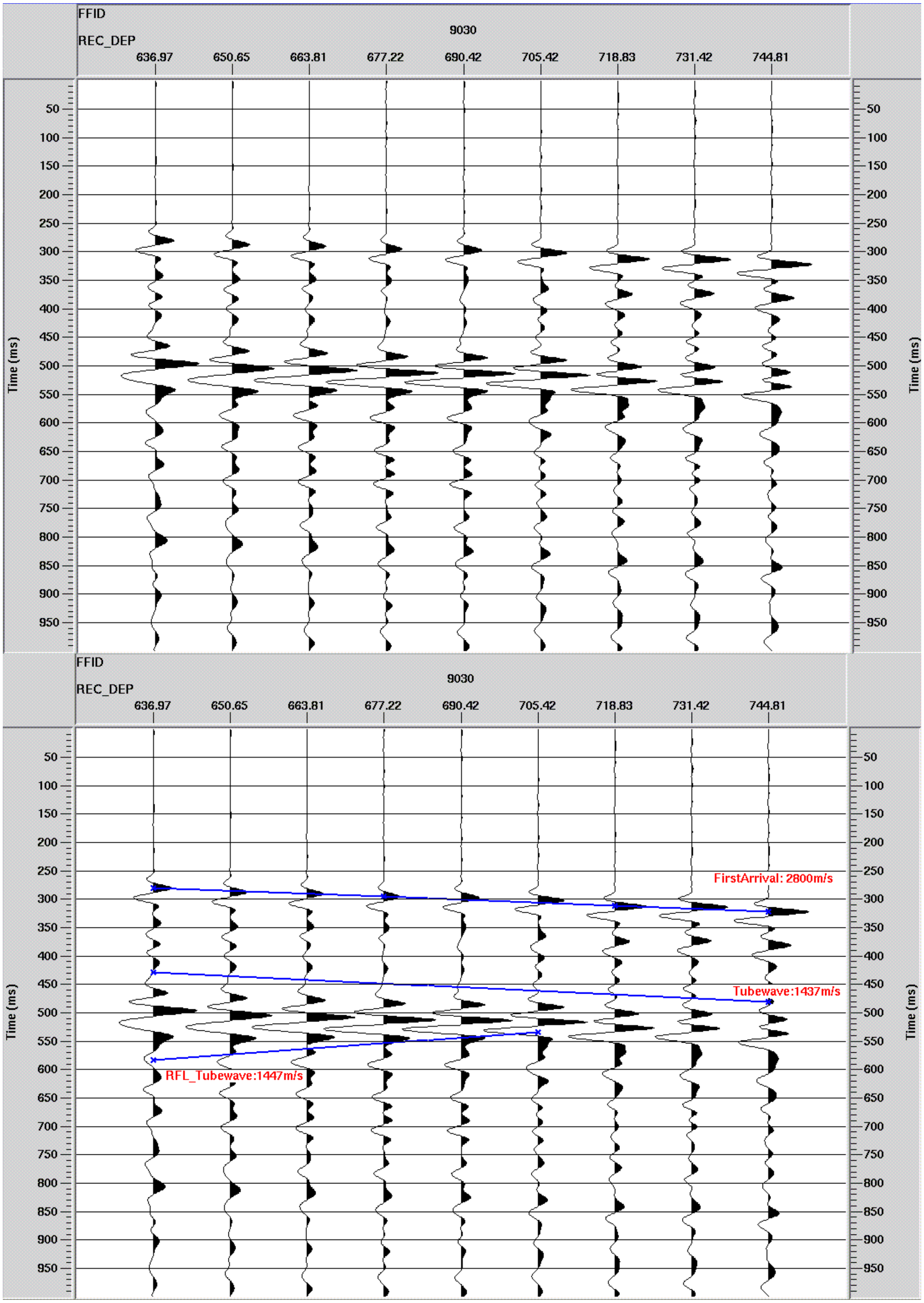

Figure 19: Seismic section with FFID9030 with 10-50Hz bandpass filtering applied. The lower one shows different seismic events and their propagation velocities.

Trace Mute

With focuses on only primary reflections which should locate on a regime between first breaks and the onset of noise, two mutes were picked to zero all the data outside the regime, shown as the upper plot in Figure 20. With the two mutes applied on the data the area above the first break was zeroed using the top mute and area below noise onset was zeroed using the bottom mute. The lower plot in the figure is the result of the mutes. Both high amplitude first breaks and tube waves were absent and only small amplitude events which should contain up-going reflections were left.

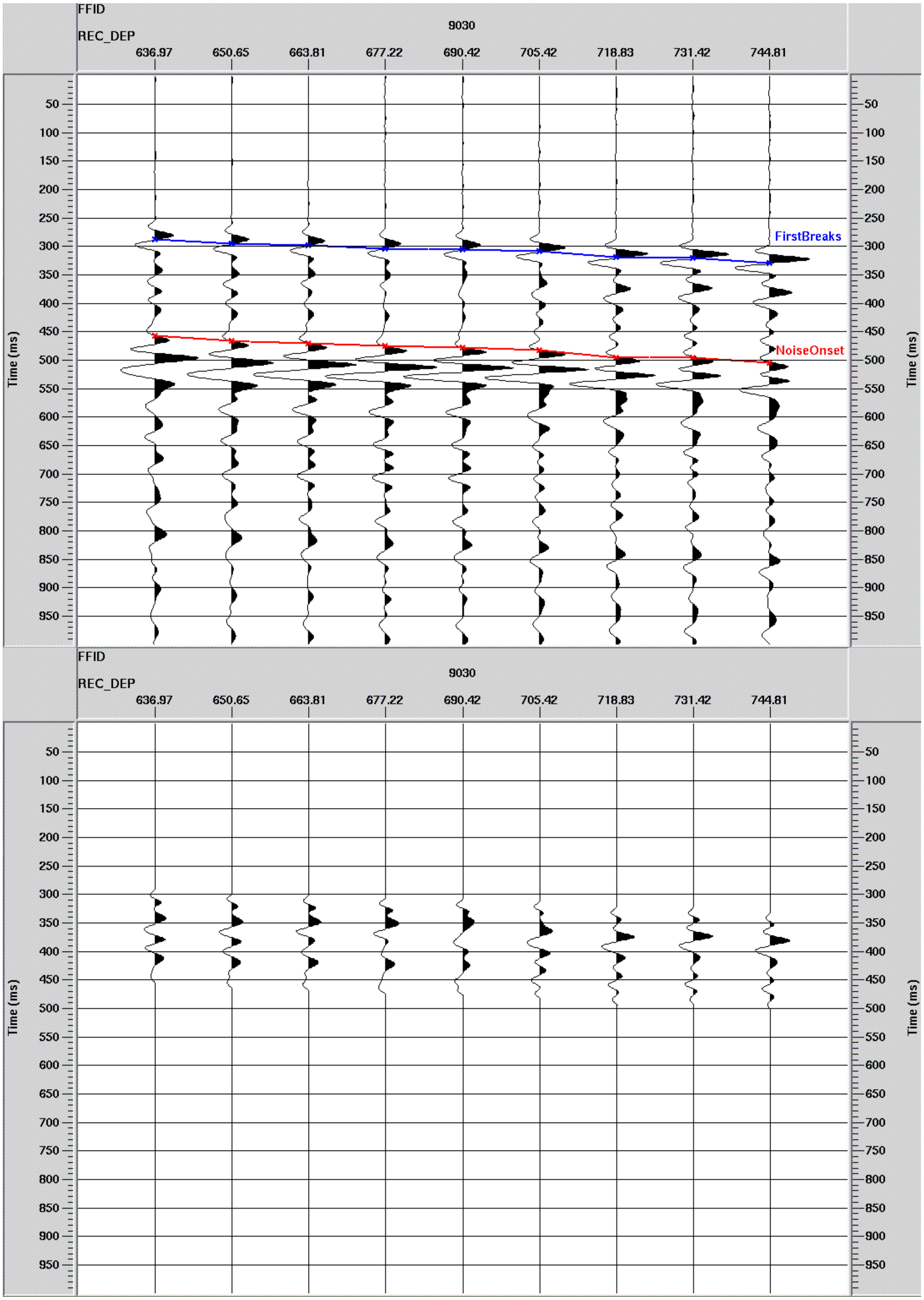

Figure 20: FFID9030's Trace Mute processing with top mute at first break and bottom mute at noise onset. The lower plot is the result of trace mute processing.

FK Filtering

Another effort made in order to track up-going reflections was to apply FK filtering on the muted data. This can be done based on the fact that two seismic events that may overlap rendering multiplicative filtering impossible in one dimension do not overlap in the two-dimension in both the F and K. Since a dipping straight line in TX transforms to a dipping straight line in FK, events having certain dips between two values in the TX domain can be removed by multiplying the FK transform of the data with a transform which is zero between the corresponding dips in the FK domain and one elsewhere. This fact provides FK filtering as a means of separating borehole seismic events depending on the direction that the waves travel and a way of filtering to suppress unwanted events such as low velocity tube waves on the basis of their apparent velocity. In borehole seismic data, reflections were propagating upward which had the opposite dip from down-going first arrivals thus they fall within different zones of the plot in FK domain. Down-going first arrivals that travel across the spread away from the source will plot in the positive wave-number field while up-going reflections travelling towards the source will plot in the negative wave-number field.

FK filtering involves applying a filter for the events in a FK plot by choosing a polygon to indicate the region to which they are applied. The type of FK filtering used was a reject for the event the polygon encompasses. A polygon was chosen on the side of the positive wave numbers of almost all down-going events including the first arrivals and down-going tube waves using the FK analysis processor. Figures 21 illustrates the reject polygon chosen. It can be seen all down-going seismic events were on the right side not corresponding to up-going reflections. Steepness in the TX domain or large values of dx/dt corresponds to shallowness in the FK domain. Therefore the less steeper first arrivals in the shot gather corresponds to the more steeper FK values (upper plot in the figure), and the steeper tube waves in the shot gather corresponds to the more horizontal FK values (the lower plot in the figure). The polygon was also chosen a little bit on the left side around the center of FK which corresponds to seismic waves with infinite velocities to destruct possible reflected steel casing waves.

This polygon covered almost the whole area of the side of the plot with positive wave numbers which if applied, should attenuate most down-going events and enhance 100% primary events. The result of this FK filter processing was shown in Figure 22. Due to the weak amplitudes, up-going reflections were still hard to detect even with FK filtering applied.

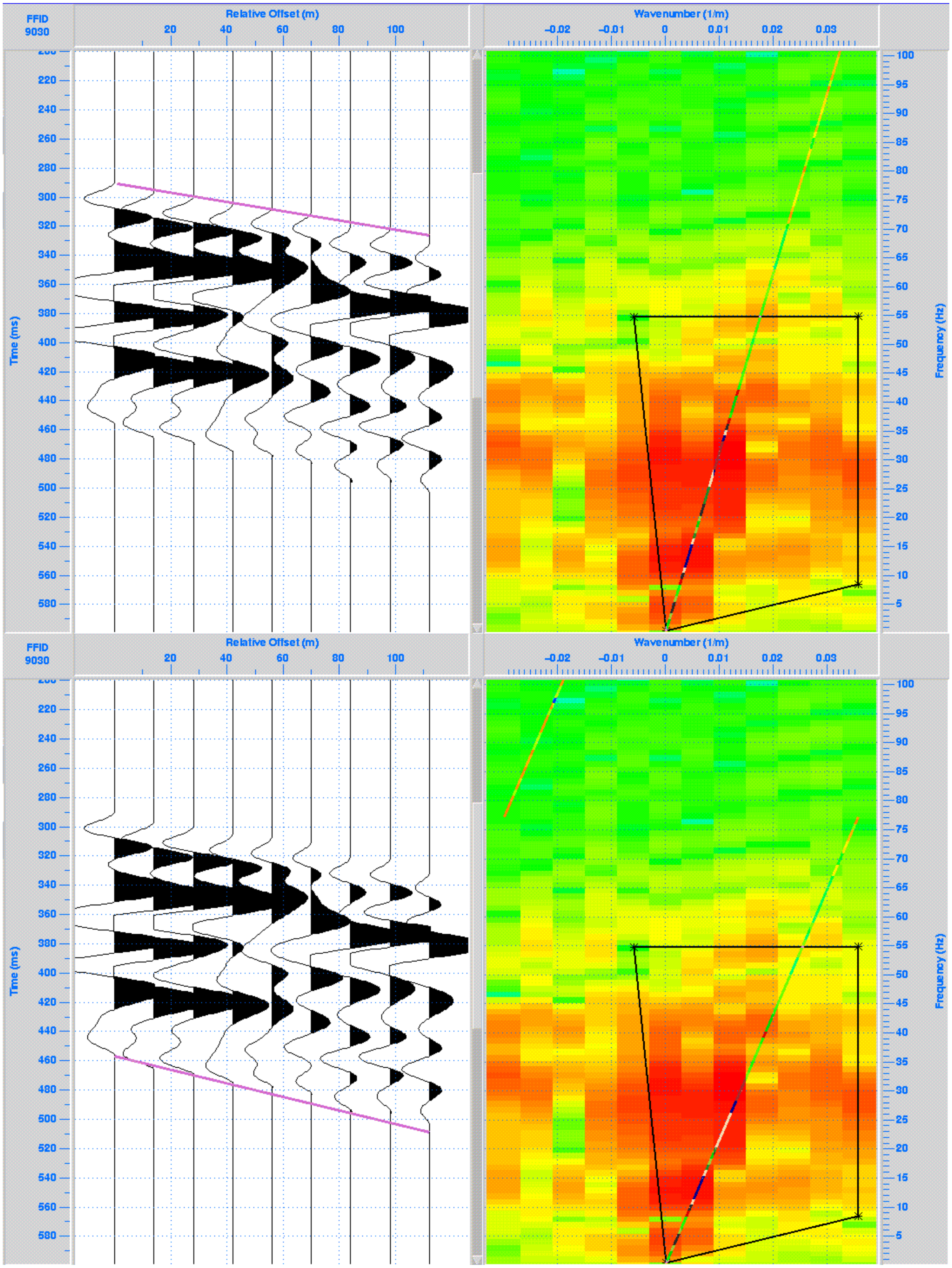

Figure 21: (FFID9030) FK analysis with a FK filter polygon with positive wavenumber. The upper one corresponds to first arrivals and the lower one is low velocity tube waves.

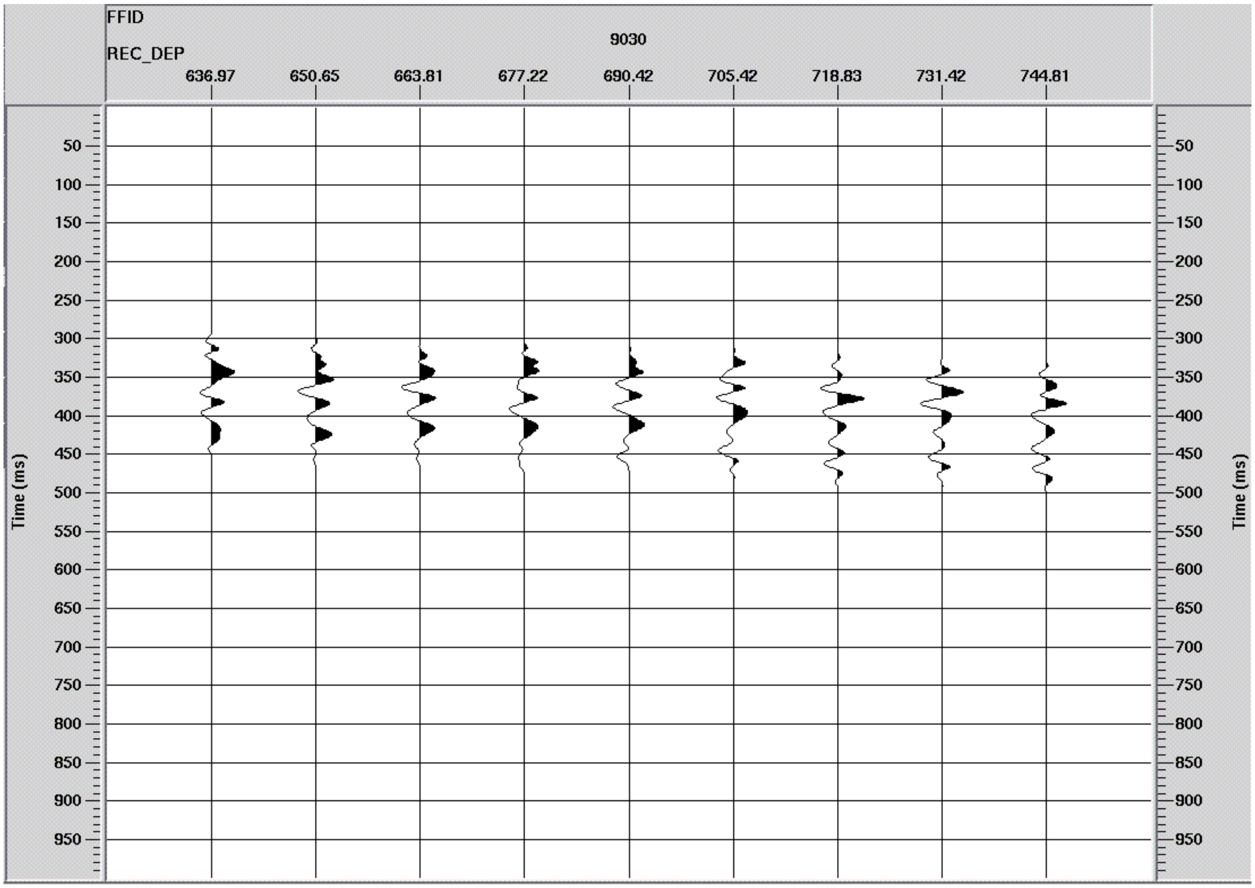

Figure 22: FFID9030 section after FK filtering with most down-going events destructed.

Normal Move-out Correction and Static Time Shifting

After FK filtering, all up-going events should be separated and they were the only part that the rest of the processing would be applied on. Since the strong reflector Big Lime existed at 2297ft (700m) depth below surface, the expected reflection should originate from 700m and reflected upward to the surface so the rest processing used to enhance reflections would be only applied on traces that were recorded above 700m, i.e. channel 1 through channel 5 in the seismic display. Figure 23 shows such a seismic display of 5 traces created by killing the rest of traces with a Trace Editing processor.

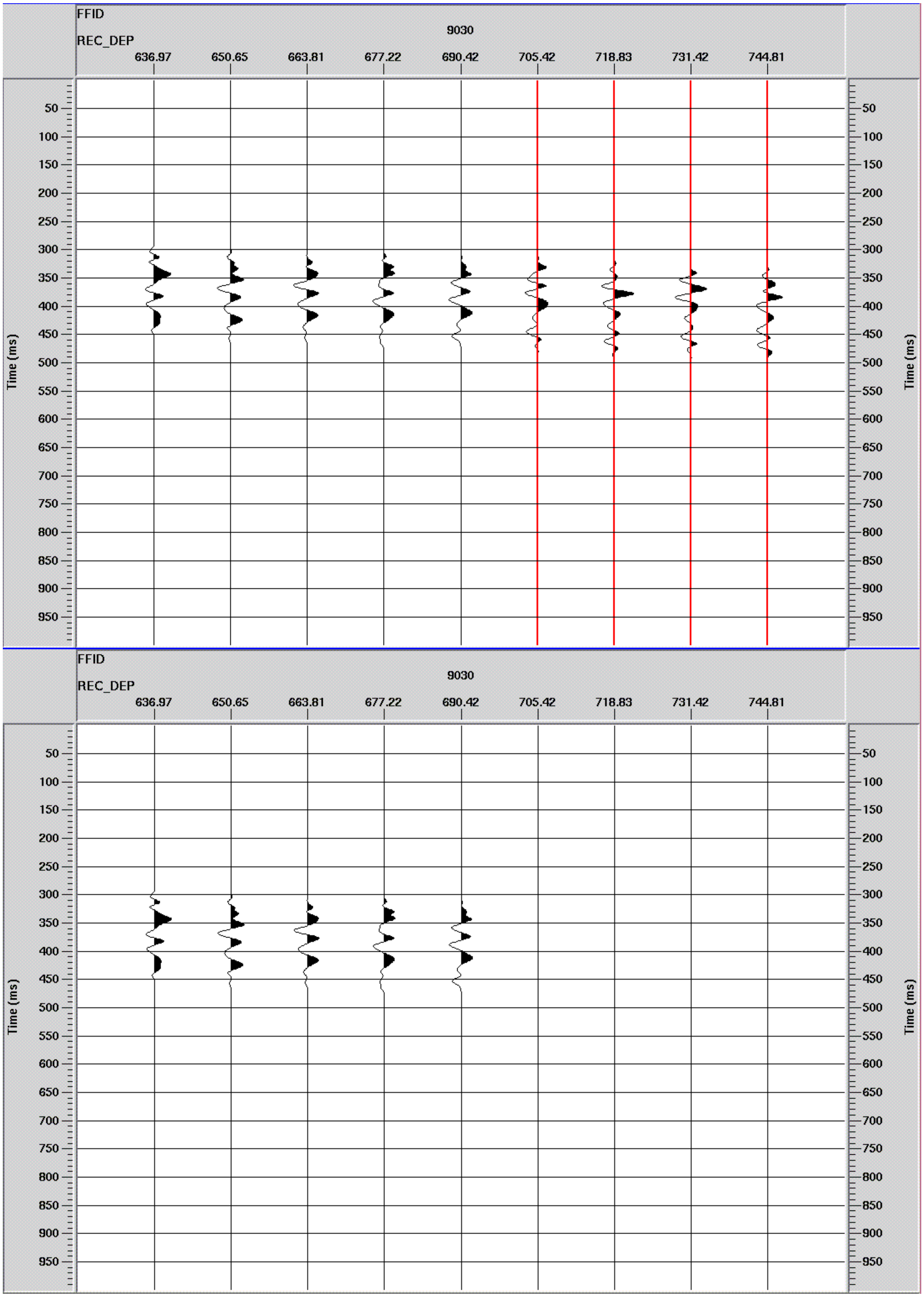

Figure 23: Lower one is the FFID9030 section of up-going events recorded above 700m. Upper one shows the killing processing that was applied.

As NMO correction that is applied in the conventional surface-recorded seismic data, in the VSP, when source was shot at a far offset distance from the wellhead, it is also necessary to apply NMO correction on the data before stacking is made. As a result of this the offset VSP section is transformed to zero-offset VSP section such that the time of seismic events would represent the wave transmitted and reflected vertically. Figure 24 illustrates the steps followed in correcting the reflected arrivals to normal incidence time.

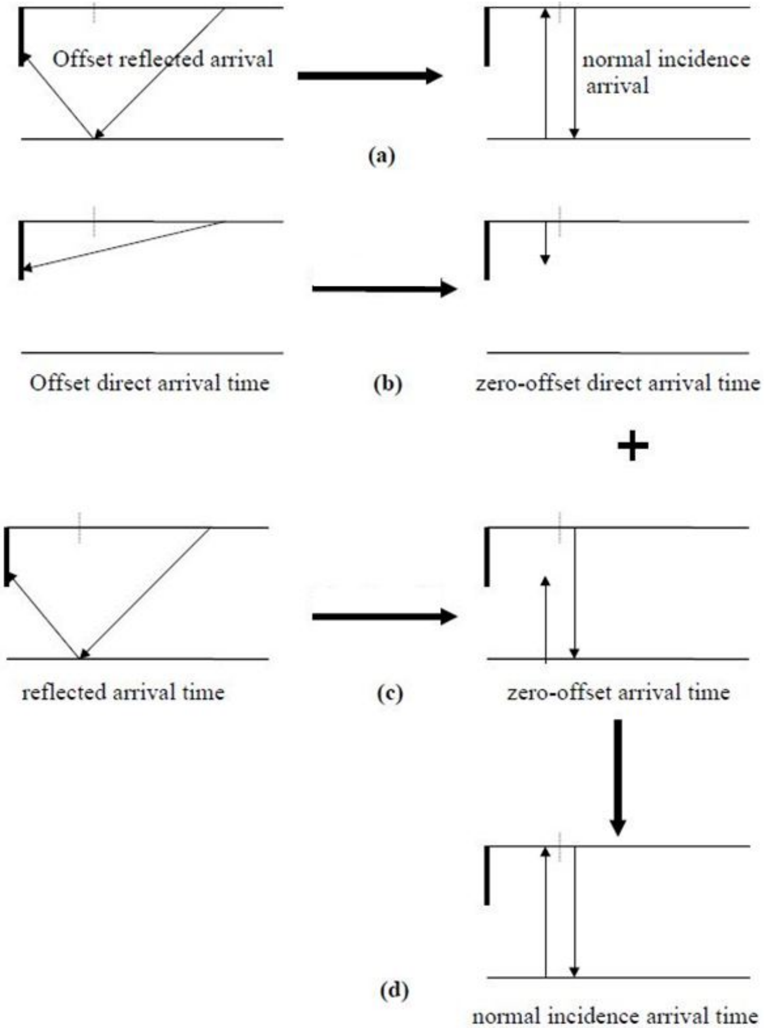

Figure 24: Steps followed to correct NMO in VSP data. (a) The objective is to correct the arrival time of the reflected wave to a normal incidence time. (b) Correct the direct arrivals to a zero-offset time. (c) Correct the reflected wave arrival time at the receiver to zero-offset reflection time. (d) Adding the results of (b) and (c) then gives the normal incidence time for the reflected event **(Gulati 1997)**.

Following the steps shown above a ray tracing method together with the RMS velocity determined from picking the first break was applied to calculate approximate NMO correction (Appendix D). Equation 8 through Equation 11 were used to calculated NMO correction C_1 needed to convert direct arrival to zero offset (Appendix D). Equation 12 through Equation 14 were used to calculated NMO correction C_2 needed to convert offset VSP reflection to zero offset VSP reflection (Appendix D). The total NMO needed to convert borehole-recorded reflections to surface-recorded reflections was the sum of C_1 and C_2, shown in Table 13.

Table 13: Determination of NMO correction for each trace.

Sensor	Depth (m)	l (m)	y(m)	T_b	T_{0B}	C_1	T_r	T_{0r}	C_2	C_1+C_2
1	637	898	51	267	190	77	457	356	101	178
2	651	905	40	274	197	77	452	350	102	179
3	664	912	30	277	202	75	447	343	104	179
4	677	918	20	282	207	75	442	337	105	180
5	690	925	9	284	210	74	438	331	107	181

Total NMO correction determined from the above processing was to be applied on the traces. To do this, a Hand Statics processor in Promax was used with parameters in a format of: /primary header: secondary header: corresponding statics/. To make things easier both primary header and secondary header were selected as channel numbers: 1:1:178 /2:2:179 /3:3:179 /4:4:180 /5:5:181 /. The result of NMO correction is illustrated in Figure 25. In theory, after NMO correction, all up-going reflections from flat horizontal reflectors should be positioned to the zero-offset two-way-travel-time reflections recorded by surface geophones.

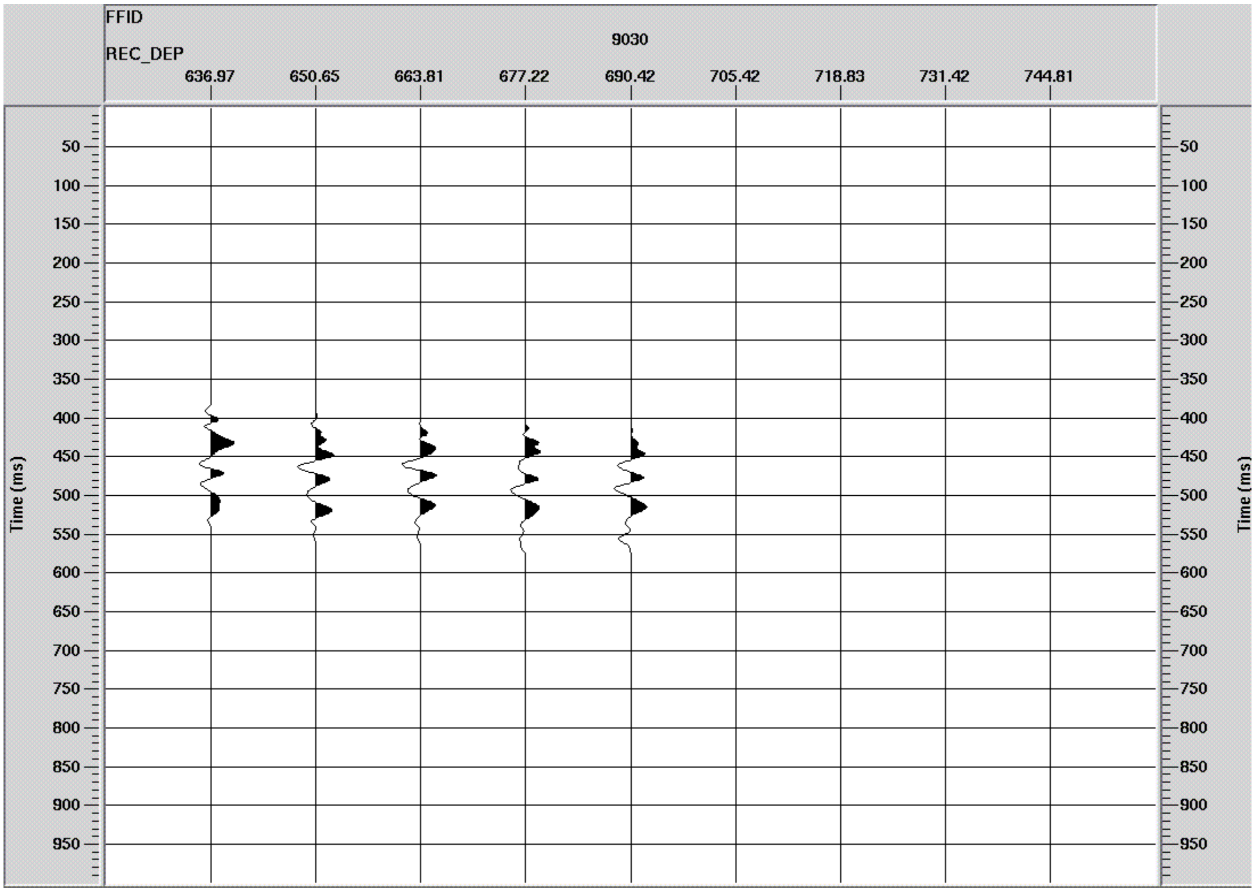

Figure 25: FFID9030 section after NMO correction.

Restricted Vertical Summation

The NMO corrected traces were then stacked vertically to create a composite trace with assumption that it aligned up-going reflections from horizontal strata in phase along equal time lines and other events misaligned. Vertical summing the set of NMO corrected traces will yield a single trace containing all up-going events and a small amount of contamination due to the out-of-phase summation of the down-going wavefields. The vertical summation resulted in composite trace shown in Figure 26, which should be an accurate estimate of all up-going primary reflections and contains little contamination from multiple reflections and other noise events.

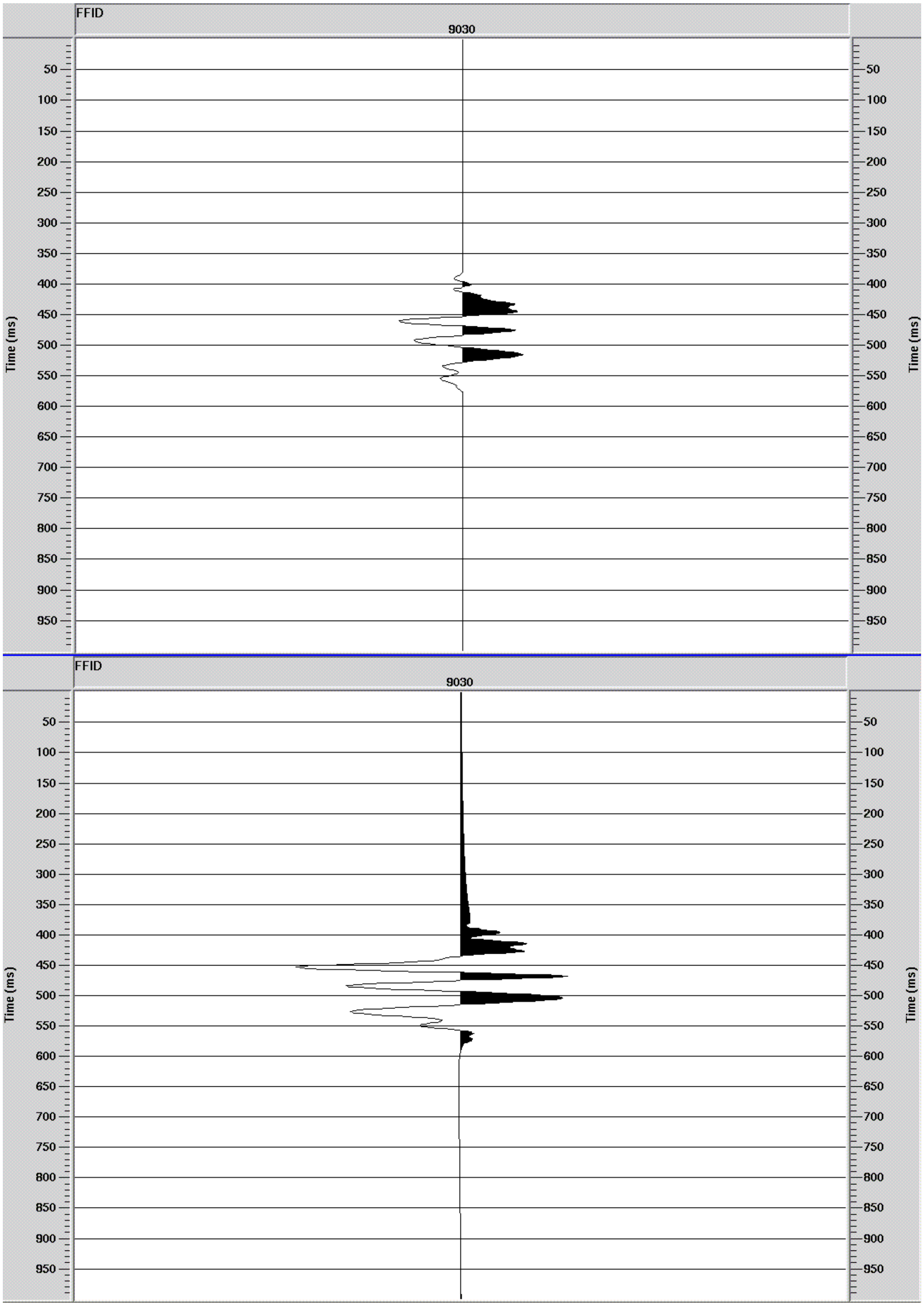

Figure 26: The composite trace obtained from restricted vertical summation of FFID9030. The data was muted and filtered to remove down-going events, shifted to vertically align up-going events, and vertically summed. The upper one is the raw stack. The lower one is the zero phase rotated section.

Tie to Surface Seismic Section

The main role of well seismic surveying is to tie surface seismic data in order to facilitate correlating up-going VSP reflections with events recorded at the surface. The processed VSP obtained from above processing was tied to a migrated surface seismic section as illustrated in Figure 27. Surface seismic data was collected at 2D surface seismic lines crossing over the wellhead and was processed and migrated by Wright Stated University. Tying was done in Promax using a processor named as Merge. To make comparison easier the single composite trace was repeated three times and insert in the middle between surface seismic trace at its real FFID position.

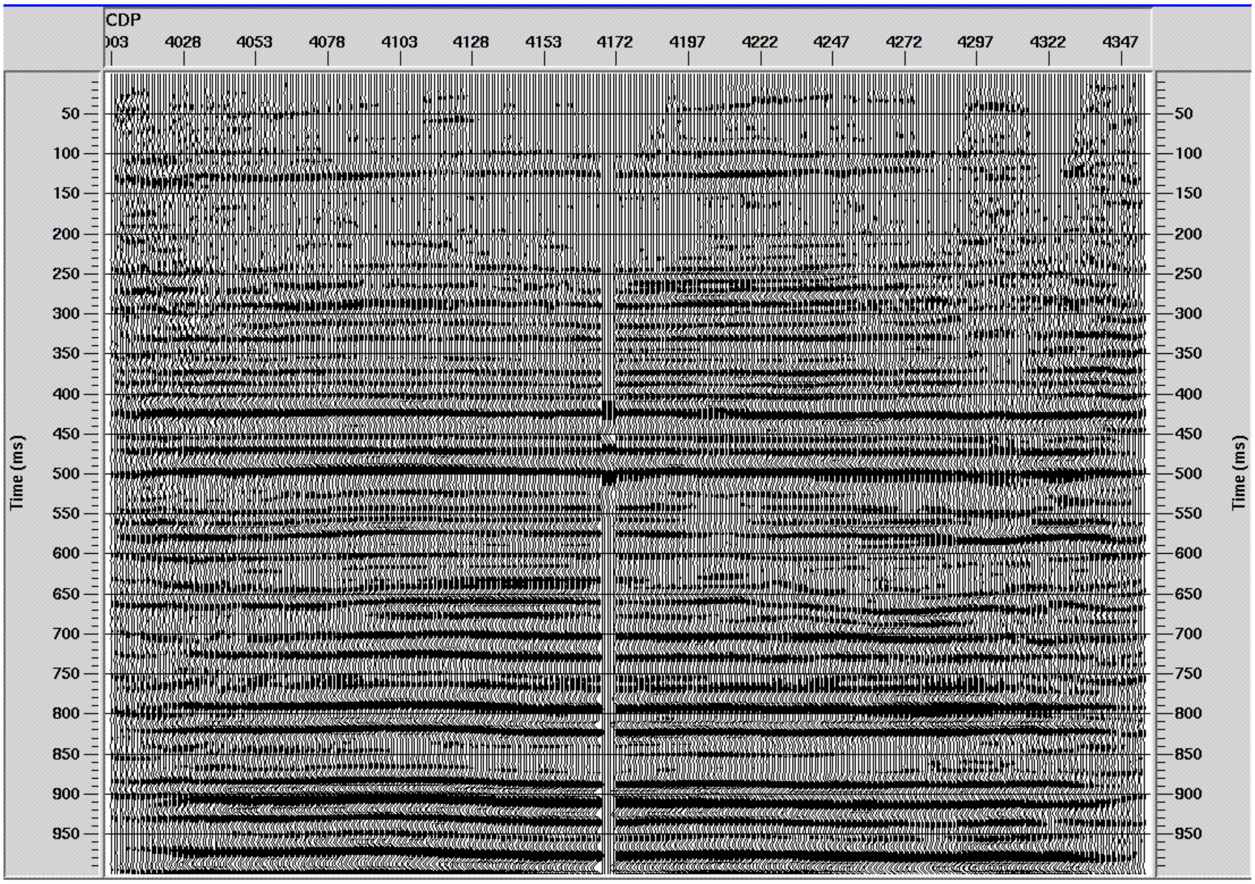

Figure 27: The composite trace obtained from restricted vertical summation of FFID9030 tied to surface seismic section. The VSP was plotted at the right position shown in the middle of the plot.

It can be seen that the pattern and shape of reflections of borehole records and surface records match very well, with only slight differences which might be due to the minimum to zero phase rotation. Three up-going VSP reflections correlated with surface recorded reflections in terms of time very well which occurred at 425ms, 475ms, and 500ms. From the results obtained at surface seismic data, 425ms and 500ms correspond to the top of Packer Shell and the top of Clinton Interval respectively.

IV Spectral Attributes

This section illustrates spectral analysis of beat test data recorded at surface with 3C broadband seismometers and data recorded in the borehole with a single 7-level array. Analysis was based on two spectral attributes: amplitude spectrum and V/H-ratio, completed in Geopsy. Geopsy allows data of types of formats such as miniseed, SEGY and etc. to be input and processed easily, however has a limitation of 65536 of data size for SEGY data. The data recorded at surface was given as 30min long miniseed data and the borehole data was given as one hour long Passcal SEGY format. Prior to processing the borehole data was converted to SEGY format and split into continuous time intervals of 1min data files. Data with clean signal before beats was extracted to show the background noise level to which the data after beats was compared. The change of spectral attributes through continuous time was tracked to show the 3Hz anomaly caused by beats. The result measured at surface was compared with that measured in the borehole to verify whether beats generated change in low frequency range (~3Hz) are present at both surface and borehole.

Set Header

The first work that was done on the data was to set header for each file so that Geopsy could distinguish components and file names. This was done using the following equations:

Set Components (surface data):

```
if(left(right(FileName,6),1)=="z", Component="Vertical");

if(left(right(FileName,6),1)=="n", Component="North");

if(left(right(FileName,6),1)=="e", Component="East");
```

Set file name (surface data):

```
Name= left(right(FileName,15),3;
```

Set Components (borehole data):

```
if(left(right(FileName,6),0)=="z", Component="Vertical");
if(left(right(FileName,6),1)=="n", Component="North");
if(left(right(FileName,6),2)=="e", Component="East");
```

Set File Name (borehole data):

```
Name= left(right(FileName,10),3;
```

Raw Beat Test Record

The raw beat test data recorded at surface was used to determine the time interval of clean data before beats since strong perturbations including driving noise, surface traffic or other artifacts can be easily detected at surface records. To obtain a clean signal all the time intervals with obvious strong artificial interferences were cut out. This is an important step in the workflow. However, it is the first interpretive, nonautomatic routine in the data processing. Figure 28 shows a representative record of the wavefield before and after beats in the survey area. The record shows data from 20:00 to 21:00 recorded at surface station 301 which located very close to the wellhead. The recording time 20:00-21:00 refers to the local time 15:00-16:00 of 5 February 2011. The beats took place between 20:38 and 20:42 and noise caused by machine driving around occurred between 20:32 and 20:36. The three traces correspond to the vertical, east/west, and north/south component. The clean data was determined from amplitude spectrum analysis using a time window of 60s long, and it turned out that clean data could be 20:10 to 20:11 before beats and 20:43 to 20:44 after beats (green window). Figure 29 shows data recorded in the borehole from the same quiet time 20:10 to 20:11 and 20:43 to

20:44 recorded by sensor 5. Again, three traces correspond to the vertical, east/west, and north/south component. In the raw borehole data the dominant noises were high amplitude pulses of unknown source that occurred systematically at about every 4s before beats and every 10s after beats.

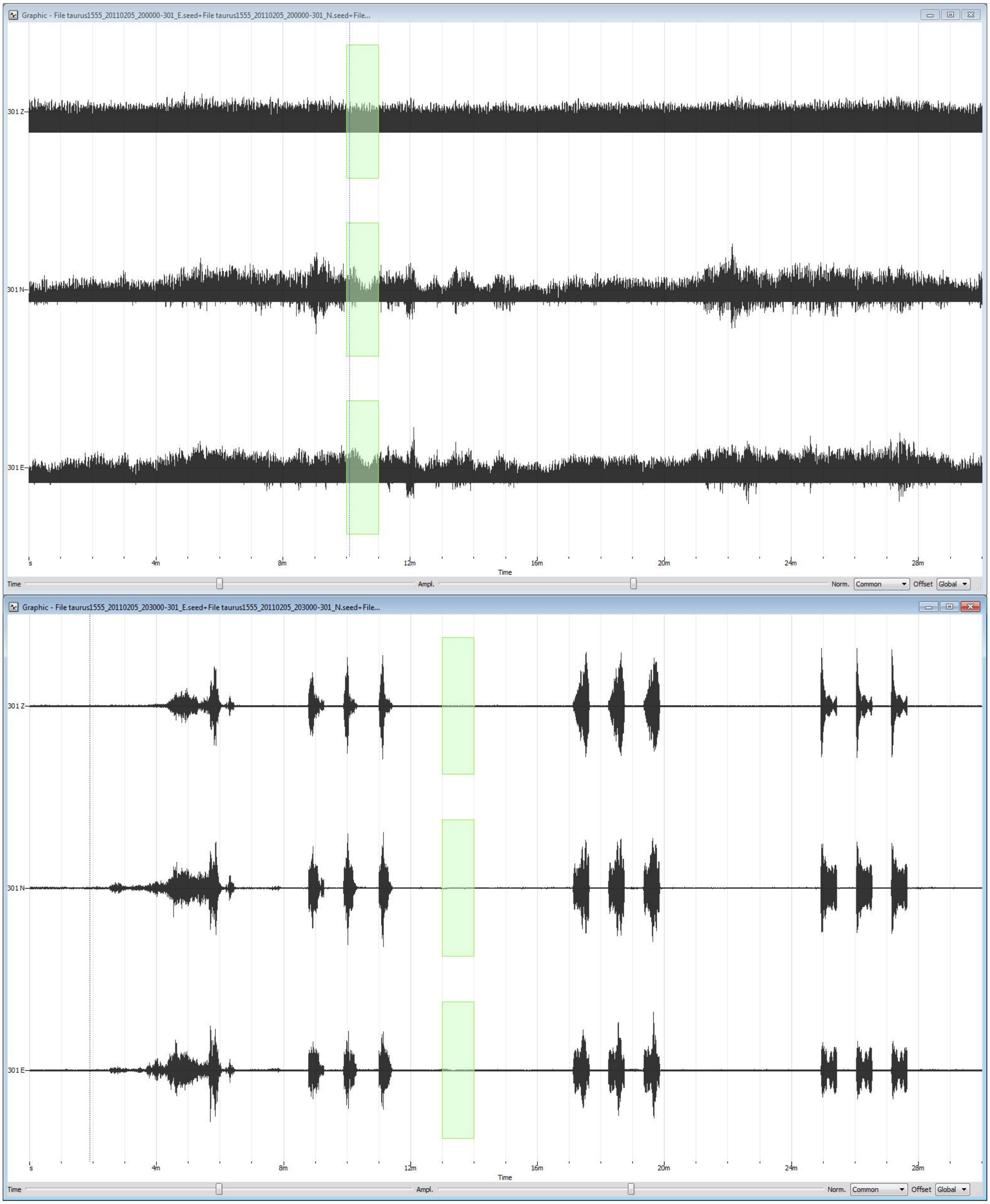

Figure 28: Raw beat data from surface station 301. Three traces are vertical, north-south, and east-west component respectively. Upper: Data from 20:00 to 20:30. Lower: Data from 20:30 to 21:00. Beats occurred from 20:38 to 20:42. Listening time was 5min from 20:42 to 20:47.

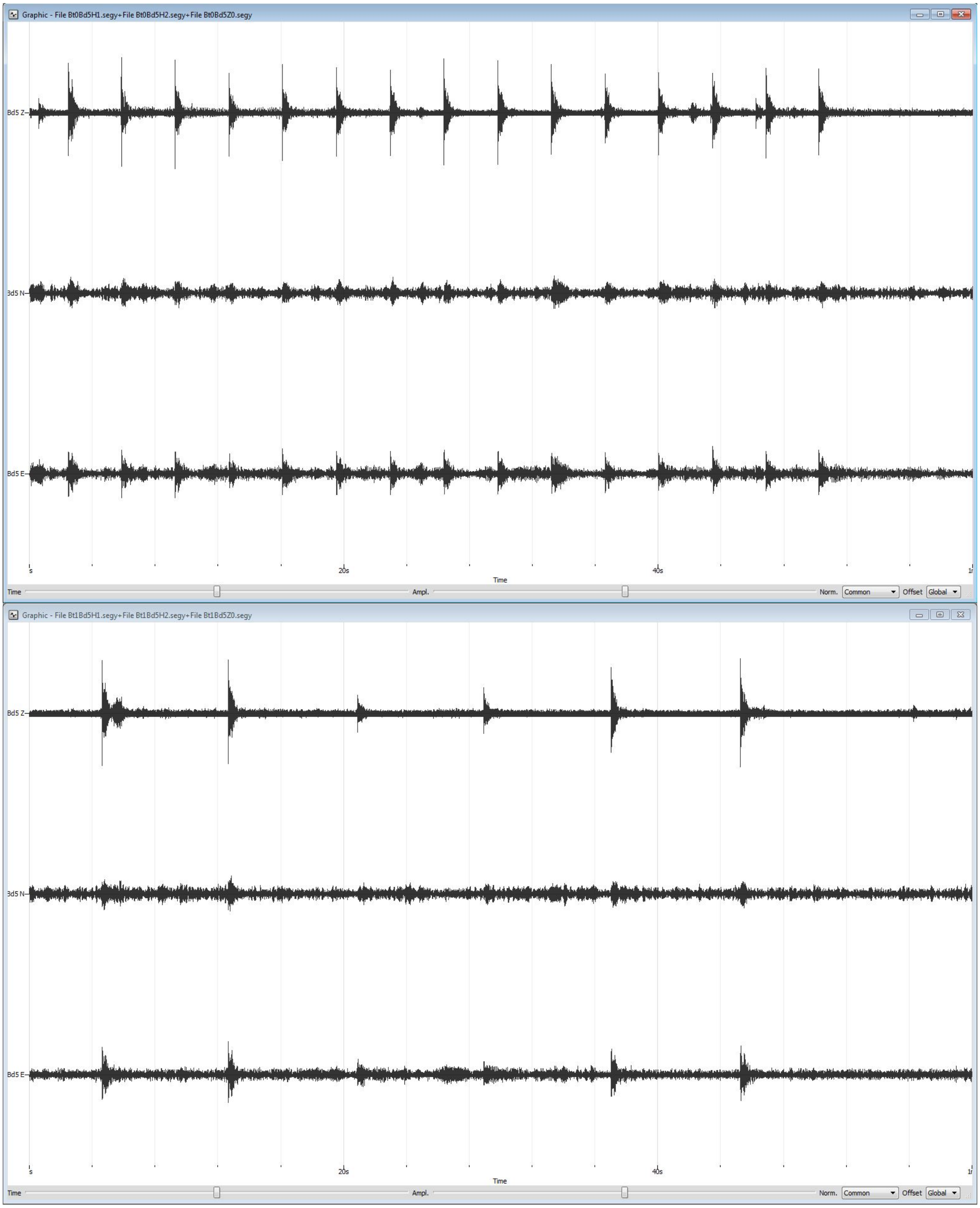

Figure 29: Raw beat data from borehole sensor 5. Three traces are vertical, north-south, and east-west component respectively. Upper: Data before beats, from 20:10 to 20:11. Lower: Data after beats, from 20:43 to 20:44.

Amplitude Spectrum

The data with header set successfully was processed with Spectrum Analysis processor in Geopsy. Parameters of a time window of 60s in length and a frequency range of 1-15Hz were used to calculate amplitude spectrum. The 60s was used since data size limitation in Geopsy showed the proper borehole data to be one minute long. Figure 30 shows a toolbox of all the parameters needed for windowing, processing, graphic appearance, and output destination.

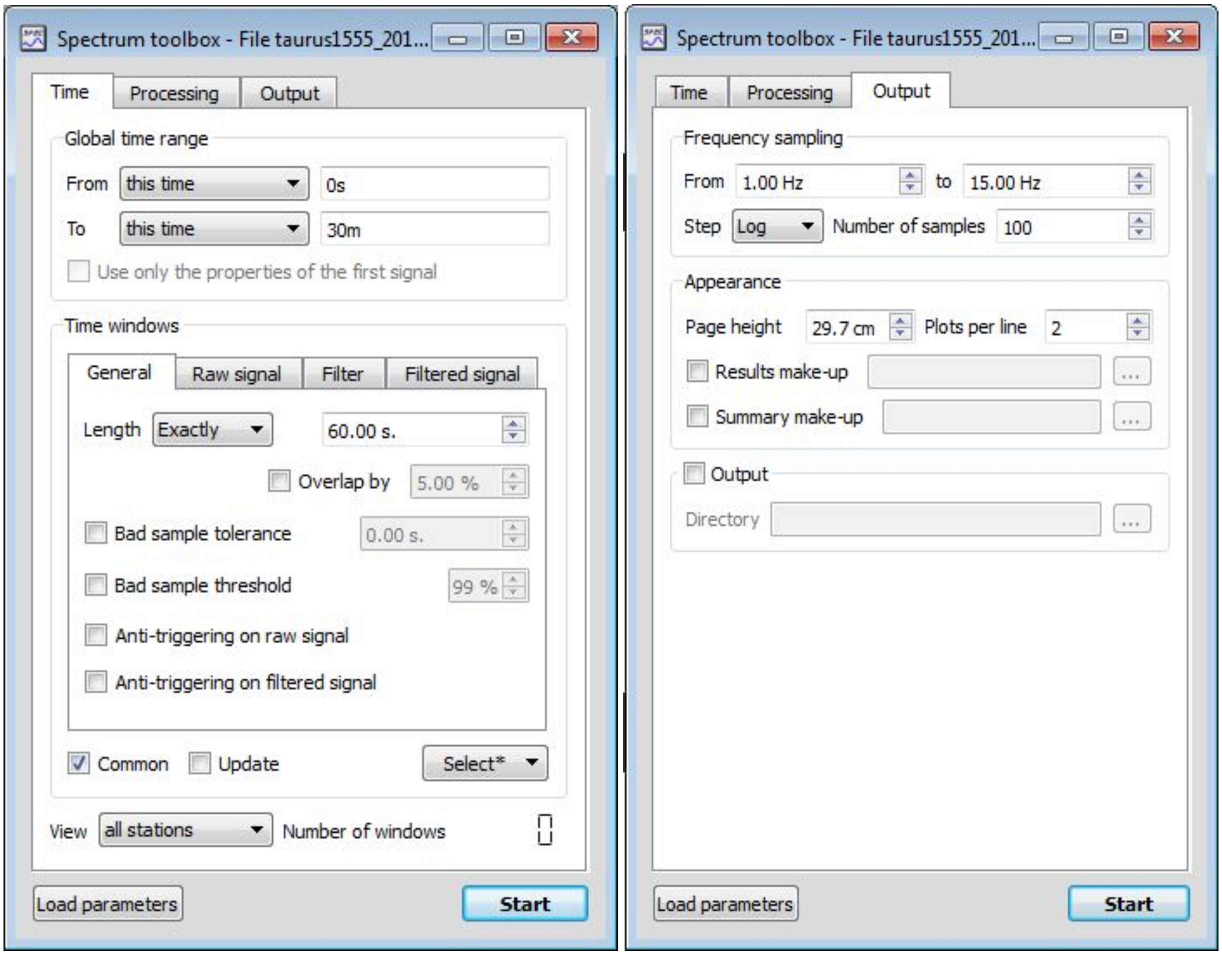

From: this time 0s

To: this time 30m

☐ Use only the properties of the first signal

Length: Exactly 60.00 s.

☐ Overlap by 5.00 %

☐ Bad sample tolerance 0.00 s.

☐ Bad sample threshold 99 %

☐ Anti-triggering on raw signal

☐ Anti-triggering on filtered signal

☑ Common ☐ Update

View: all stations Number of windows: 0

From 1.00 Hz to 15.00 Hz

Step: Log Number of samples: 100

Page height: 29.7 cm Plots per line: 2

☐ Results make-up

☐ Summary make-up

☐ Output

Directory

Figure 30: Time window length and frequency content used for spectrum analysis.

Surface Records

Figure 31 shows spectrum of the data recorded at surface station 301 at a quiet time before beats from 20:10 to 20:11 and the data at a quiet time after beats from 20:43 to 20:44. One feature showed up in the ambient wavefield before beats was a narrow band signals at 8Hz that appeared dominantly on horizontal components. This feature could be possibly love wave which propagates horizontally or shear wave that propagates from subsurface. Since this recording time was 15:00-16:00 at the local time when the ambient noise could be high, this 8Hz was very likely related to artificial noise such as industrial machinery or traffic. This 8Hz feature was also present at other surface records at the same time interval shown in Figure 32. 301 through 316 correspond to surface stations from near wellhead to far wellhead covering 3miles of the survey area. Before beats were done most surface stations showed quiet amplitude on all components especially in the range of 1-6Hz, and a constant 8Hz feature that presented dominantly on two horizontal components and a little bit on the vertical with varied amplitudes among different stations.

After beats were done station 301 showed a feature of amplitude increase at 3Hz which was absent before beats and attenuation of the feature at 8Hz meanwhile (Figure 33). The 3Hz feature was dominantly on vertical and also presented on two horizontals, namely, a P-wave. This feature presented at other surface stations as well shown in Figure 38. All surface stations presented a turning on of 3Hz and turning off at 8Hz with unknown reasons after beats. Most interesting for this study are the features between 1-6Hz since it lies between the ocean wave peak and the anthropogenic noise band and is most probably produced by natural sources and/or geological conditions. Therefore, the feature at 8Hz will not be discussed too much in this research.

Figure 34 shows a track of spectrum variation at 3Hz through continuous time, from 20:33 to 20:47, including 5min time before beats, 3min beats time and 5min listening time after beats done. The data recorded from station 301 was used since it was right above the reservoir and also the most nearest station to the wellhead. The plots were displayed upon time with each plot corresponds to a one minute data. Before beats (20:33-20:38) two typical features that were shown at surface were a weak amplitude peak at 1Hz and a high amplitude peak at 8Hz. Both two features were recognized as transients since they varied with time. At 3Hz there was almost none amplitude anomaly before beats. During beats time (20:39-20:42) three separate beats were conducted with each lasted for 30ms, and none anomaly was measured in the range of 1-8Hz while extreme high amplitude at/after 10Hz was examined. Beats stopped at 20:42 and listening time was 5min from 20:42 to 20:47, during which time the measurements showed continuously anomaly at 3Hz with enhanced amplitude on all components and large attenuation at 8Hz with varied amplitudes. All these analyses show that 3Hz anomaly caused by beats could be the body wave related to the hydrocarbon reservoir in below.

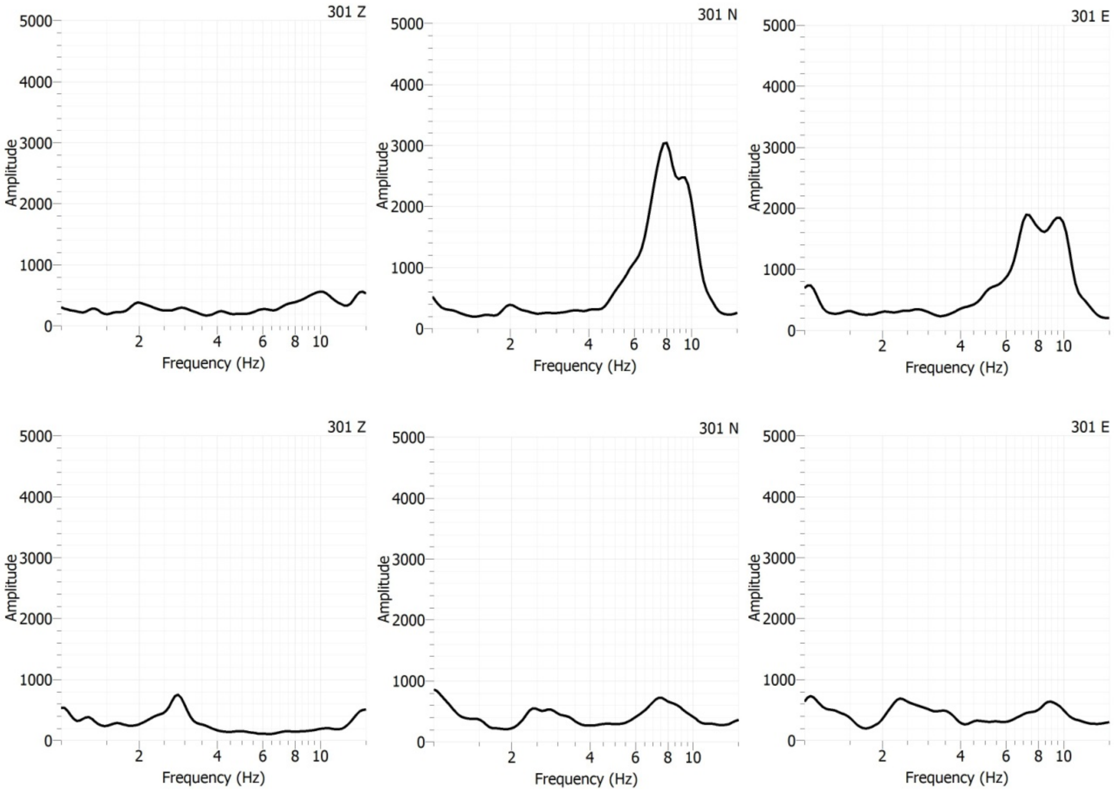

Figure 31: Spectrum of 3C data at surface from a near wellhead station 301. Upper: Data at a quiet time before beats 20:10-20:11. Lower: Data at a quiet time after beats 20:43-20:44.

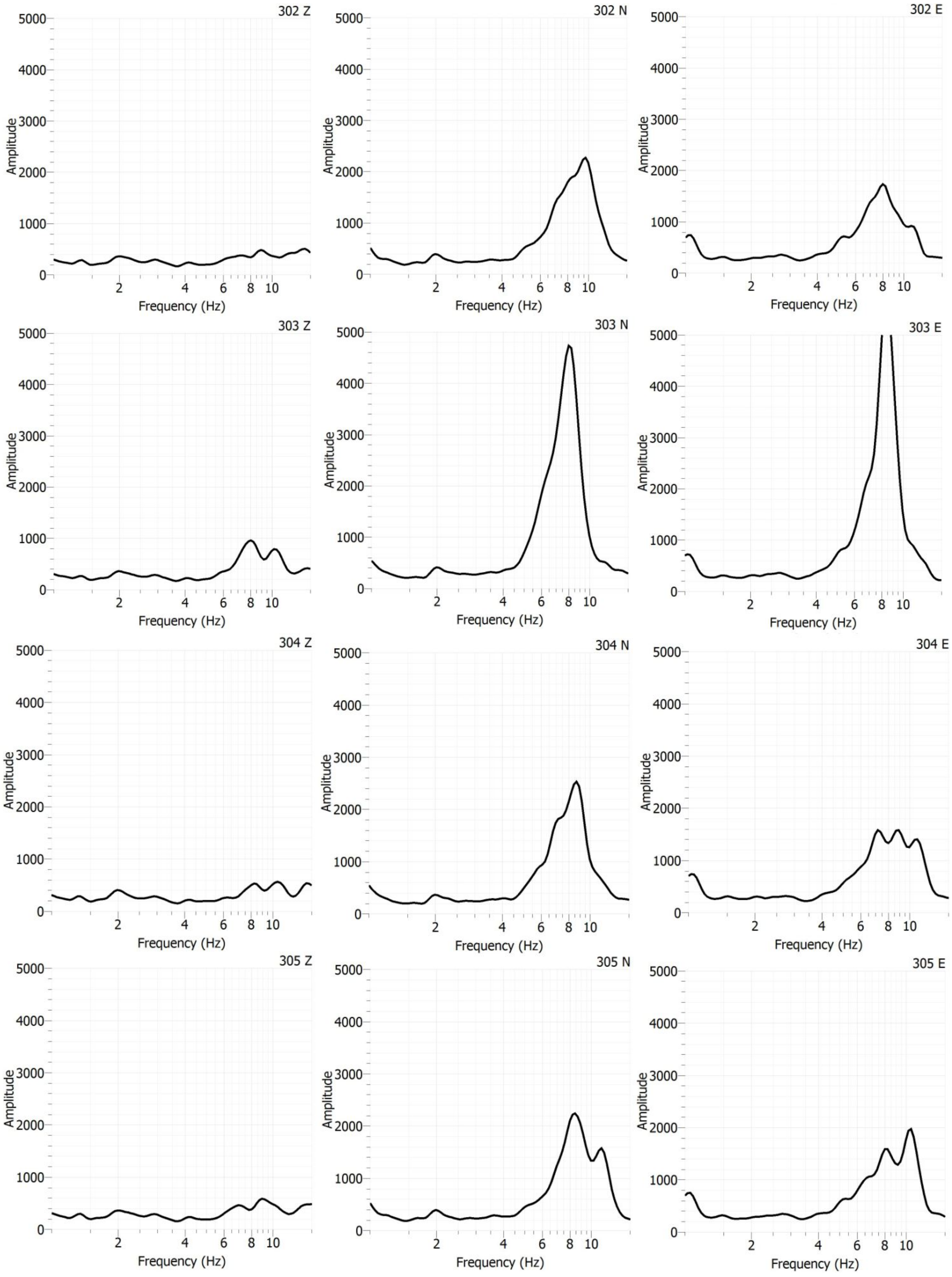

Figure 32: Spectrum of 3C data at all surface stations from 301 through 316. Data was recorded at a quiet time from 20:10-20:11 before beats. The ambient wavefield has quiet amplitudes between 1-6Hz and high amplitudes at 8Hz dominantly on horizontal components. (contituted on next page)

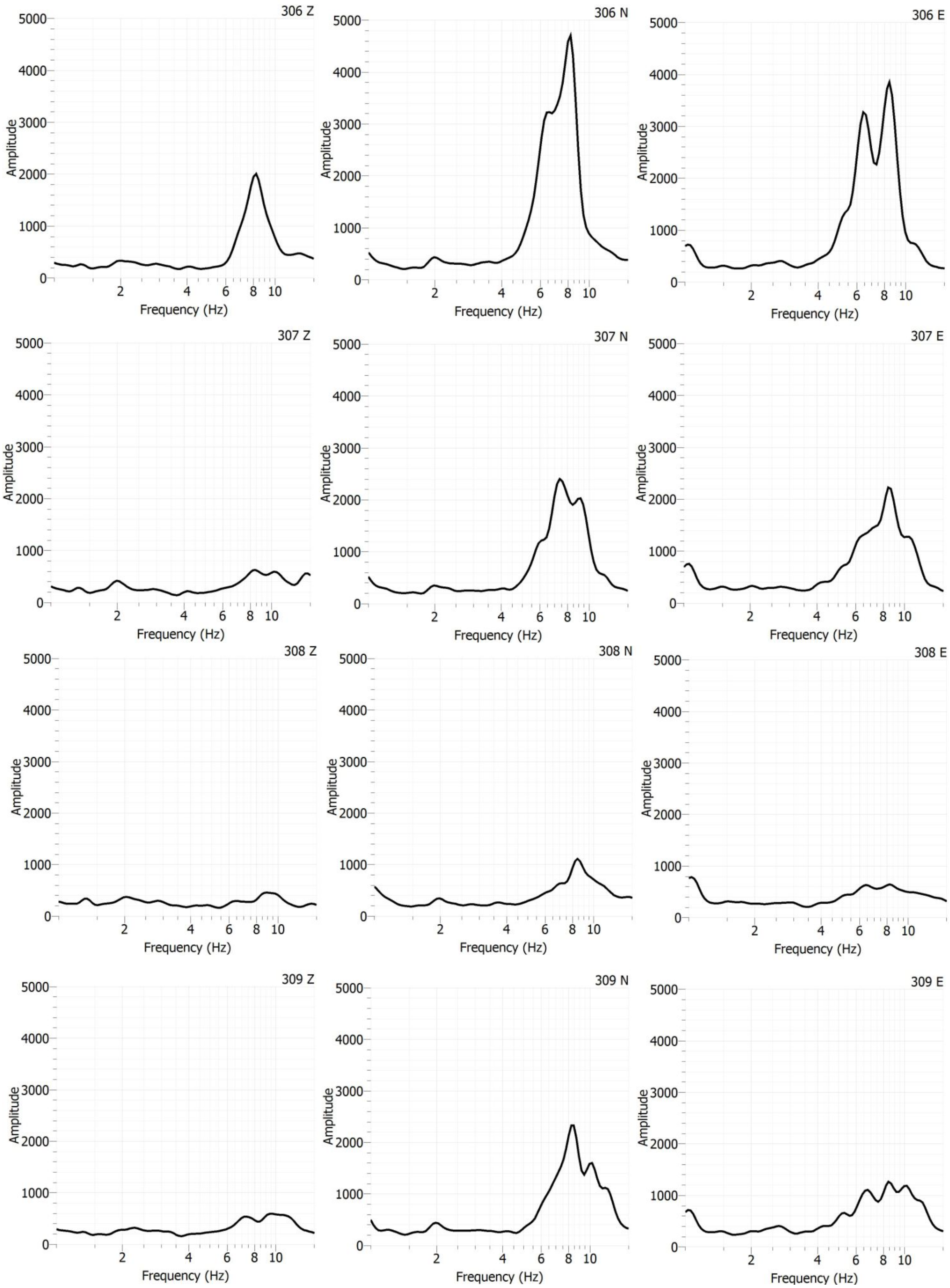

Figure 32: (Continued) Spectrum of 3C data at all surface stations from 301 through 316. Data was recorded at a quiet time from 20:10-20:11 before beats. The ambient wavefield has quiet amplitudes between 1-6Hz and high amplitudes at 8Hz dominantly on horizontal components. (continuted on next page)

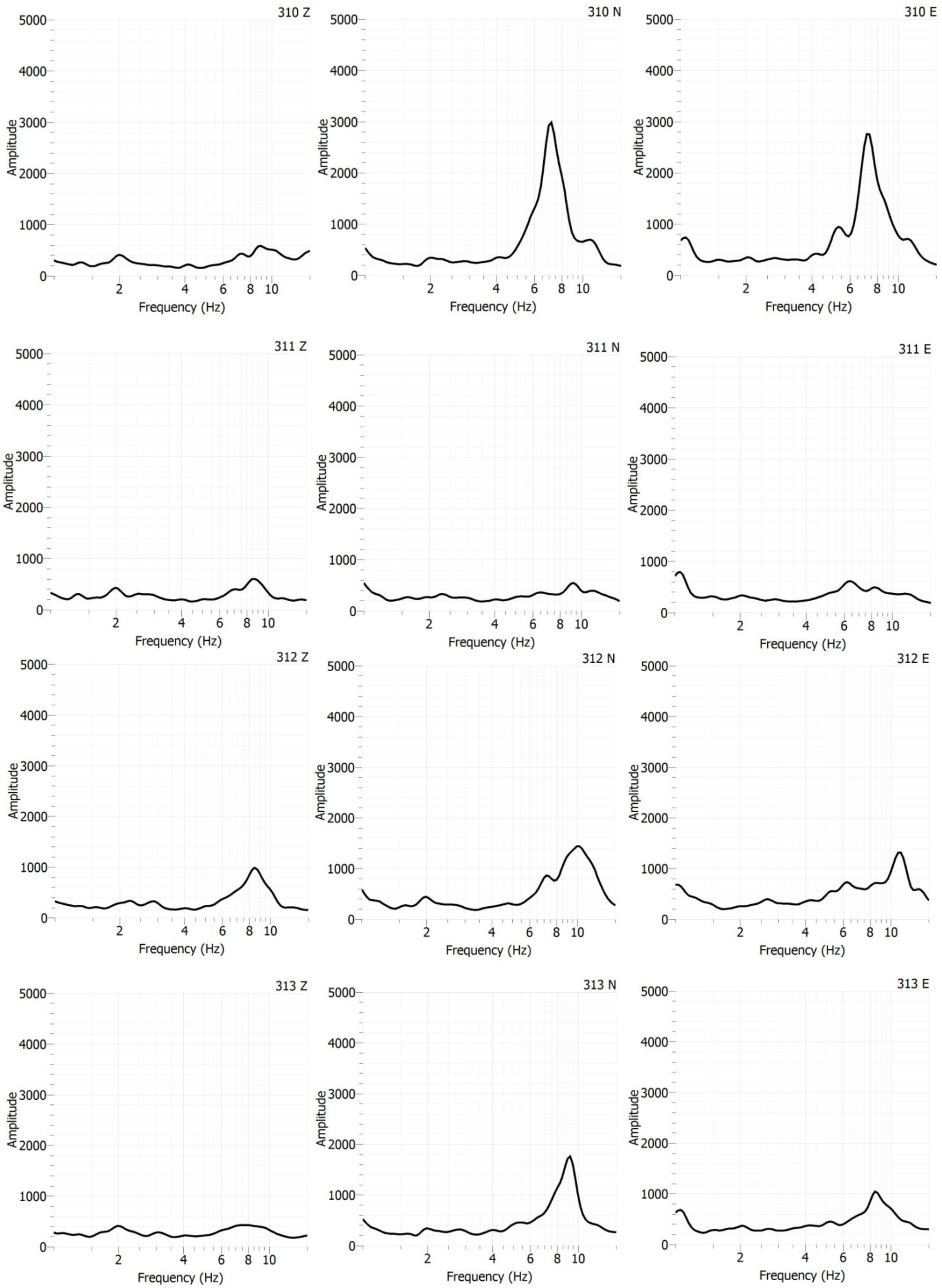

Figure 32: (Continued) Spectrum of 3C data at all surface stations from 301 through 316. Data was recorded at a quiet time from 20:10-20:11 before beats. The ambient wavefield has quiet amplitudes between 1-6Hz and high amplitudes at 8Hz dominantly on horizontal components. (continuted on next page)

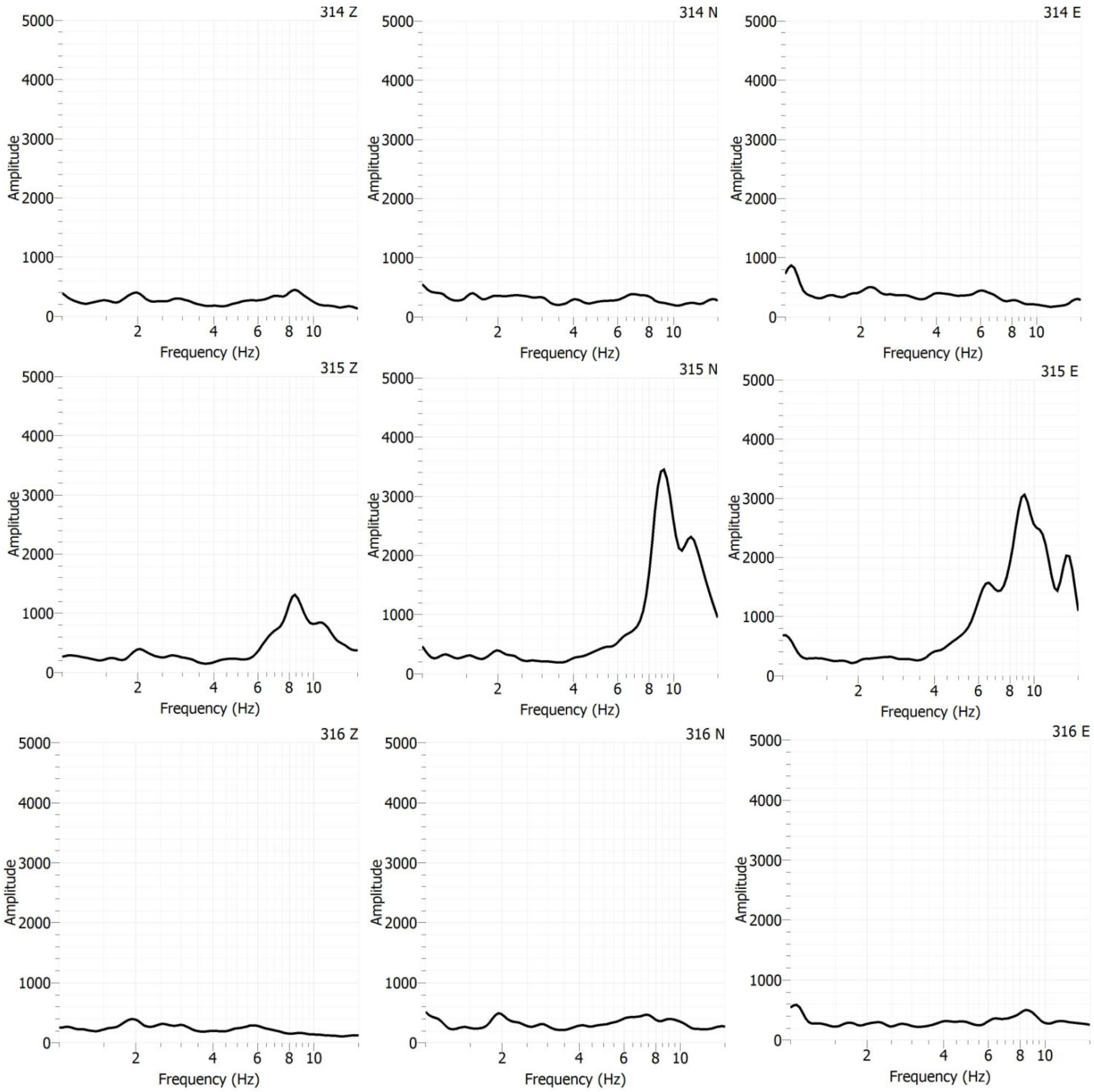

Figure 32: (Continued) Spectrum of 3C data at all surface stations from 301 through 316. Data was recorded at a quiet time from 20:10-20:11 before beats. The ambient wavefield has quiet amplitudes between 1-6Hz and high amplitudes at 8Hz dominantly on horizontal components.

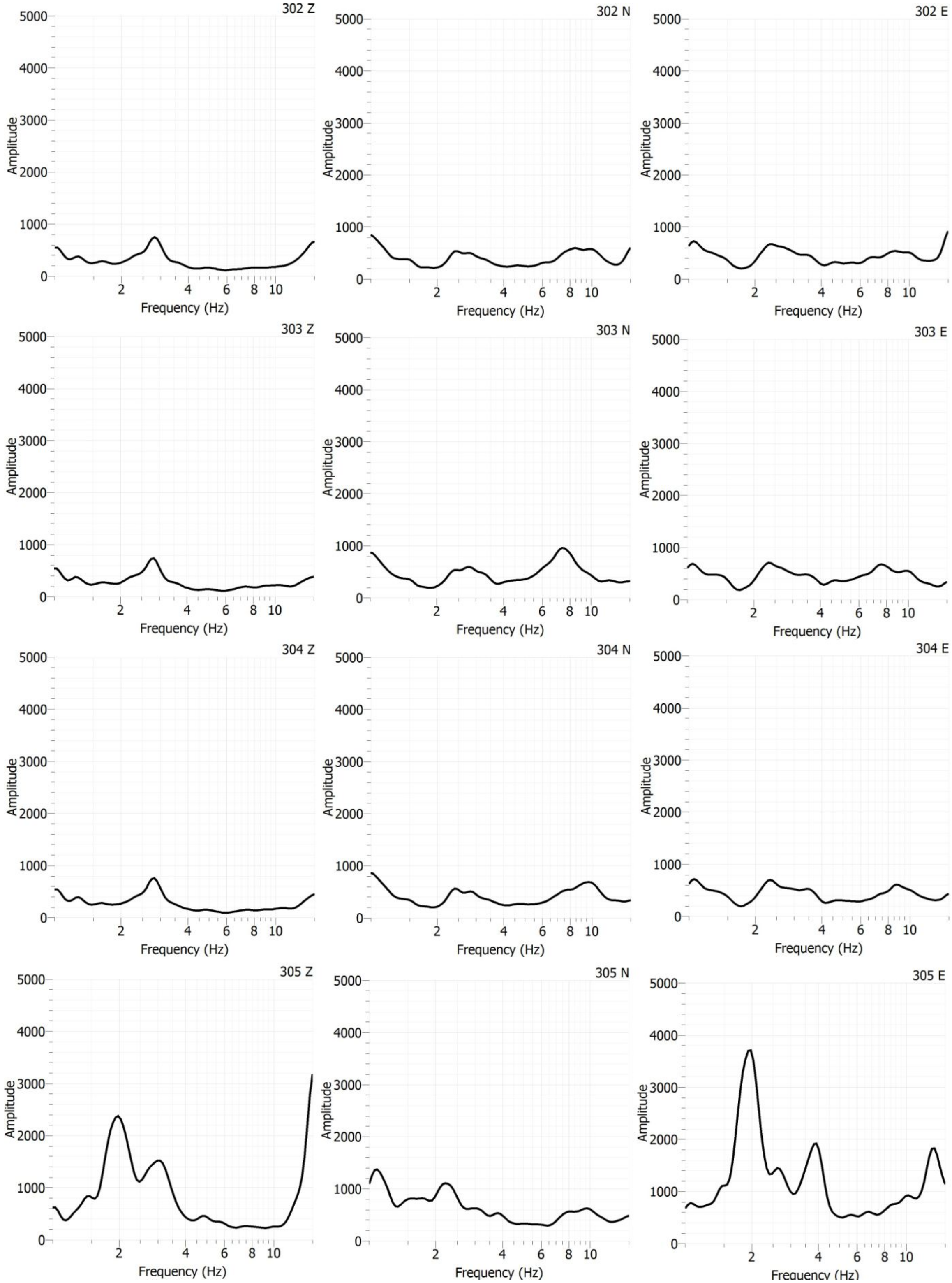

Figure 33: Spectrum of 3C data at all surface stations from 301 through 316. Data was recorded at a quiet time from 20:43-20:44 after beats. All stations showed enhanced amplitudes at 3Hz on three components and decreased amplitudes at 8Hz after beats. (continued on next page)

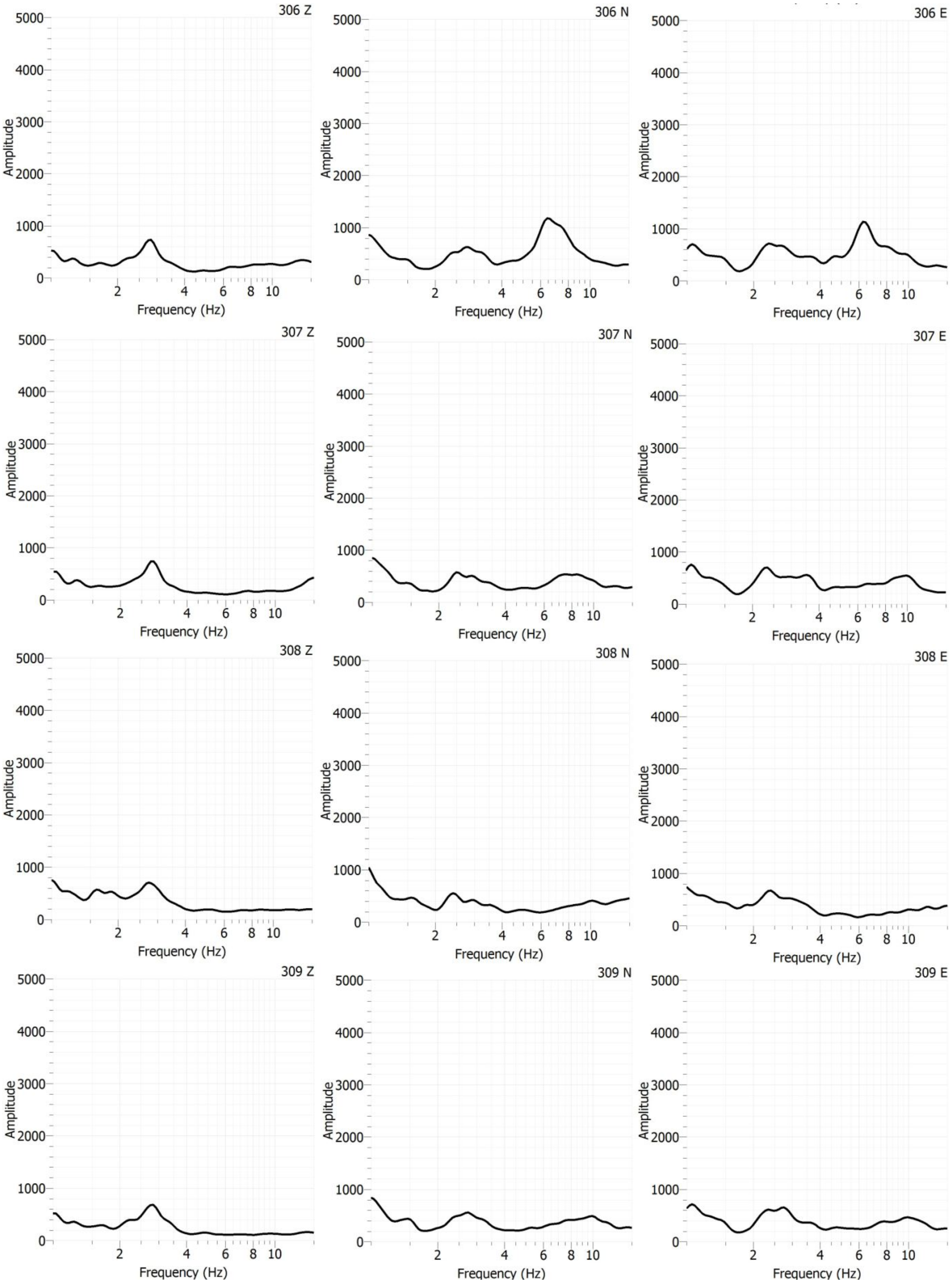

Figure 33: (Continued) Spectrum of 3C data at all surface stations from 301 through 316. Data was recorded at a quiet time from 20:43-20:44 after beats. All stations showed enhanced amplitudes at 3Hz on three components and decreased amplitudes at 8Hz after beats. (continued on next page)

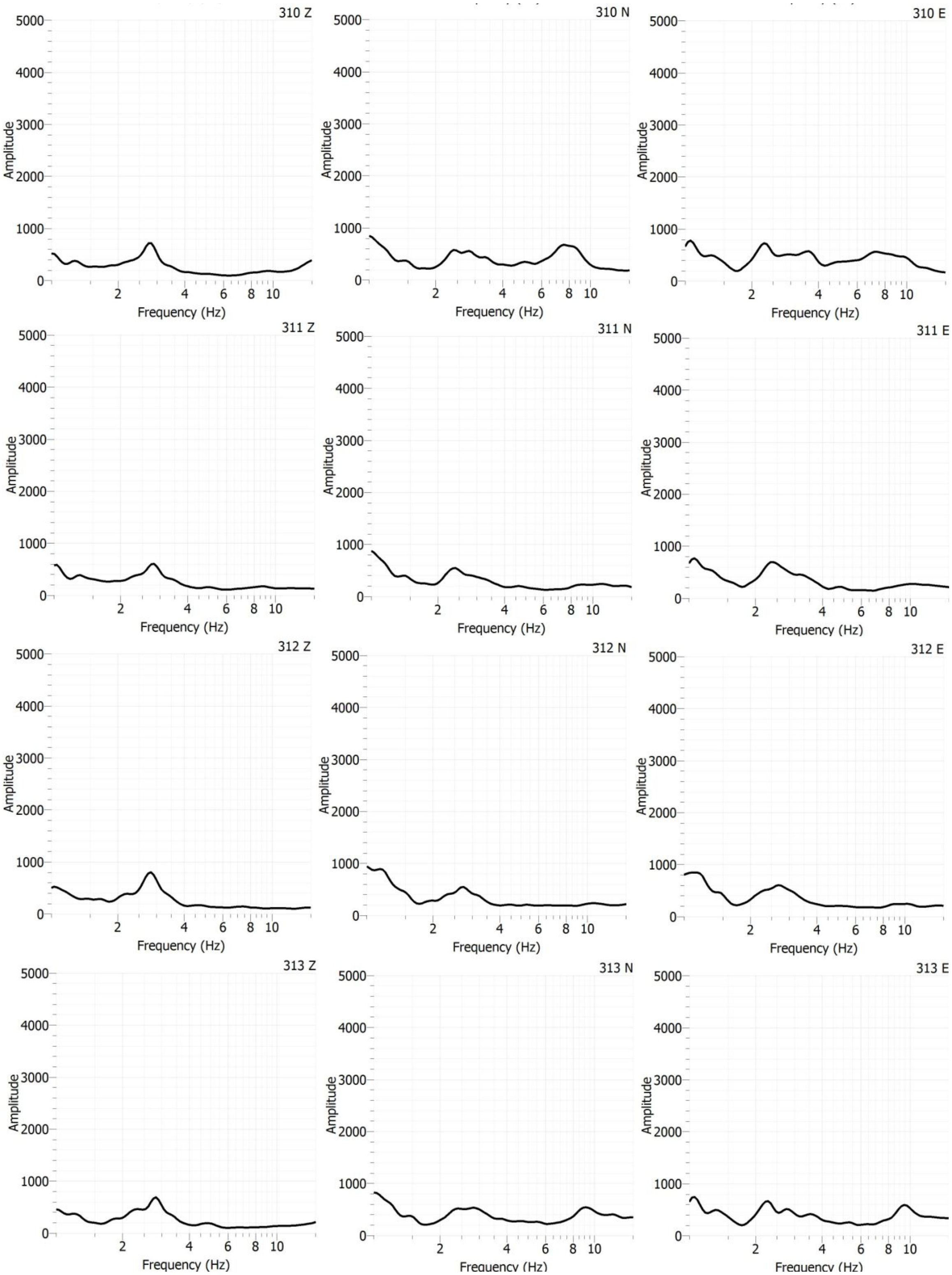

Figure 33: (Continued) Spectrum of 3C data at all surface stations from 301 through 316. Data was recorded at a quiet time from 20:43-20:44 after beats. All stations showed enhanced amplitudes at 3Hz on three components and decreased amplitudes at 8Hz after beats. (continued on next page)

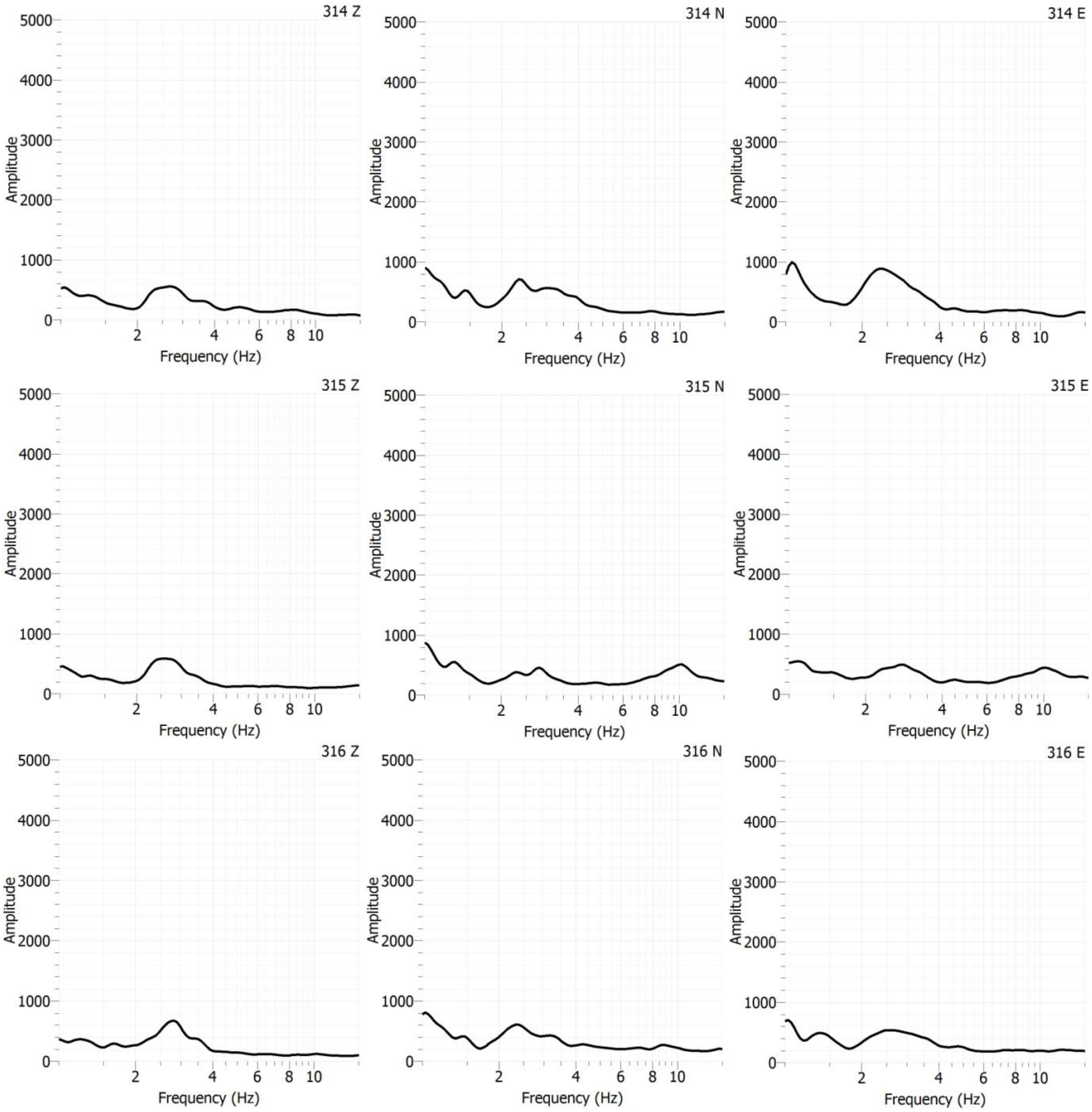

Figure 33: (Continued) Spectrum of 3C data at all surface stations from 301 through 316. Data was recorded at a quiet time from 20:43-20:44 after beats. All stations showed enhanced amplitudes at 3Hz on three components and decreased amplitudes at 8Hz after beats.

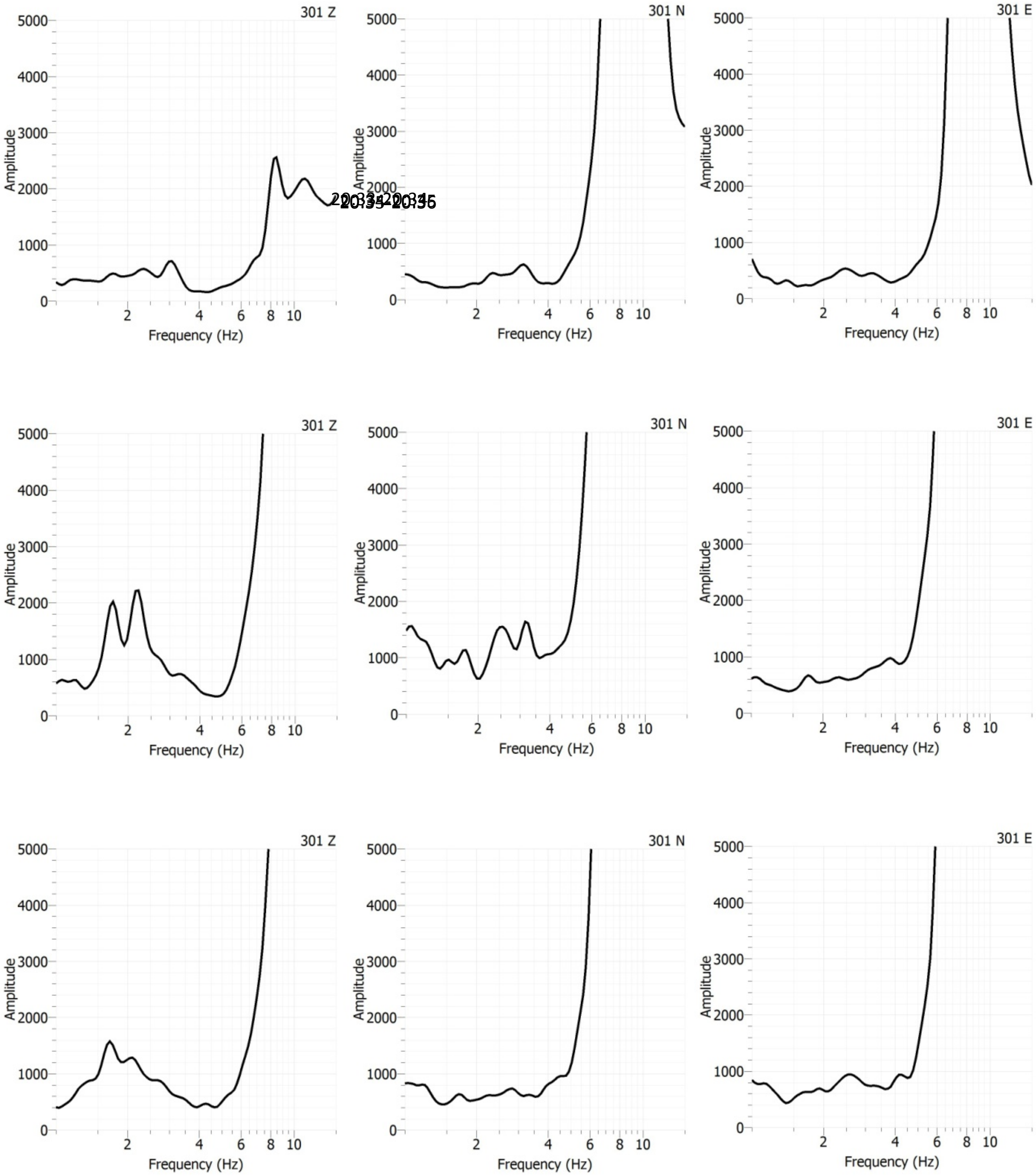

Figure 34: Track of spectrum variation at 3Hz from 20:33 to 20:47 at surface station 301. Beats occurred from 20:38 to 20:42. (continued on next page)

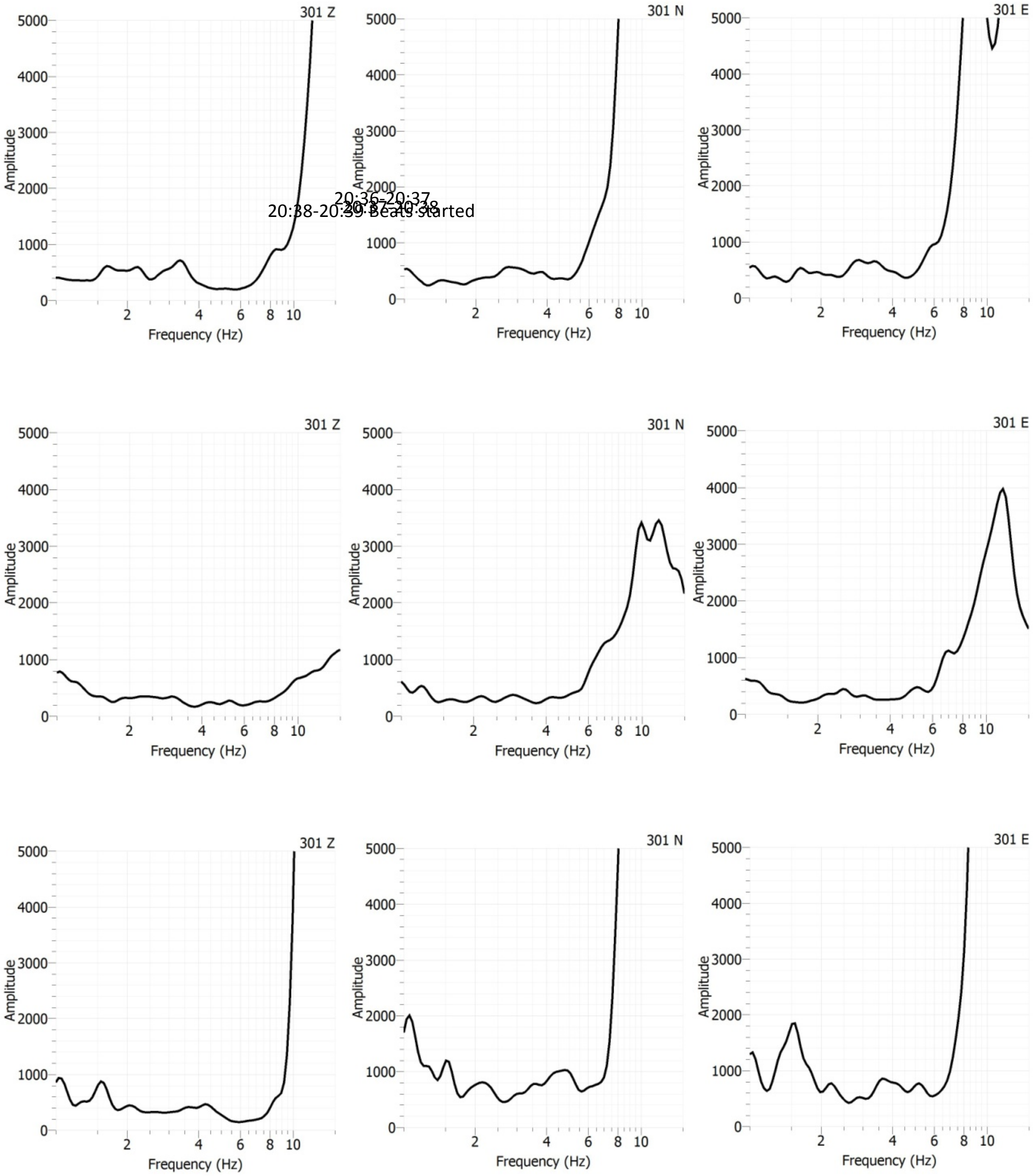

Figure 34: (Continued) Track of spectrum variation at 3Hz from 20:33 to 20:47 at surface station 301. Beats occurred from 20:38 to 20:42. (continued on next page)

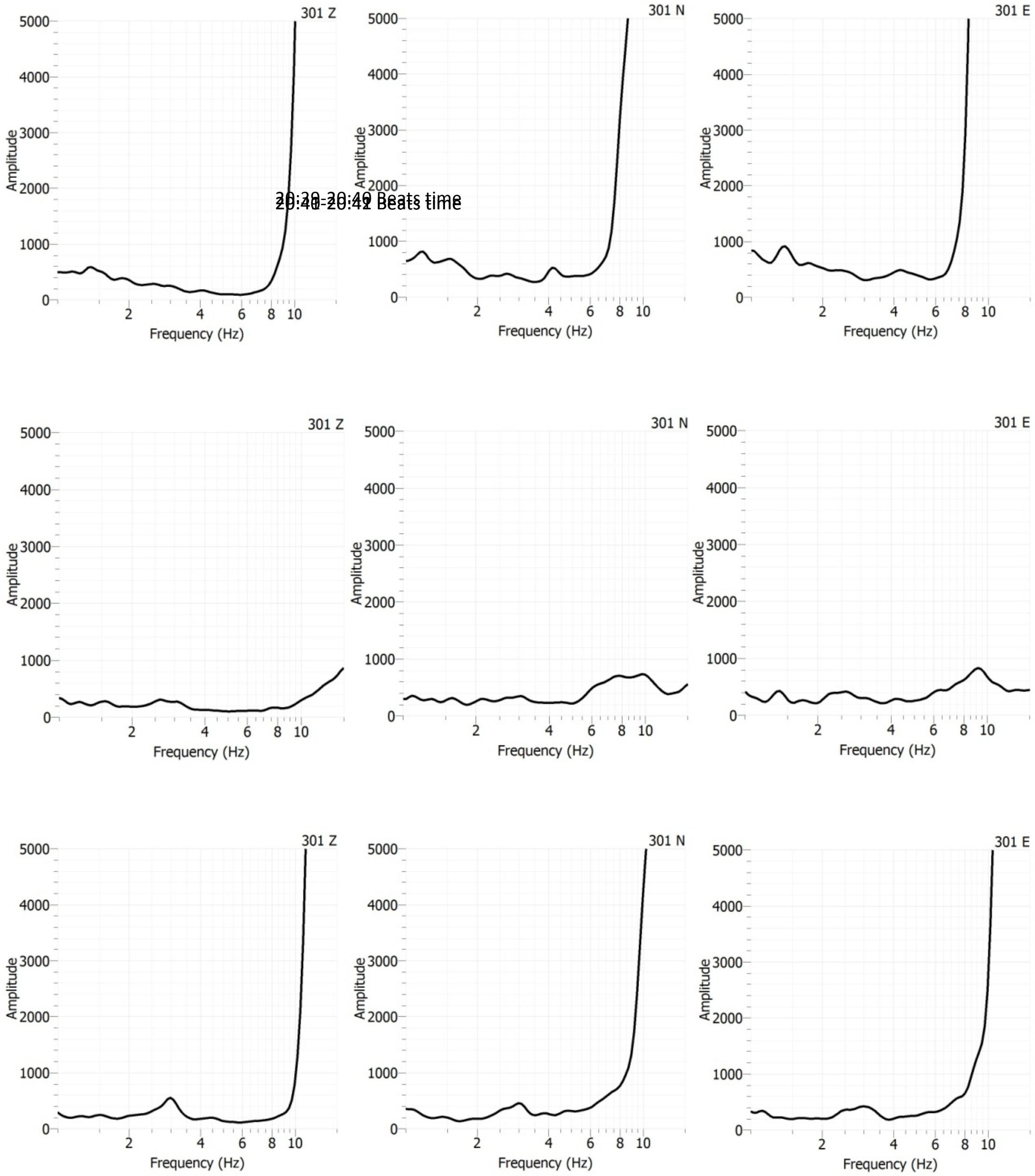

Figure 34: (Continued) Track of spectrum variation at 3Hz from 20:33 to 20:47 at surface station 301. Beats occurred from 20:38 to 20:42. (continued on next page)

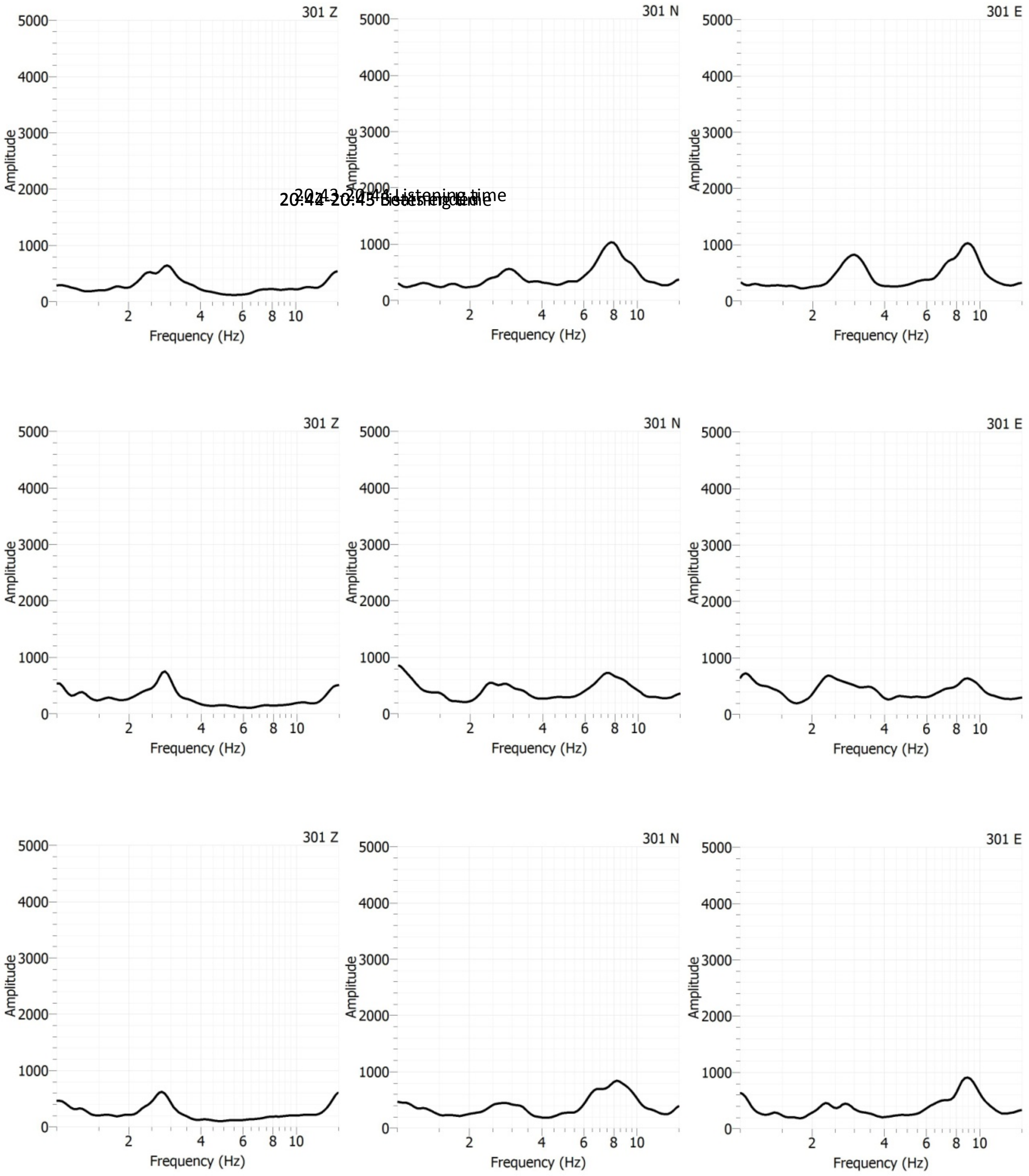

Figure 34: (Continued) Track of spectrum variation at 3Hz from 20:33 to 20:47 at surface station 301. Beats occurred from 20:38 to 20:42. (continued on next page)

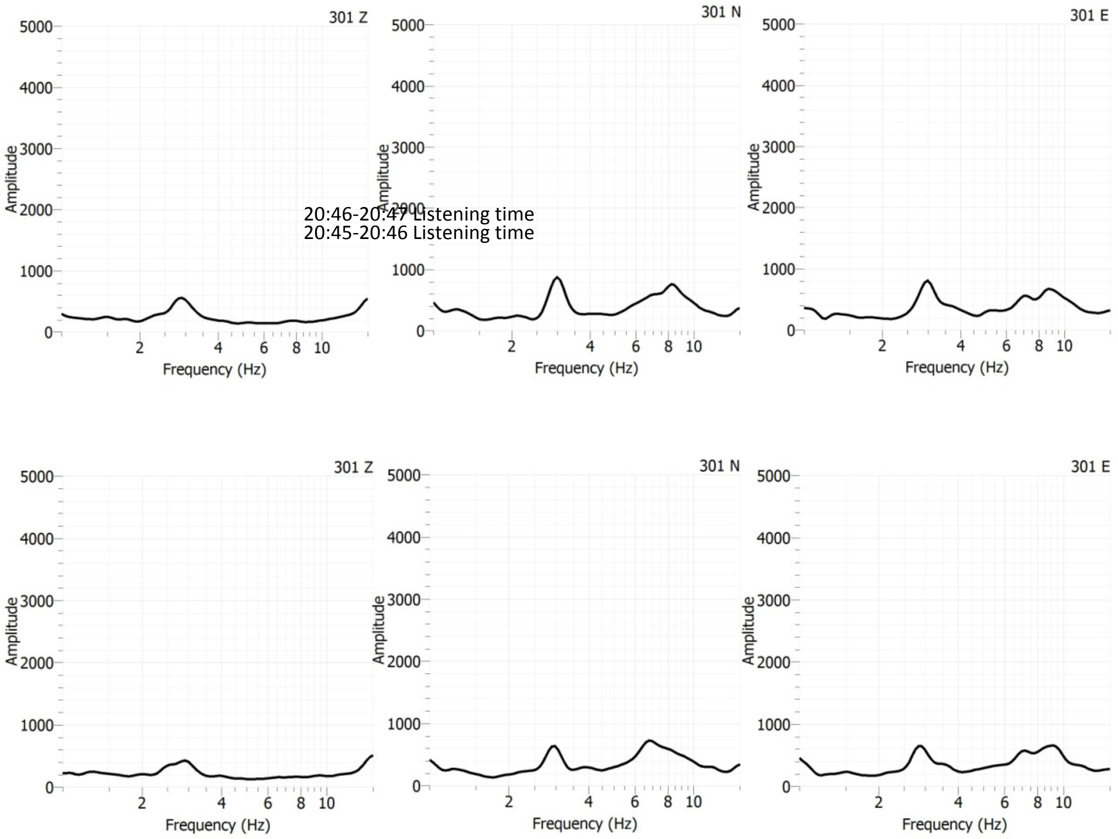

Figure 34: (Continued) Track of spectrum variation at 3Hz from 20:33 to 20:47 at surface station 301. Beats occurred from 20:38 to 20:42.

Borehole Records

Figure 35 shows spectrum of the data recorded in the borehole from sensor 5 at the same quiet time before beats from 20:10 to 20:11 and the data at the same quiet time after beats from 20:43 to 20:44. The borehole data was recorded with ultrasensitive sensor that has a dominant frequency of 4.5Hz such that the records showed a roll-off of waves below 4.5Hz. Another feature showed up in the ambient wavefield measured from borehole was a narrow band signals at 8Hz as that measured at surface, however, the difference being that 8Hz feature in the borehole was dominantly on vertical component. This 8Hz feature was also present at other borehole measurements shown in Figure 36. Record from initial top sensor Bd1 was omitted due to poor measurement, leaving only 6 borehole sensors that were Bd3 through Bd8 from top to bottom covering an array of 70m in length. Before beats were done most borehole measurements showed roll-off below 4.5Hz on all three components caused by the sensors and a constant feature at 8Hz presented on all three components with amplitudes decreased with depth. In the range of 1-6Hz, one can see a small peak at 3Hz but very weak to none due to 4.5Hz roll-off. After beats were done borehole records showed largely enhanced amplitude at 3Hz on all three components as well as large amplitude attenuation at 8Hz as that measured at surface. Since the hydrocarbon-related energy anomaly is usually stronger in the vertical component compared to the horizontal components, the 3Hz feature was very likely to be relevant to hydrocarbon reservoir. This feature also presented in other borehole records shown in Figure 37. All borehole records presented amplitude turning on at 3Hz and turning off at 8Hz after beats. Again, focus will be put on the 1-6Hz range and the turning off at 8Hz will not be discussed too much in this research.

Figure 38 shows a track of spectrum variation at 3Hz through time in the borehole measurements. The track was done on the records from sensor 5 which was the middle sensor in the array. The track time was from 20:33 to 20:47, the same as that in the surface data analysis. Each plot corresponds to a one minute data and all the plots were displayed upon time. Before beats (20:33-20:38) typical features shown in the borehole measurements were: a roll-off below 4.5Hz caused by borehole sensors, three amplitude peaks that occurred at 3Hz, 4.5Hz and 8Hz respectively on all components with 3Hz dominant on vertical and 8Hz dominant on horizontals at most times, and highest amplitudes occurred at 8Hz. During beats time (20:39-20:42) roll-off below 4.5Hz was still evident while the three peaks at 3Hz, 4.5Hz, and 8Hz decreased in amplitudes. After beats (20:42-20:47) the amplitudes at 3Hz increased a lot making the roll-off effects barely noticeable. The amplitude at 3Hz was highest on the vertical component and also the highest compared to the 4.5Hz and 8Hz even under the roll-off effects. The presence of the 3Hz feature continued during the whole 5min listening time.

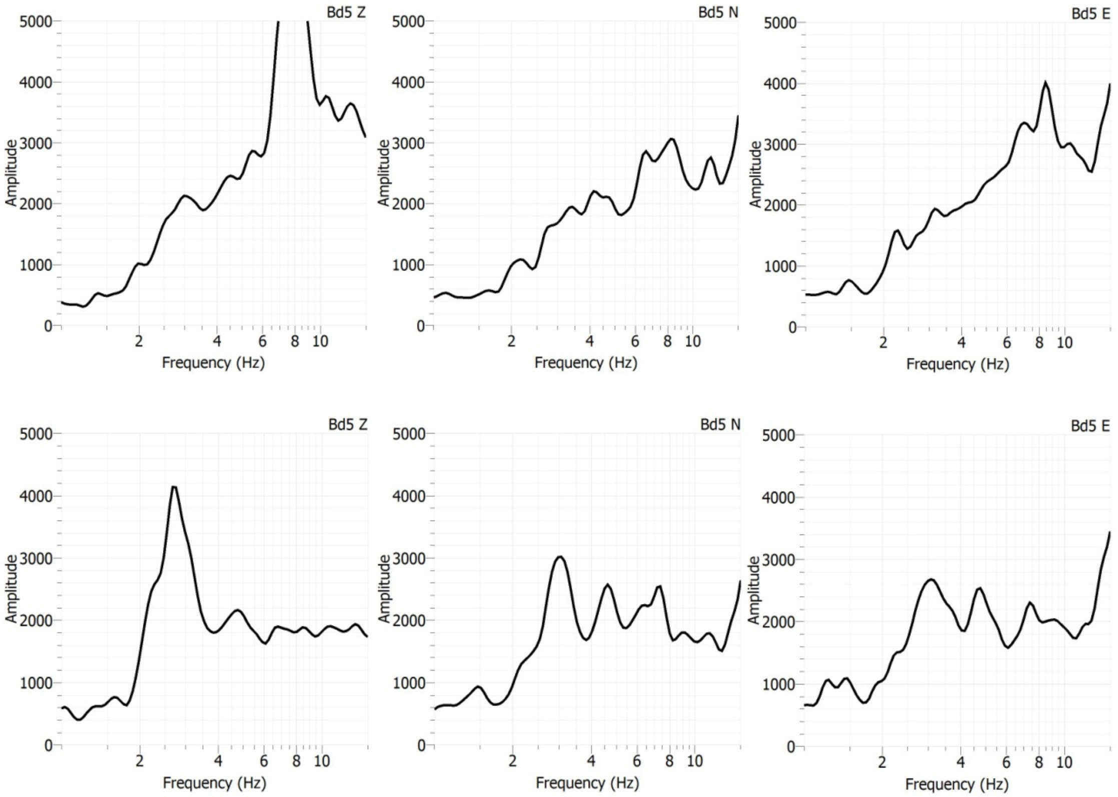

Figure 35: Spectrum of 3C data in the borehole from sensor 5. Upper: Data at a quiet time before beats 20:10-20:11. Lower: Data at a quiet time after beats 20:43-20:44.

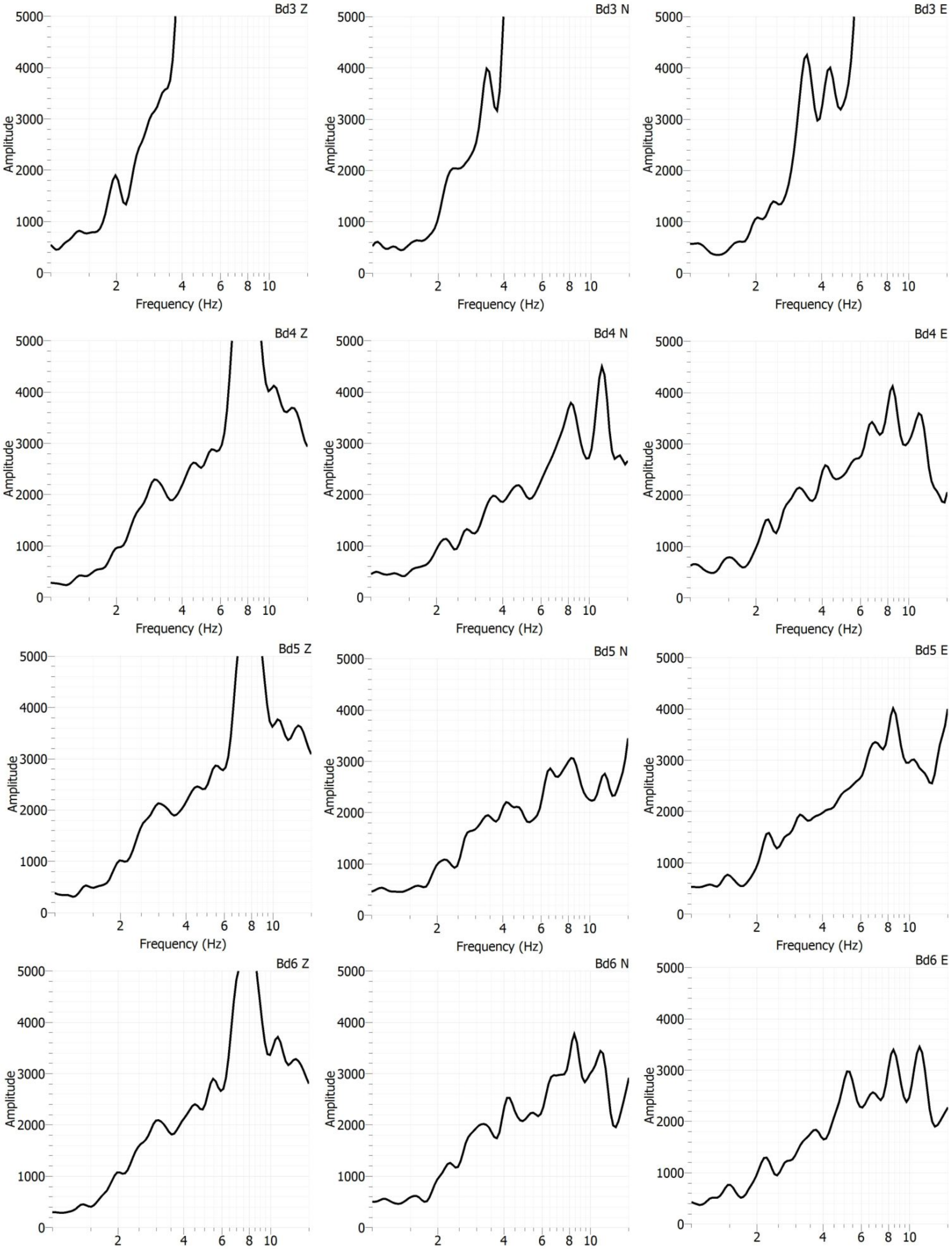

Figure 36: Spectrum of 3C data measured in the borehole with records displayed upon depth, i.e. Bd3 through Bd8 correspond to top sensor through bottom sensor. Data was at a quiet time from 20:10-20:11 before beats. All borehole sensors showed roll-off below 4.5Hz casued by sensors and a feature of high amplitude at 8Hz. (continued on next page)

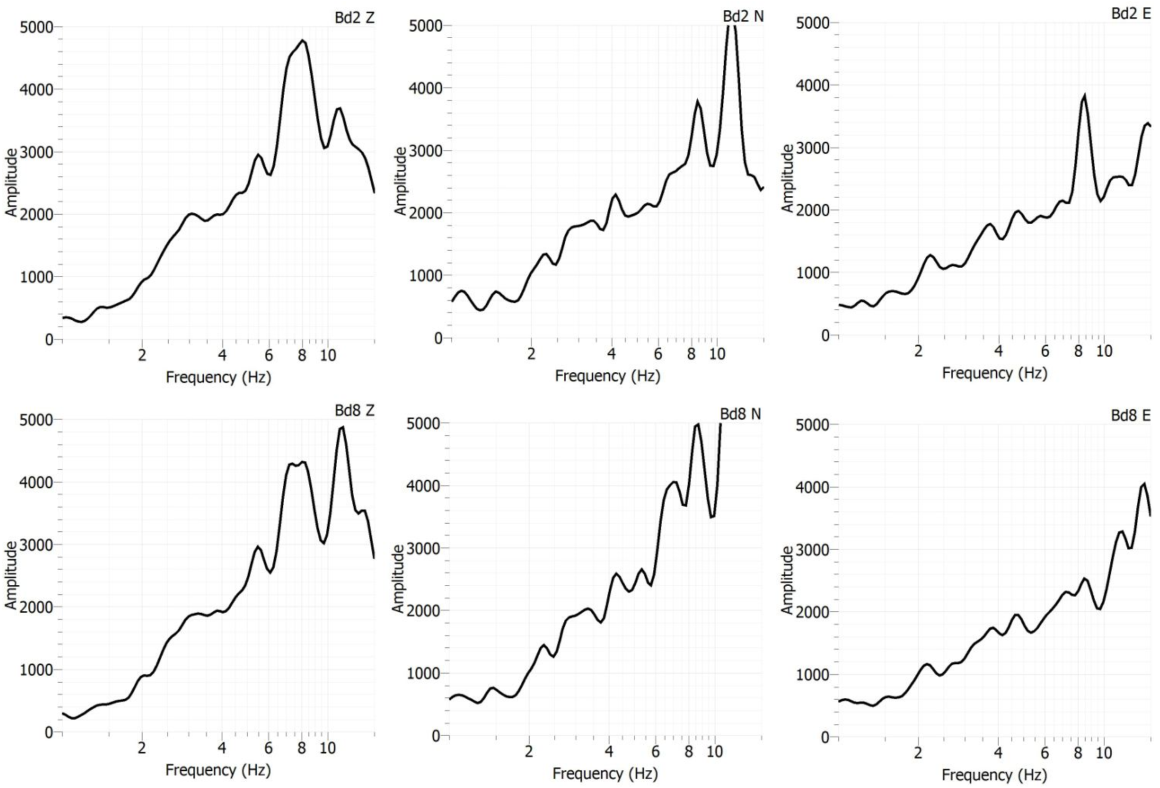

Figure 36: (Continued) Spectrum of 3C data measured in the borehole with records displayed upon depth, i.e. Bd3 through Bd8 correspond to top sensor through bottom sensor. Data was at a quiet time from 20:10-20:11 before beats. All borehole sensors showed roll-off below 4.5Hz casued by sensors and a feature of high amplitude at 8Hz.

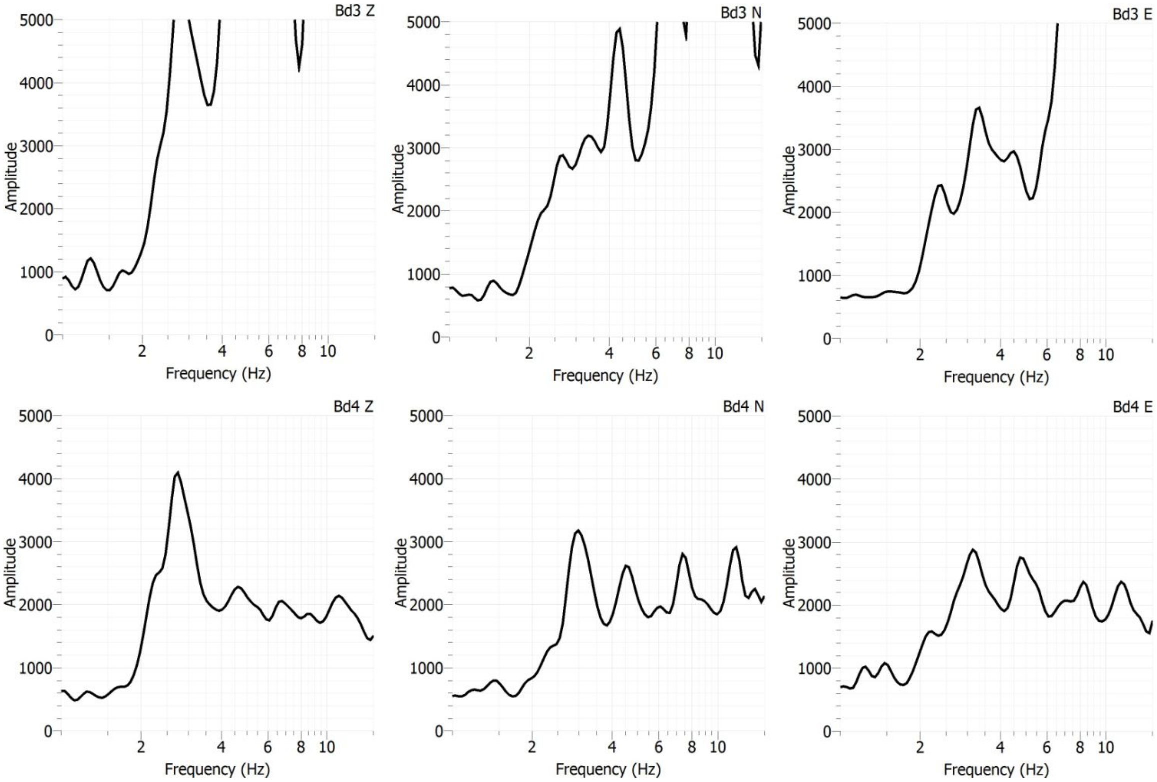

Figure 37: Spectrum of 3C data measured in the borehole with records displayed upon depth, i.e. Bd3 through Bd8 correspond to top sensor through bottom sensor. Data was at a quiet time from 20:43-20:44 after beats. All borehole sensors showed amplitude increase at 3Hz and amplitude attenuation at 8Hz. (continued on next page)

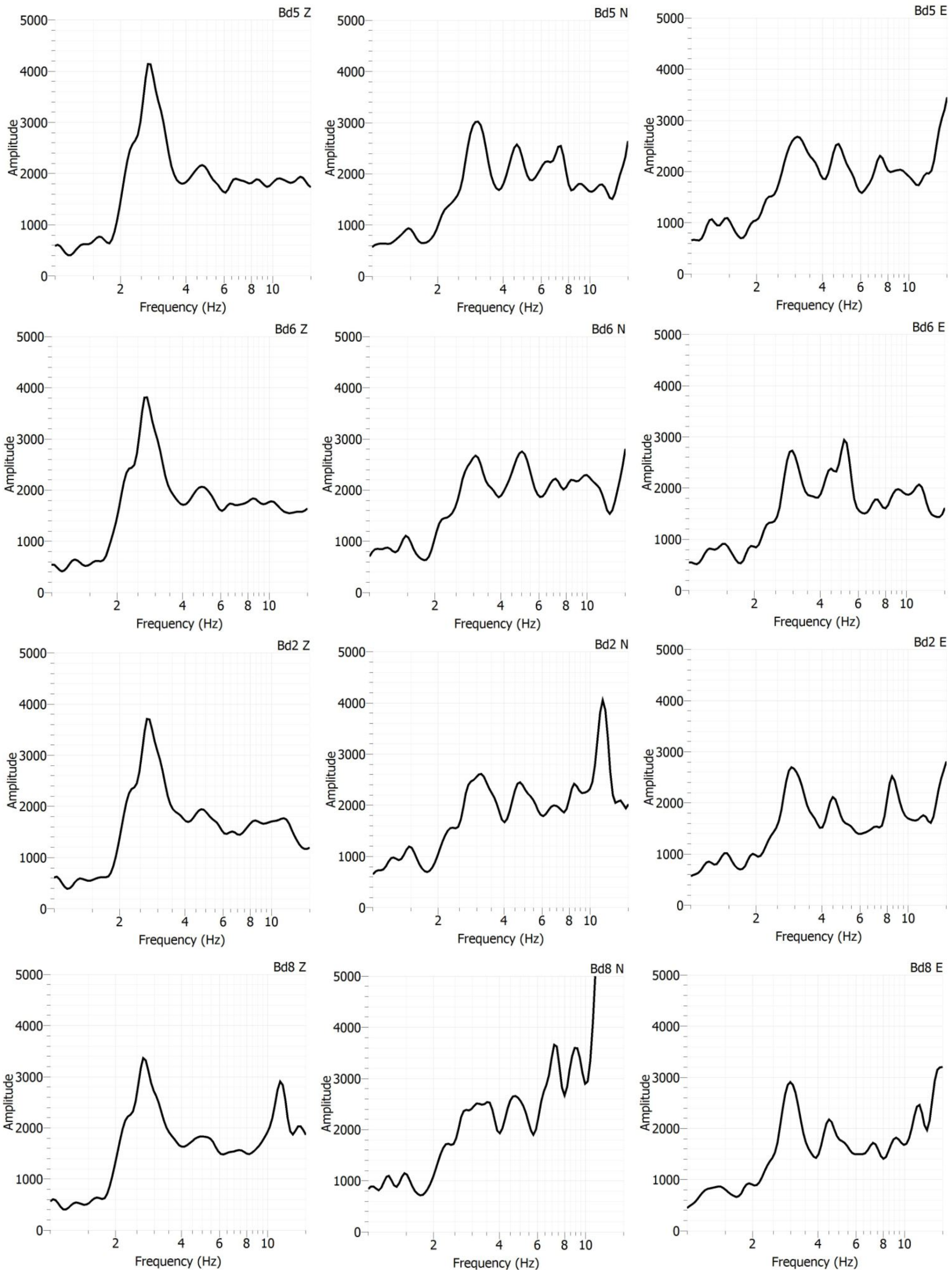

Figure 37: (Continued) Spectrum of 3C data measured in the borehole with records displayed upon depth, i.e. Bd3 through Bd8 correspond to top sensor through bottom sensor. Data was at a quiet time from 20:43-20:44 after beats. All borehole sensors showed amplitude increase at 3Hz and amplitude attenuation at 8Hz.

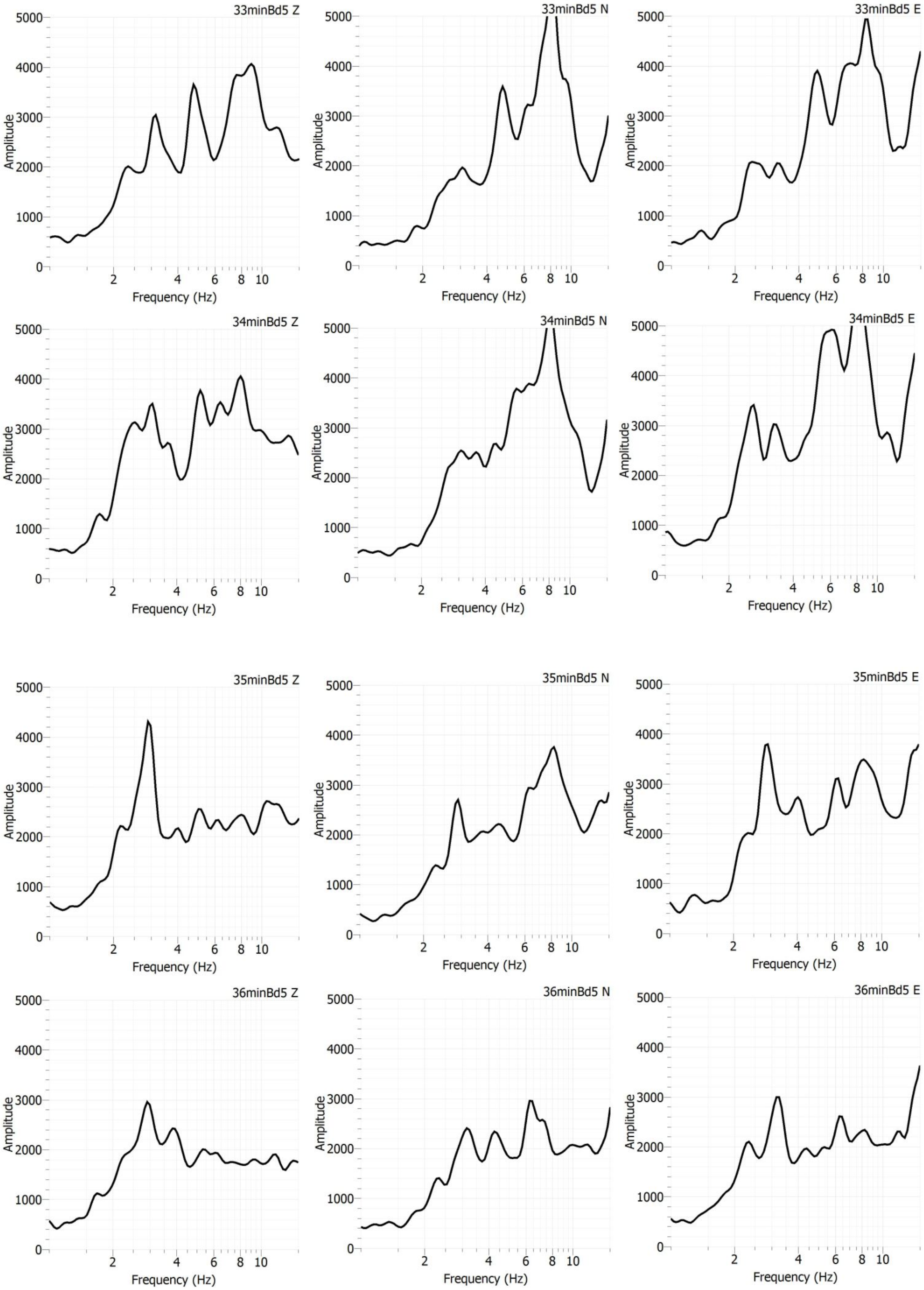

Figure 38: Track of spectrum variation at 3Hz from 20:33 to 20:47 in the borehole measurements from sensor 5. Beats occurred from 20:38 to 20:42. (continued on next page)

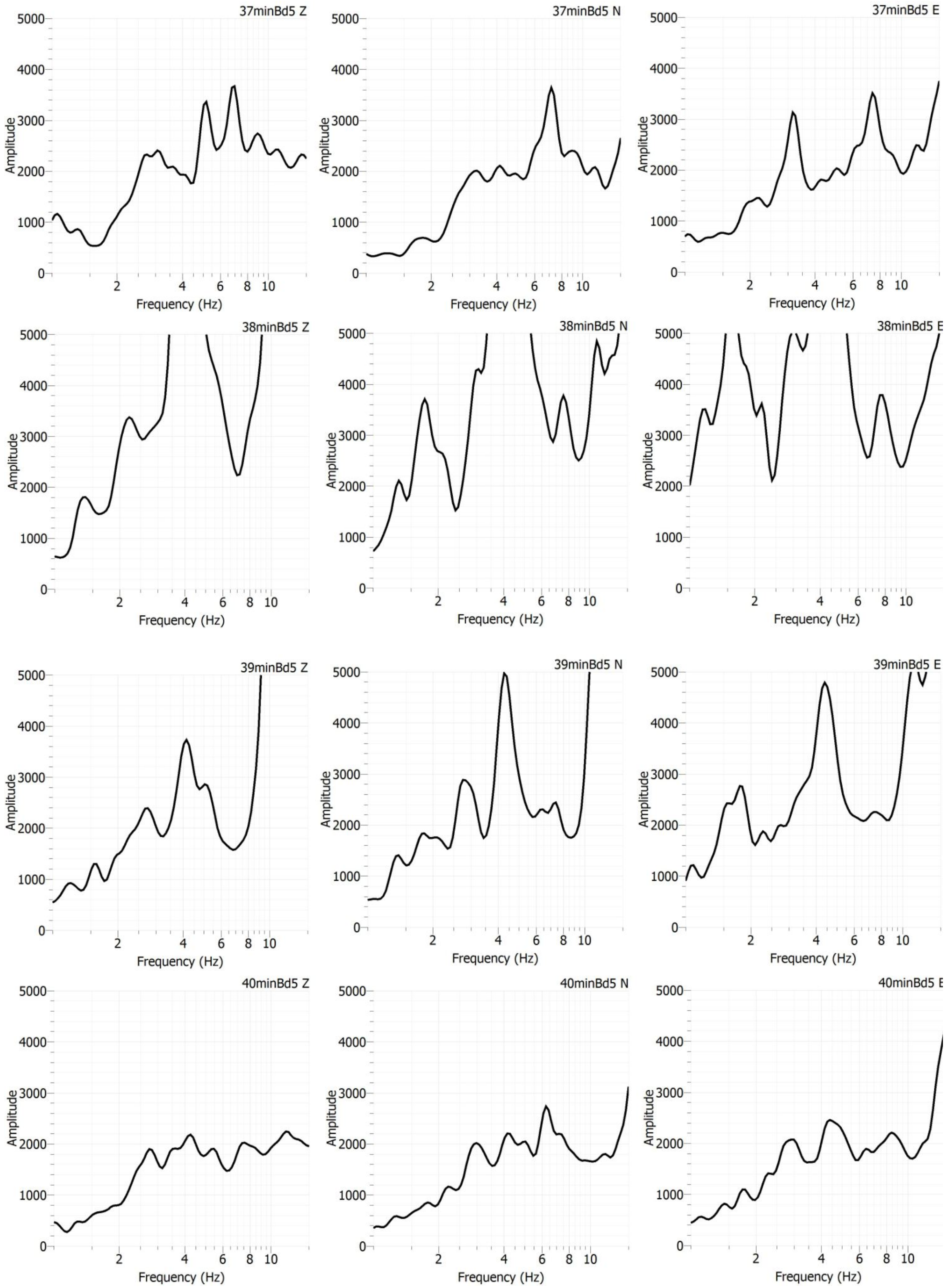

Figure 38: (Continued) Track of spectrum variation at 3Hz from 20:33 to 20:47 in the borehole measurements from sensor 5. Beats occurred from 20:38 to 20:42. (continued on next page)

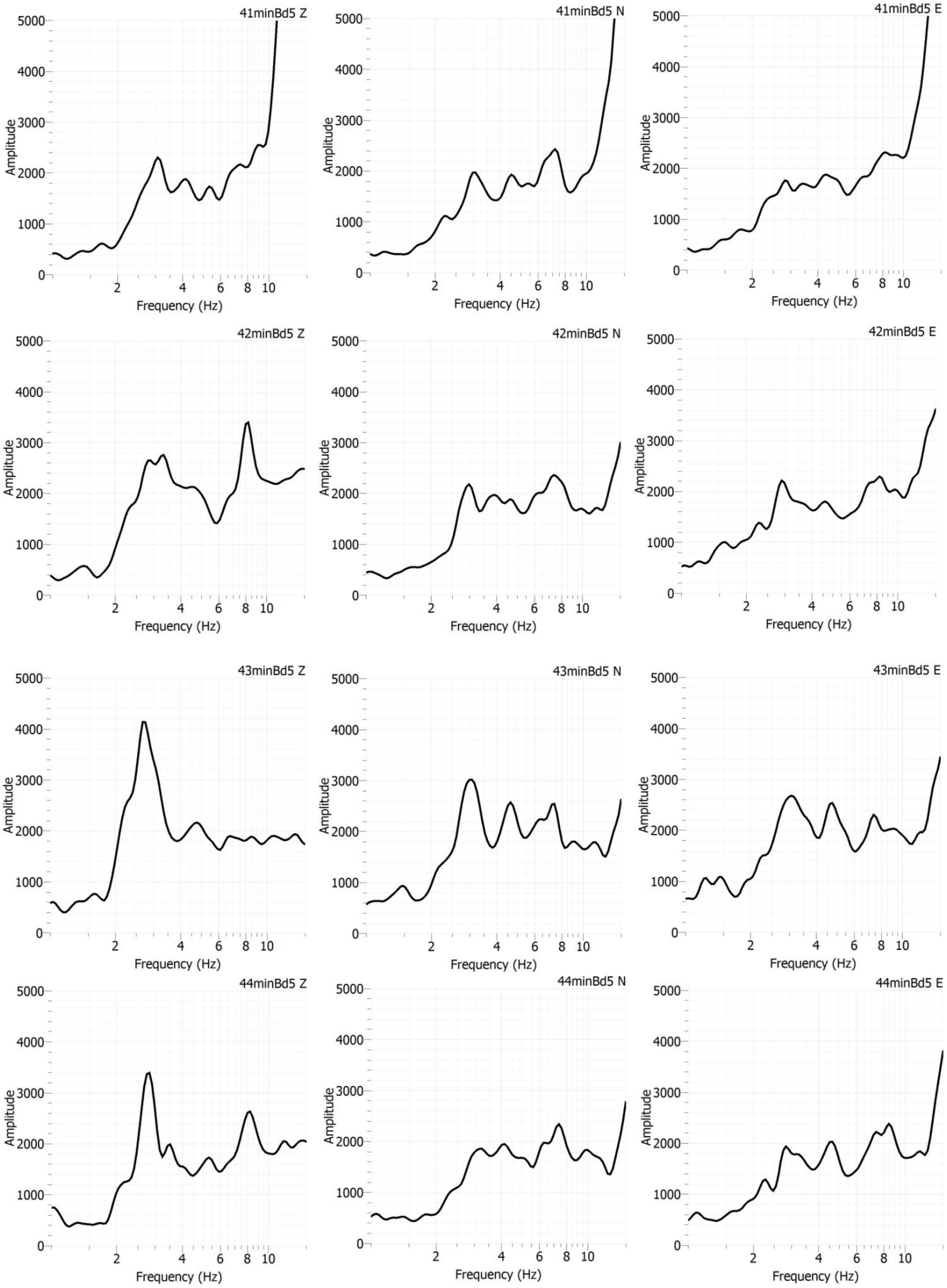

Figure 38: (Continued) Track of spectrum variation at 3Hz from 20:33 to 20:47 in the borehole measurements from sensor 5. Beats occurred from 20:38 to 20:42. (continued on next page)

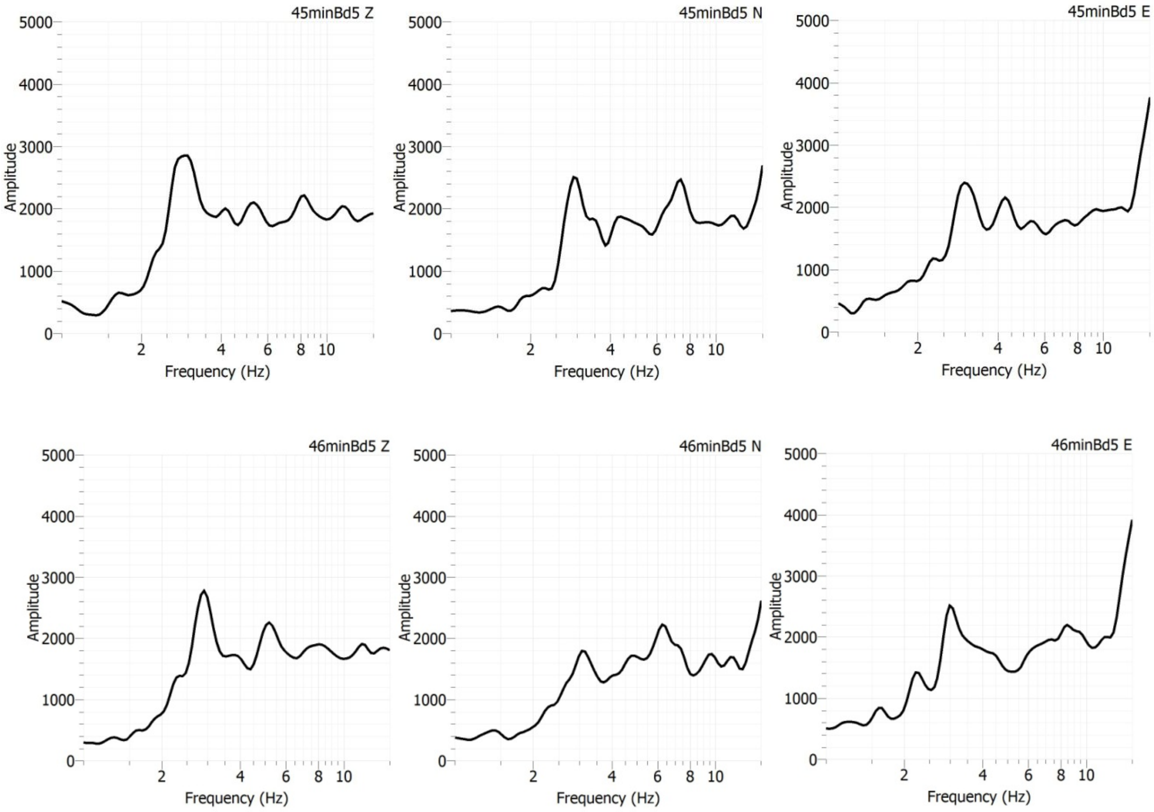

Figure 38: (Continued) Track of spectrum variation at 3Hz from 20:33 to 20:47 in the borehole measurements from sensor 5. Beats occurred from 20:38 to 20:42.

V/H-Ratio

This V/H attribute is based on the observation that the hydrocarbon-related energy anomaly is usually stronger in the vertical component compared to the horizontal components (Lambert 2007) and the V/H-ratio is more stable in time than the absolute spectra. The V/H spectral ratio normalized the vertical to the horizontal components, thus is independent of the spectrum attribute. If the general noise level is low, weak seismic signals associated with a low energy anomaly can induce a significant V/H signal value. This attribute analysis was done in Geopsy in a way that is similar to spectrum analysis using an H/V toolbox shown in Figure 39. V/H-ratio, in contrast to H/V, was obtained by simply editing the display of y-axis to be inversed. The H/V toolbox includes all the parameters needed for processing. The length of time window was chosen to be 60s and output frequency content was chosen as 1-15Hz. Once start button at the bottom was taped processing began.

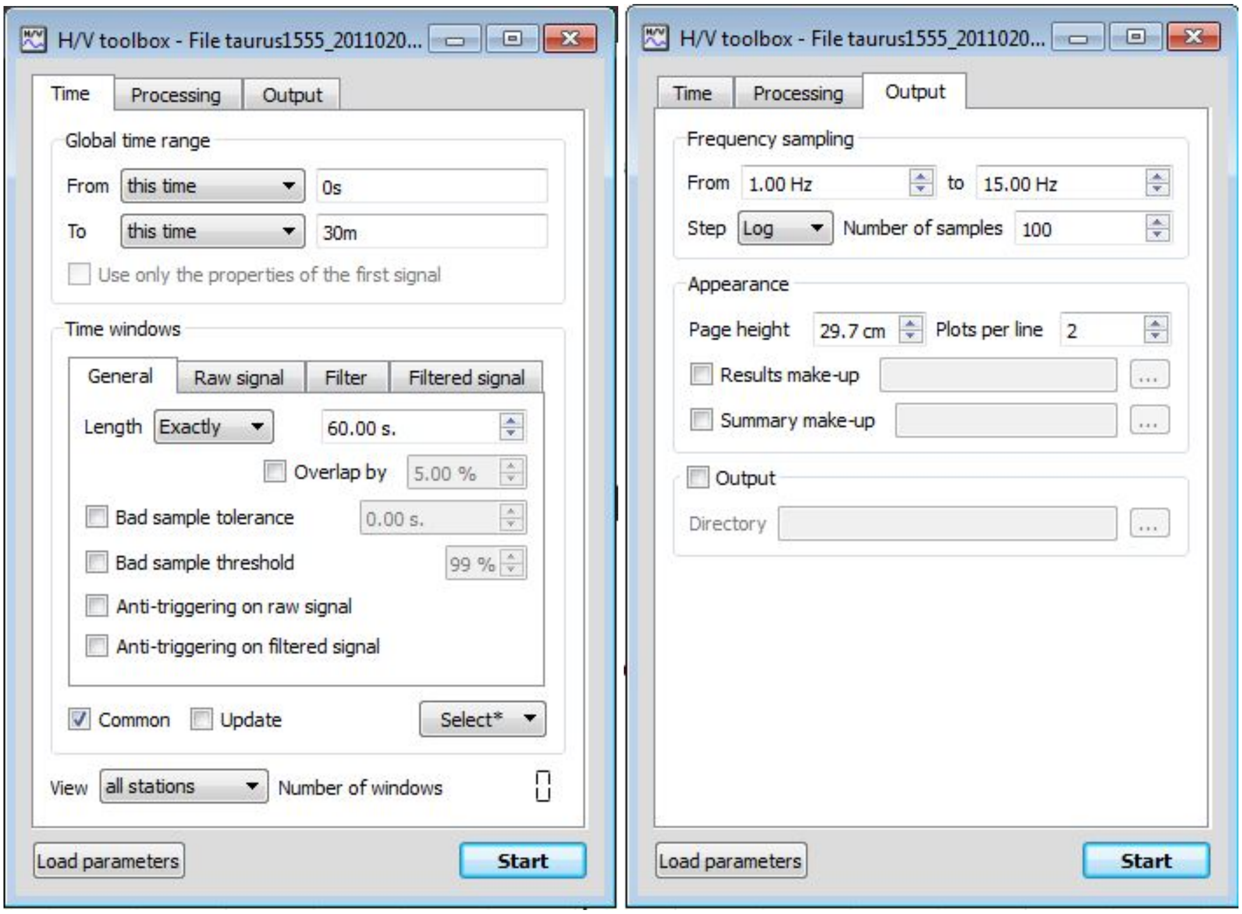

Global time range

From this time 0s

To this time 30m

☐ Use only the properties of the first signal

Time windows

Length Exactly 60.00 s.

☐ Overlap by 5.00 %

☐ Bad sample tolerance 0.00 s.

☐ Bad sample threshold 99 %

☐ Anti-triggering on raw signal

☐ Anti-triggering on filtered signal

☑ Common ☐ Update

View all stations Number of windows 0

Frequency sampling

From 1.00 Hz to 15.00 Hz

Step Log Number of samples 100

Appearance

Page height 29.7 cm Plots per line 2

☐ Results make-up

☐ Summary make-up

☐ Output

Directory

Figure 39: Time window length and frequency content used for V/H-ratio analysis.

Surface Records

As shown in Figure 40 a V/H peak was observed in the frequency band between 1-10Hz for the surface station 301 that was placed above the hydrocarbon reservoir. The amplitude of dominant peaks at ~3Hz was marked with a red star. A dashed line was plotted at V/H=1 to show that only amplitudes above the line indicated seismic energy that was dominant on vertical component. Since V/H normalized the vertical to the horizontal components, even weak signals can induce a significant V/H value, the V/H results should be interpreted in conjunction with the spectrum attributes. Before beats the record at station 301 that showed weak amplitudes in the 1-6Hz range however induced a value of below 1 at 3Hz in V/H spectral ratio. High amplitude at 8Hz on two horizontals in the spectrum attributes induced a trough of 0.15 at 8Hz, which makes sense since a trough in V/H value appears as a peak in H/V. This feature held constant on other surface records shown in Figure 41. Most to all surface records before beats showed a V/H value of below 1 at 3Hz and a trough of 0.1-0.3 at 8Hz.

After beats the record at station 301 that showed enhanced amplitude at 3Hz dominantly on vertical component in the spectrum attributes induced an increased value of 1.3 at 3Hz in the V/H ratio (Figure 40). The attenuation of 8Hz in spectrum attributes appeared as a trough at 8Hz in V/H ratio with the value increased from 0.15 before beats to 0.25 after beats. This feature was also present in other surface records shown in Figure 42. Most of the surface records after beats showed increased V/H ratio at 3Hz varied from 1.1 to 1.8 and a trough at 8Hz varied from 0.2 to 0.9. This increase at 3Hz in the spectral V/H ratio is an expected characteristic for P-waves originating from the below reservoir.

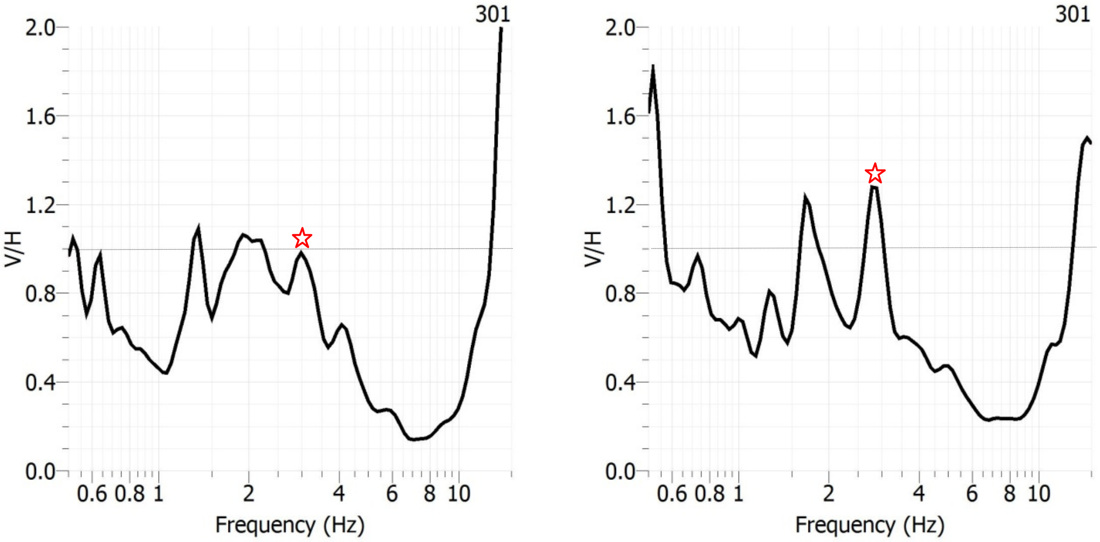

Figure 40: The V/H ratio of the seismic wavefield in the 1-15hz range for station 301. Left: Data before beats. Right: Data after beats. Red star represents the position of 3Hz. Dashed line represents the line of V/H=1.

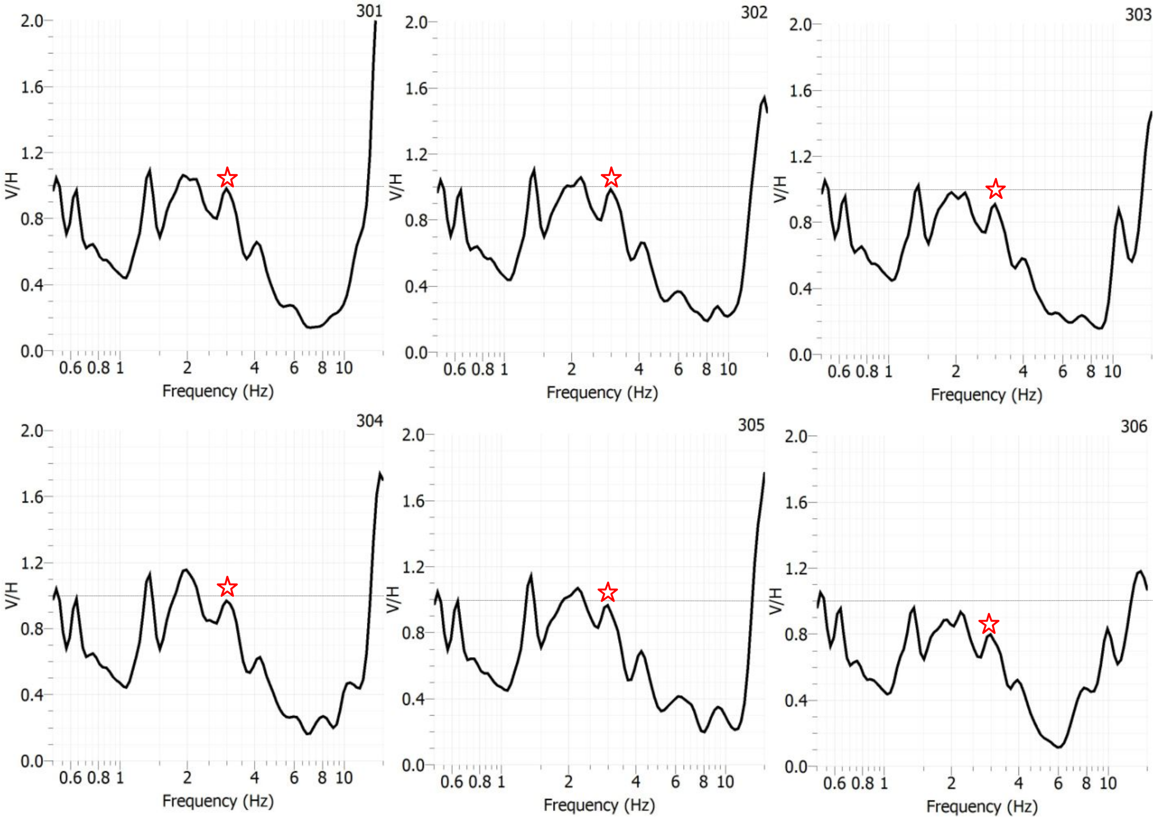

Figure 41: The V/H ratio of the seismic wavefield in the 1-15hz range for all surface stations 301-316 before beats. Red star represents the position of 3Hz. Dashed line represents the line of V/H=1. (continued on next page)

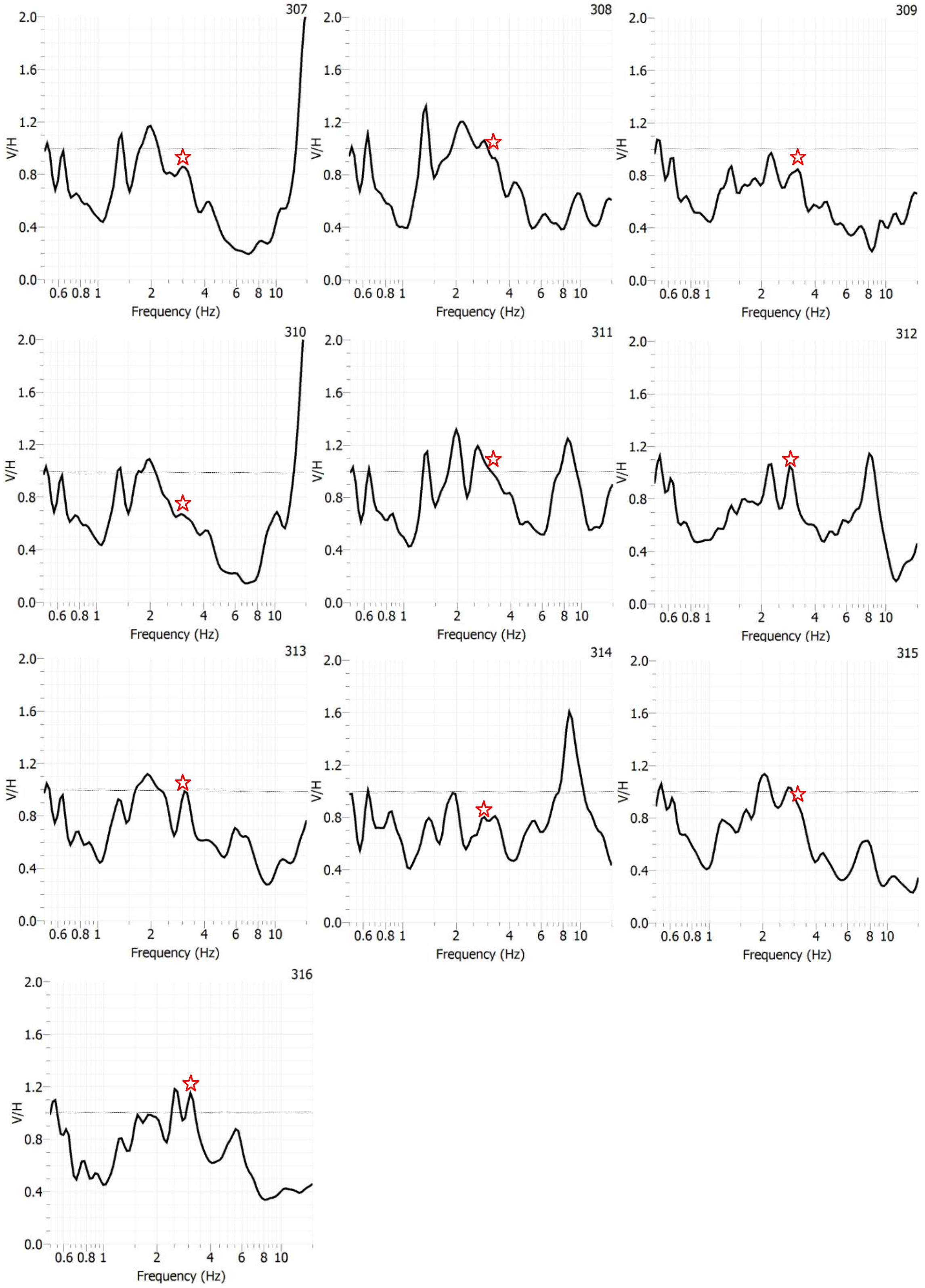

Figure 41: (Continued) The V/H ratio of the seismic wavefield in the 1-15hz range for all surface stations 301-316 before beats. Red star represents the position of 3Hz. Dashed line represents the line of V/H=1.

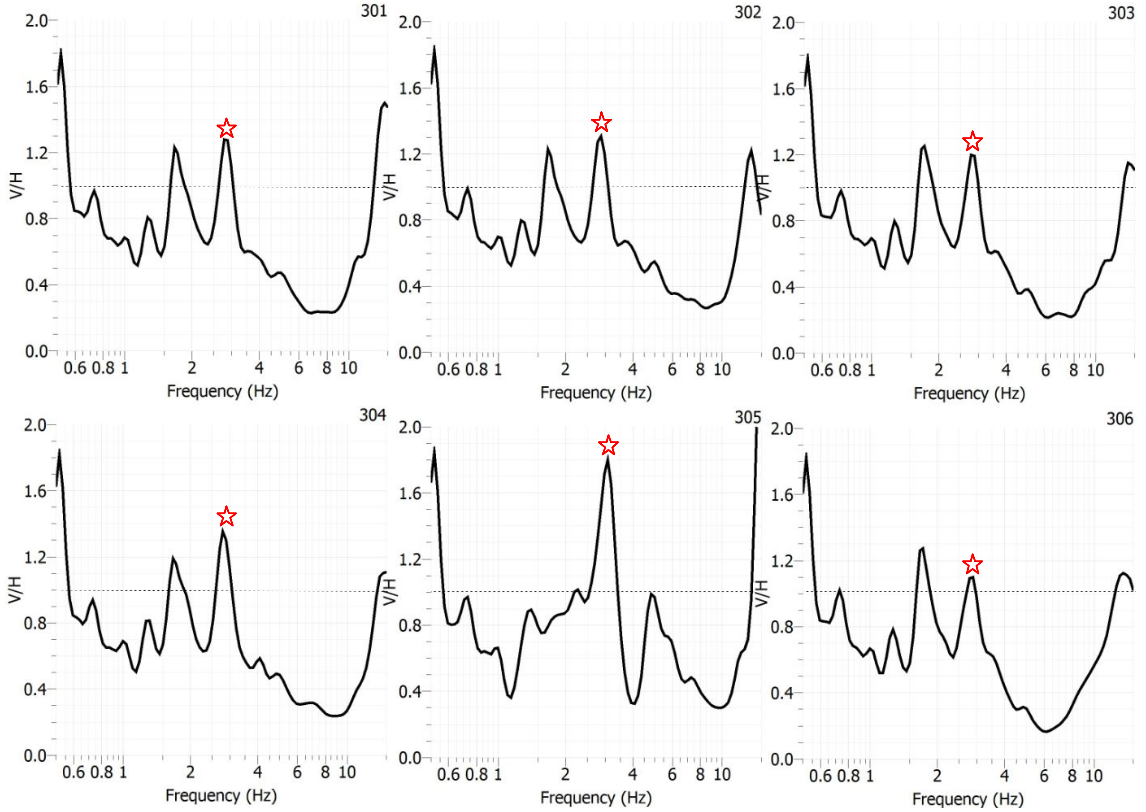

Figure 42: The V/H ratio of the seismic wavefield in the 1-15hz range for all surface stations 301-316 after beats. Red star represents the position of 3Hz. Dashed line represents the line of V/H=1. (continued on next page)

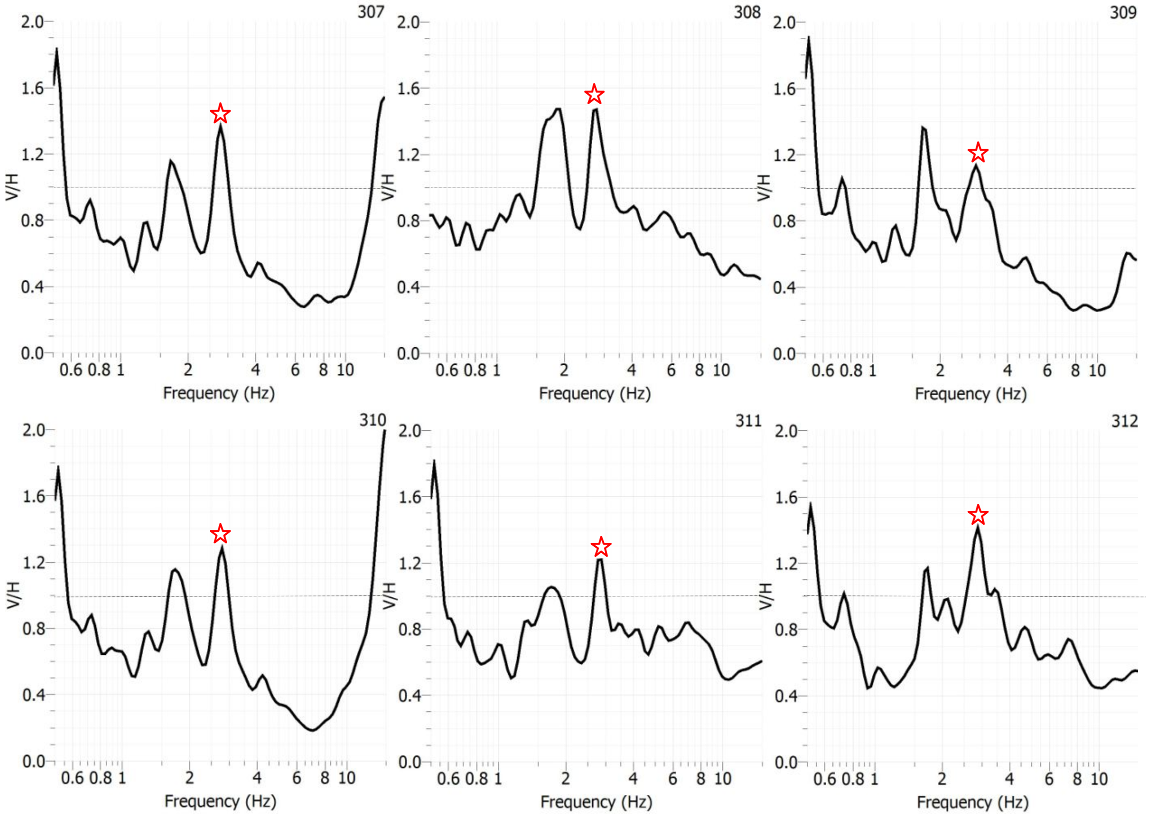

Figure 42: (Continued) The V/H ratio of the seismic wavefield in the 1-15hz range for all surface stations 301-316 after beats. Red star represents the position of 3Hz. Dashed line represents the line of V/H=1. (continued on next page)

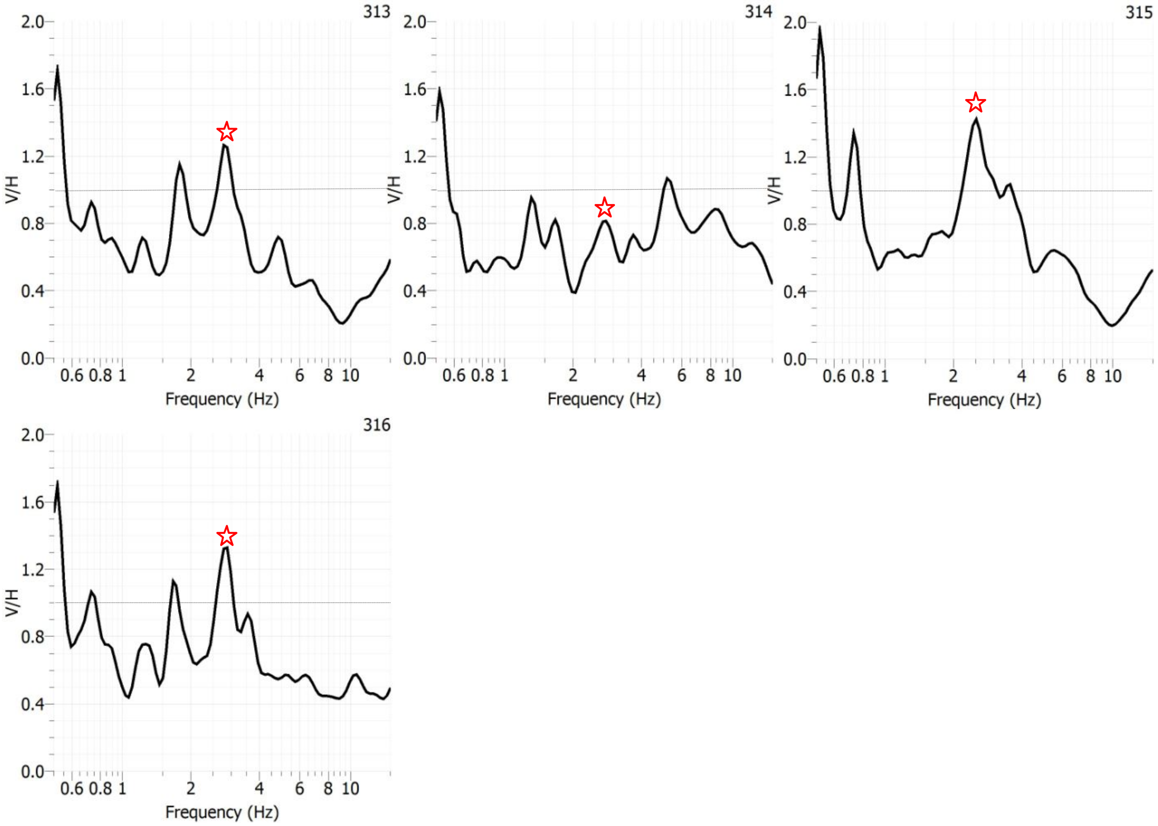

Figure 42: (Continued) The V/H ratio of the seismic wavefield in the 1-15hz range for all surface stations 301-316 after beats. Red star represents the position of 3Hz. Dashed line represents the line of V/H=1.

Borehole Records

Figure 43 shows a V/H peak observed in the frequency band between 1-15Hz for the borehole sensor 5 that was placed in the middle of the borehole array above the hydrocarbon reservoir. The amplitude of dominant peaks at ~3Hz was marked with a red star. A dashed line was plotted at V/H=1 to show that only amplitudes above the line indicated seismic energy that was dominant on vertical component. Before beats the record at sensor 5 that showed amplitudes roll-off below 4.5Hz induced a value of 1.2 at 3Hz in V/H spectral ratio, higher than that measured at surface. In contrast to the surface measurements, in the borehole records, the high amplitude at 8Hz in the spectrum attributes induced a peak of 1.85 at 8Hz since amplitude at 8Hz was highest on vertical component. This feature held constant on other borehole records shown in Figure 44. Most to all borehole records before beats showed a V/H value of 1.1-1.4 at 3Hz and a peak of 1.4 to over 2.0 at 8Hz.

After beats the record of sensor 5 that showed enhanced amplitude at 3Hz dominantly on vertical component in the spectrum attributes induced a peak at 3Hz in the V/H ratio with a value of 1.9 (Figure 43). The attenuation of 8Hz in spectrum attributes induced a value of 0.9 in V/H ratio. This feature was also present in other borehole records shown in Figure 45. Most of the borehole records after beats showed increased V/H ratio at 3Hz varied from 1.6 to over 2.0 and a low value at 8Hz varied from 0.6 to 0.9. This increase at 3Hz in the spectral V/H ratio is an expected characteristic for P-waves originating from the reservoir.

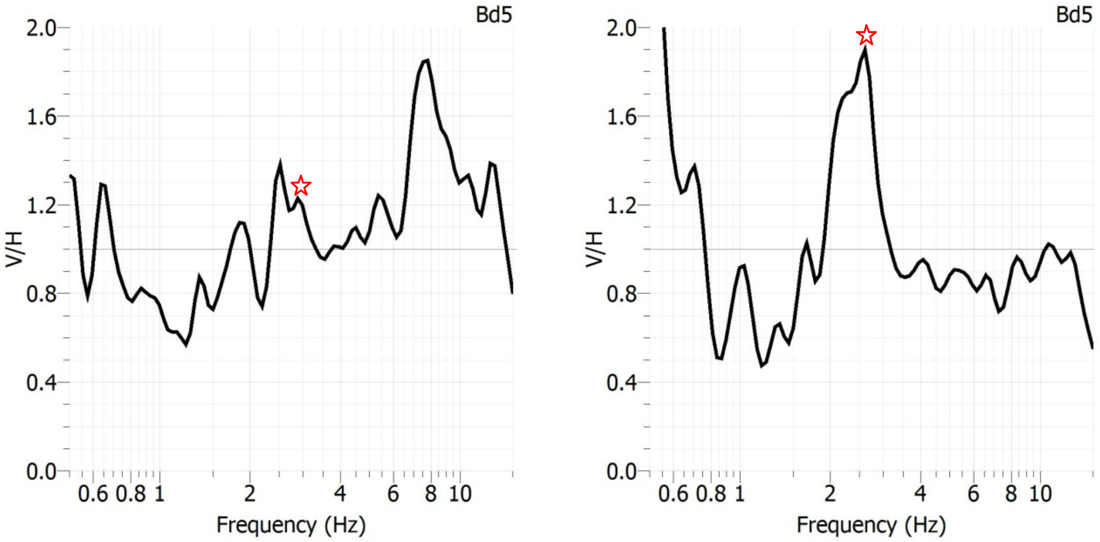

Figure 43: The V/H ratio of the seismic wavefield in the 1-15hz range for borehole sensor 5. Left: Data before beats. Right: Data after beats. Red star represents the position of 3Hz. Dashed line represents the line of V/H=1.

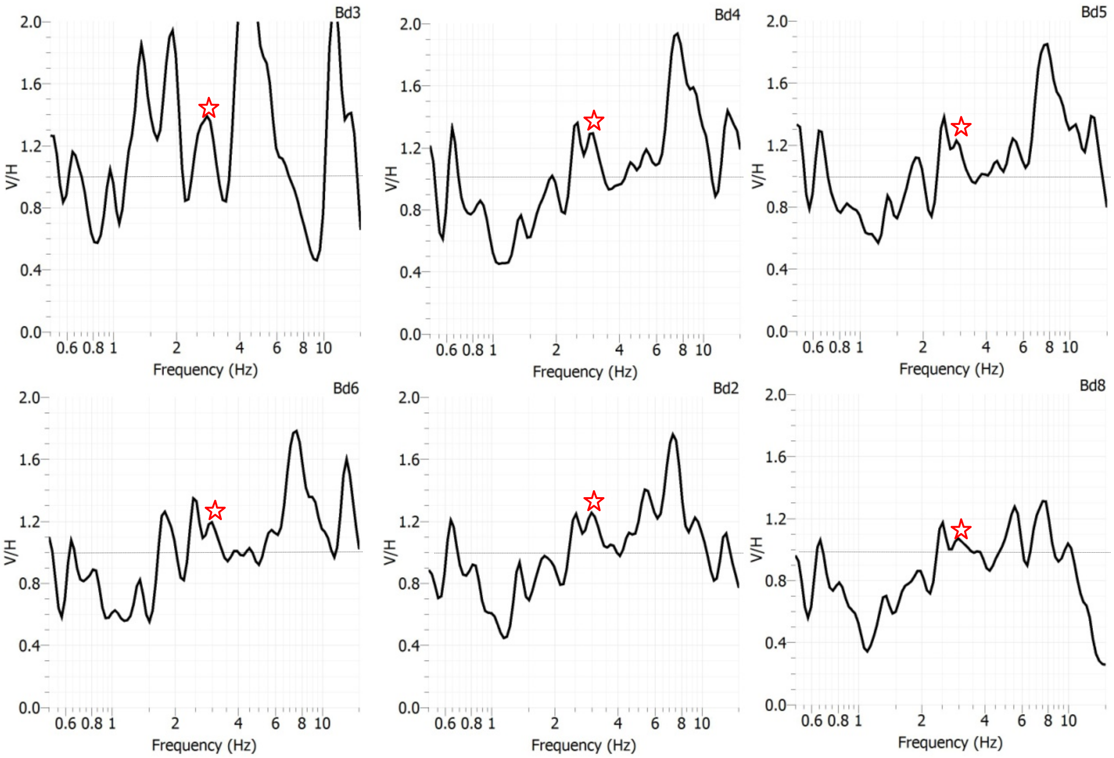

Figure 44: The V/H ratio of the seismic wavefield in the 1-15hz range for all borehole records from Bd3 through Bd8 before beats. Red star represents the position of 3Hz. Dashed line represents the line of V/H=1.

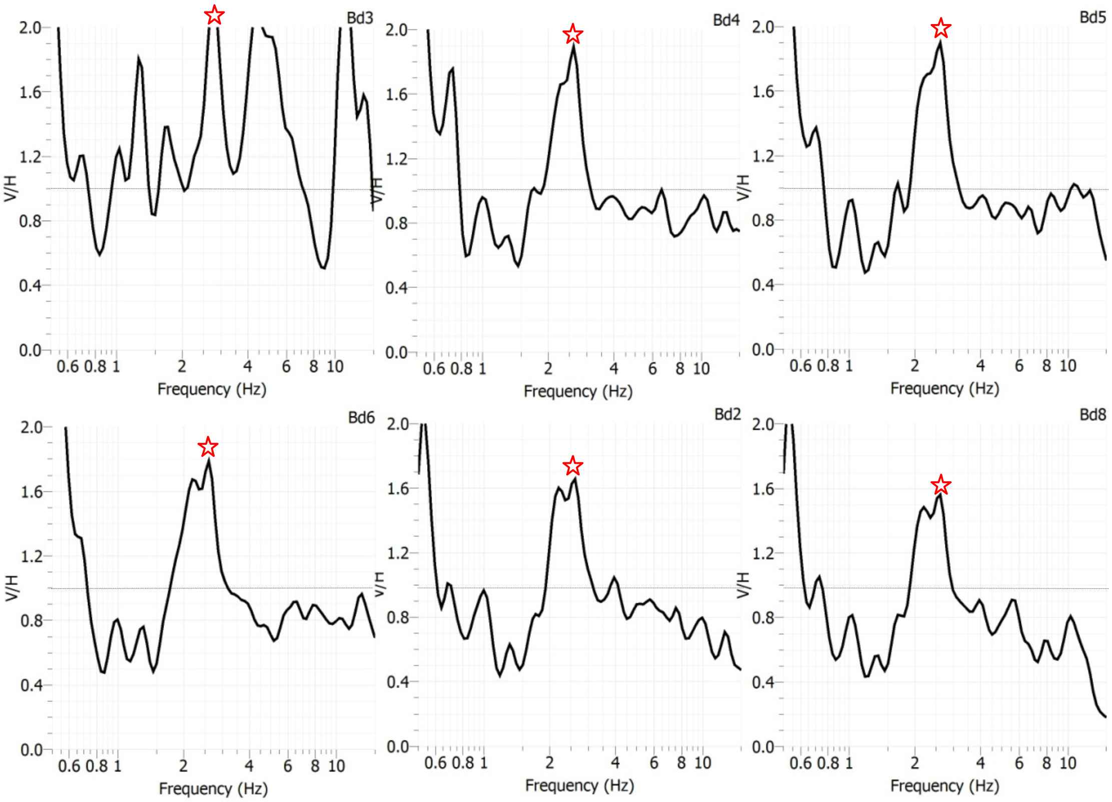

Figure 45: The V/H ratio of the seismic wavefield in the 1-15hz range for all borehole records from Bd3 through Bd8 after beats. Red star represents the position of 3Hz. Dashed line represents the line of V/H=1.

V Summary and Conclusion

The purpose of the research was to make the best use of borehole seismic data for subsurface information by processing efforts, and to find low frequency anomaly over hydrocarbons. Most raw data when first displayed had clear onset of direct arrivals as well as well-related noises that masked primary reflections. Direct arrivals were used for velocity determination which showed good correspondence with stacking velocity obtained from surface seismic data. FK filtering with trace mutes were successful in attenuating down-going waves and enhancing primary reflections. NMO correction was determined mathematically and corrected up-going reflections to zero offsets in two-way time that would be recorded at surface. The vertical stacking created a composite trace that contained only primary reflections, which matched with surface obtained formation tops very well. These formation tops were: the top of Packer Shell at 425ms and the top of Clinton Interval at 500ms. The beat test data obtained at both surface and borehole was analyzed for low frequency anomalies. Both two spectral attributes showed responses at 3Hz dominant on vertical component that were spectrum and V/H ratio. The 3Hz feature was verified in a track analysis of spectrum change through continuous time.

The results indicate that borehole seismic data provided a way of determining wave velocities with more detailed information than surface seismic survey. While it is suggested that energy source in a borehole check shot better to be placed at the same position and repeated for several times in order to generate data of good quality. Numerous noise contaminants in the records suggested that in any borehole seismic surveys borehole condition should be guaranteed to the first order otherwise noises would not be avoided. Borehole survey also provided a way of identifying subsurface formations that correlated with surface seismic sections very well. This research developed a way of processing borehole seismic data to recover the weak waves which were barely before processing. However, due to the limit array geometry, the borehole seismic data did not provided as many subsurface horizons as surface seismic did. It is recommended that efforts should be put on the arrangement of field geometry, array spread and receiver density in the future in order to get enough data to be used. The beats data showed very good response at 3Hz, but also showed high noise level at 8Hz from unknown source, therefore a suggestion would be that a beat test survey for low frequency anomaly analysis better be conducted at a time as quiet as possible.

VI Acknowledgements

I thank Spectraseis and Dominion East Ohio for providing the borehole data presented in the study, I thank Precision Geophysical for surface data acquisition, and Tom McGovern of Seismic Earth Resources Technology for the professional processing of the 2D seismic profiles.

I extend special thanks to Dr. Ernest Hauser for investing far more time and energy in instructing and reviewing this research. I thank Dr. Doyle Watts for valuable help and stimulating discussions. I thank Dr. David Dominic for helping and reviewing this research, and the valuable suggestions. I want to thank Dr. Fred Garber and Dr. Mateen Rizki for the help through MATLAB programme.

VII Bibliography

Ali, Mohammed Y., Braham Barkat, Karl A. Berteussen, and James Small. "A Low Frequency Passive Seismic Array Experiment over An Onshore Oil Field in Abu Dhabi, United Arab Emirates." *Geophysics78(4)*, 2013: B159-B176.

Brewer, Robert J. "VSP Data in Comparison to The Check Shot Velocity Survey." *Search and Discovery Artical#40059*, 2002.

Clay, Clarence S. *Elementary Exploration Seismology.* Englewood Cliffs, NJ: Prentice Hall, 1990.

Conrey, Guy Woolard. *The Geology of Wayne County, Ohio.* Ohio State University, 1921.

Coogan, Alan H. "Ohio's Surface Rocks and Sediments." *Bulletin-Ohio, Division of Geological Survey.* 1996. 31-50.

Daley, Thomas M., Roland Gritto, Ernest L. Majer, and Phillip West. "Tube-wave Suppression in Single-well Seismic Acquisition." *GEOPHYSICS 68(3)*, 2003: 863-869.

Dangel, S, M. E. Schaepman, E. P. Stoll, R. Carniel, O. Barzandji, E. -D Rode, and J. M. Singer. "Phenomenology of Tremor-Like Signals Observed over Hydrocarbon Reservoirs." *Volcanology and Geothermal Research*, 2003: 135-158.

Daures, R.and P. Tariel. "Applying Three-Component Records in Wave Field Seperation." *SEG Technical Program Expanded Abstracts.* Society of Exploration Geophysicists, 1985. 61-63.

Frehner, Marcel, Stefan M. Schmalholz and Yuri Podladchikov. "Spectral Modification of Seismic Waves Propagating through Solids Exhibiting A Resonance Frequency: A 1-D Coupled Wave Propagation-Oscillation Model." *Geophysical Journal International 176(2)*, 2009: 589-600.

Goertz, Alex, Konrad Cieślik, Ernest Hauser, Gary Watts, Steve McCrossin, Phil Zbasnik. "A Combined Borehole/Surface Broadband Passive Survey over A Gas Storage Field." *SEG Technical Program Expanded Abstracts.* 2011. 1488-1492.

Gulati, Jitendra S., Robert R. Stewart, Janusz Peron, and John M. Parkin. "3C-3D VSP: Normal Moveout Correction and VSPCDP Transformation." CREWES Research Report, 1997.

Hardage, Bob A. "An Examination of Tube Wave Noise in Vertical Seismic Profiling Data." *Geophysics 46(6)*, 1981: 892-903.

Hardage, Bob A. *Vertocal Seismic Profiling.* London: Geophysical Press, 1983.

Hinds, Ronald Clifford, Neil Lennart Anderson, Richard Dwight Kuzmiski. *VSP Interpretive Processing: Theory and Practice.* Tulsa, OK: SEG Books, 1996.

Kearey, Philip, Michael Brooks, Ian Hill. *An Introduction to Geophysical Exploration, 3rd Edition.* Wiley, 2002.

Knowlton, Kelly B., and Terry W. Spencer. "Polarization Measurement Uncertainty on Three-Component VSP." *Geophysics 61(2)*, 1996: 594-599.

Lambert, Marc, Stefan M. Schmalholz, Erik H. Saenger, and Yuri Y. Podladchikov. "Low Frequency Anomalies in Spectral Ratios of Single Station Microtremor Measurements: Observations Across An Oil and Gas Field in Austria." *SEG Technical Program Expanded Abstracts.* 2007. 1352-1356.

Lambert, Marc-André, Stefan M. Schmalholz, Erik H. Saenger, Brian Steiner. "Low Frequency Microtrmor Anomalies at An Oil and Gas Field in Voitsdorf, Austria." *Geophysical Prospecting* 57, no. 3 (May 2009): 393-411.

Mari, Jean-Luc, Françoise Coppens. *Well Seismic Surveying.* Editions TECHNIP, 2003.

Quintal, Beatriz, Stefan M. Schmalholz, Yuri Y. Podladchikov. "Low Frequency Reflections from A Thin Layer with High Attenuation Caused by Interlayer Flow." *Geophysics* (Geophysics) 74 (January-February 2009): N15-N26.

Riggs, Emmet D. "Seismic Wave Types in A Borehole." *Geophysics*, January 1955: 53-67.

Saenger, Erik H., Stefan M. Schmalholz, Marc-A. Lambert, Tung T. Nguyen, Arnaud Torres, Sabrina Metzger, Robert M. Habiger, Tamara Müller, Susanne Rentsch, and Efraín Méndez-Hernández. "A Passive Seismic Survey over A Gas Field: Analysis of Low-Frequency Anlomalies." *Geophysics* 74 (March 2009): O29-O40.

Singh, O. P., and M. Bhanu. "3-Component Processing of VSP Data." *9th Biennial International conference & Exposition on Petroleum Geophysics.* 2012. 232-236.

Wightman, W Ed, Frank Jalinoos, Philip Sirles, Kanaan Hanna. *Application of Geophysical Methods to Highway Related Problems.* FHWA-IF-04-021, Lakewood, CO: Federal Highway Administration, Central Federal Lands Highway Division, 2004.

Yilmaz. *Seismic Data Analysis: Processing, Inversion, and Interpretation of Seismic Data.* Tulsa, OK: SEG Books , 2000.

VIII APPENDIX

Appendix A

Convert Passcal SEG-Y to SEG-Y

Data recorded by the 3C borehole array was delivered in Passcal SEG-Y format, and can be loaded using the MATLAB reader:

The raw data files are stored and named as following:

Example:

```
/Cardinal3/raw-data/325789/added/*_1.rsy
/Cardinal3/raw-data/325789/added/*_2.rsy
/Cardinal3/raw-data/325789/added/*_3.rsy
```

, corresponding to recordings with RIO-ID 325789. Files names ending with the number 1 refer to the vertical component of the measurement. The numbers 2 and 3 refer to the two horizontal components H1 and H2, respectively. Figure 46 is an example of MATLAB script used on the data recorded at the first depth array.

To read Passcal. SEG-Y data, use MATLAB command:

```
[temp,streamid,sps,ist,header]=s6_readpasscalfile(fn{i});
```

To extract data with a length of 1s, use MATLAB command:

```
Data=temp(StartTime:(StartTime + TimeLength));
```

To convert the data to SEG-Y format, use MATLAB command:

```
WriteSegy('Data.segy',Data)
```

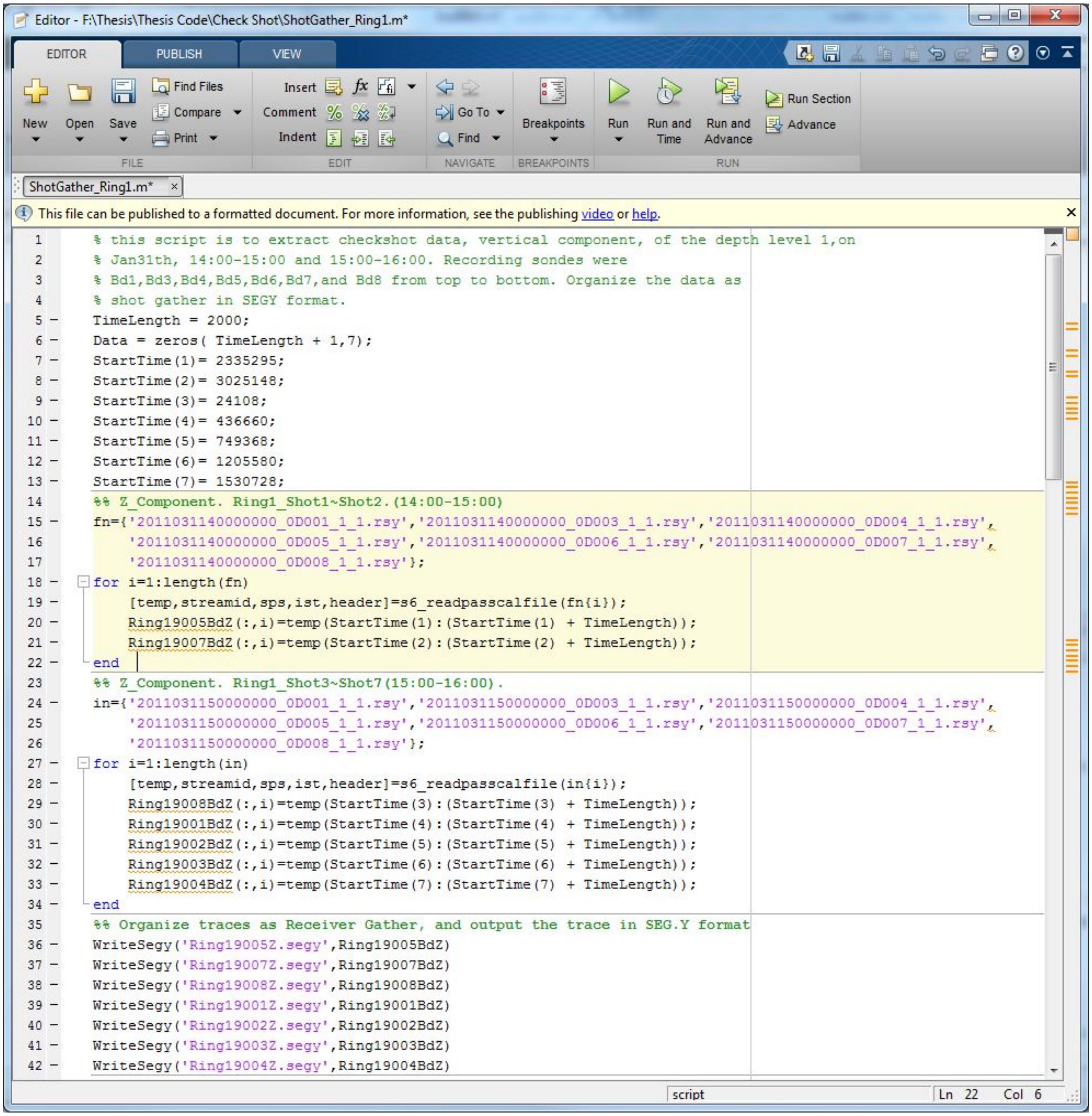

This file can be published to a formatted document. For more information, see the publishing video or help.

```
% this script is to extract checkshot data, vertical component, of the depth level 1,on
% Jan31th, 14:00-15:00 and 15:00-16:00. Recording sondes were
% Bd1,Bd3,Bd4,Bd5,Bd6,Bd7,and Bd8 from top to bottom. Organize the data as
% shot gather in SEGY format.
TimeLength = 2000;
Data = zeros( TimeLength + 1,7);
StartTime(1)= 2335295;
StartTime(2)= 3025148;
StartTime(3)= 24108;
StartTime(4)= 436660;
StartTime(5)= 749368;
StartTime(6)= 1205580;
StartTime(7)= 1530728;
%% Z_Component. Ring1_Shot1~Shot2.(14:00-15:00)
fn={'2011031140000000_0D001_1_1.rsy','2011031140000000_0D003_1_1.rsy','2011031140000000_0D004_1_1.rsy',...
    '2011031140000000_0D005_1_1.rsy','2011031140000000_0D006_1_1.rsy','2011031140000000_0D007_1_1.rsy',...
    '2011031140000000_0D008_1_1.rsy'};
for i=1:length(fn)
    [temp,streamid,sps,ist,header]=s6_readpasscalfile(fn{i});
    Ring19005BdZ(:,i)=temp(StartTime(1):(StartTime(1) + TimeLength));
    Ring19007BdZ(:,i)=temp(StartTime(2):(StartTime(2) + TimeLength));
end
%% Z_Component. Ring1_Shot3~Shot7(15:00-16:00).
in={'2011031150000000_0D001_1_1.rsy','2011031150000000_0D003_1_1.rsy','2011031150000000_0D004_1_1.rsy',...
    '2011031150000000_0D005_1_1.rsy','2011031150000000_0D006_1_1.rsy','2011031150000000_0D007_1_1.rsy',...
    '2011031150000000_0D008_1_1.rsy'};
for i=1:length(in)
    [temp,streamid,sps,ist,header]=s6_readpasscalfile(in{i});
    Ring19008BdZ(:,i)=temp(StartTime(3):(StartTime(3) + TimeLength));
    Ring19001BdZ(:,i)=temp(StartTime(4):(StartTime(4) + TimeLength));
    Ring19002BdZ(:,i)=temp(StartTime(5):(StartTime(5) + TimeLength));
    Ring19003BdZ(:,i)=temp(StartTime(6):(StartTime(6) + TimeLength));
    Ring19004BdZ(:,i)=temp(StartTime(7):(StartTime(7) + TimeLength));
end
%% Organize traces as Receiver Gather, and output the trace in SEG.Y format
WriteSegy('Ring19005Z.segy',Ring19005BdZ)
WriteSegy('Ring19007Z.segy',Ring19007BdZ)
WriteSegy('Ring19008Z.segy',Ring19008BdZ)
WriteSegy('Ring19001Z.segy',Ring19001BdZ)
WriteSegy('Ring19002Z.segy',Ring19002BdZ)
WriteSegy('Ring19003Z.segy',Ring19003BdZ)
WriteSegy('Ring19004Z.segy',Ring19004BdZ)
```

Figure 46: MATLAB script for check-shot data extraction, re-organization, and SEGY format conversion.

Appendix B

Borehole noise contamination

Figure 47 shows an example of noisy data possibly caused by bad cementation. The data was recorded at the second depth array where cementation was bad. The strong noise level and resonance completely mask any up-going or down-going events such that one can hardly identify first arrivals from such noisy record.

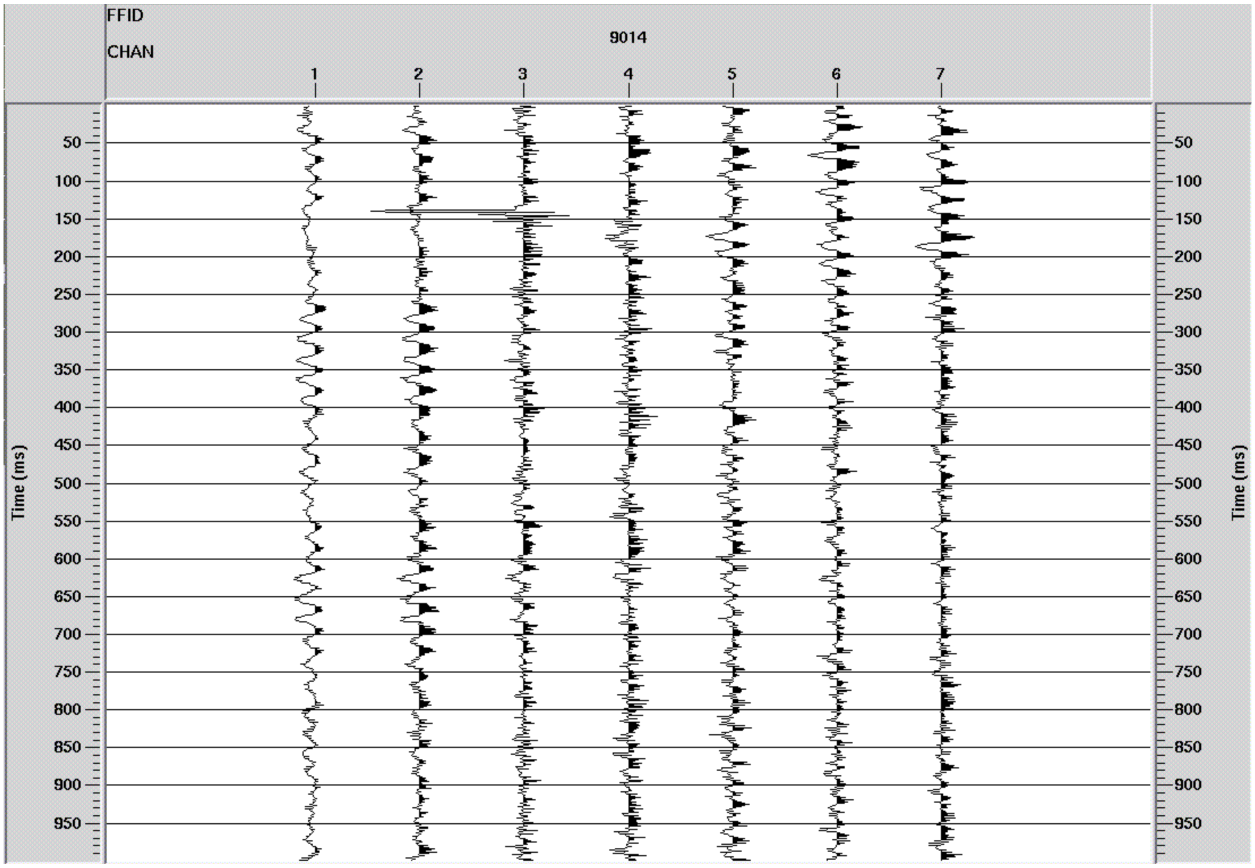

Figure 47: Example of noisy data affected by bad cementation.

Figure 48 shows an example of noisy data affected by loose geophone clamping. The response of the unlocked geophone before the high amplitude first arrival represents noise that was transmitted down the tubing.

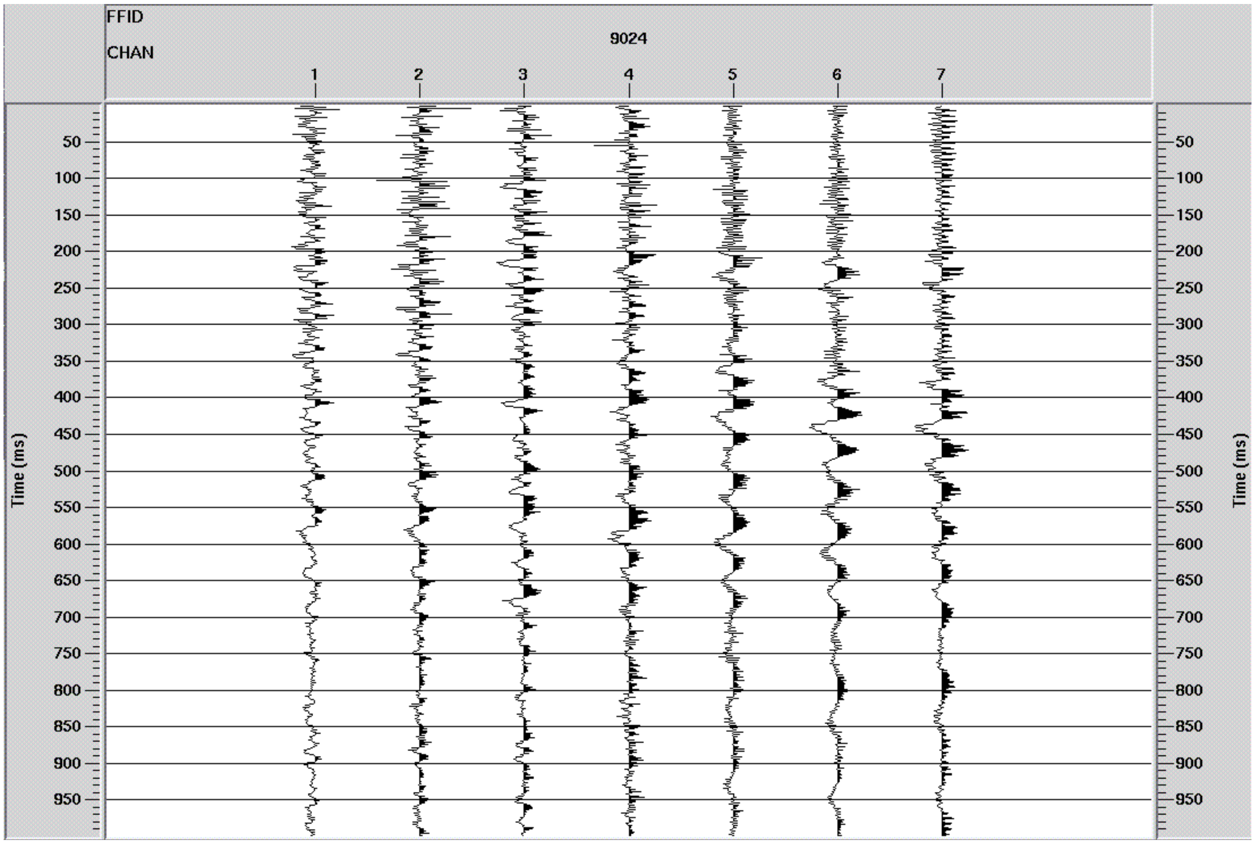

Figure 48: Example of noisy data affected by loose geophone clamping.

Appendix C

First arrival determination using a time window

A time window was used that covered the half wave period of first arrival and dominant frequency can be calculated as the reverse of wave period (f=1/T). Selection of the time window was based on Knowlton and Spencer (1996)'s tests of uncertainties of particle polarization measurement made with different time windows located at the peak amplitude and at other locations (Figure 49). One would believe window C which includes the peak of maximum amplitude should have the most accurate measurement because this is where the SNR is the highest. However, Knowlton and Spencer (1996) showed that measurements made over window A generally contained the least scatter and least uncertainty compared to window B and C. Based on this research, the time window A was selected for determining half wave period, and the window covered the whole half-wave cycle, starting from the time when the amplitude was zero till the time when the amplitude went back to zero. Thus the half wave period is calculated as the length of this chosen half cycle.

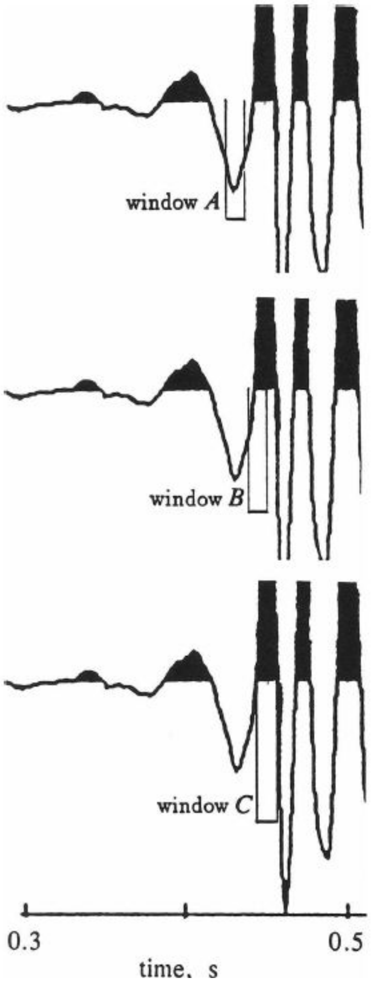

Figure 49: Time windows used in analysis of first arrival. Window C is centered at the peak of maximum amplitude **(Knowlton 1996)**.

Appendix D

Cross-correlation method applied for determination of time shifts

The cross-correlation on MATLAB applies syntax:

```
c(:, i)=xcorr(x, y)
```

,in which x and y are two finite segments of row vectors for input, and parameter i corresponds to trace numbers. For example, time window of data sourced from FFID9005 was 88:161, so the syntax applied was: c(:, i)=xcorr(88, 161). X and y varied with different traces, for data sourced from FFID9007, time window was 103:181, therefore the syntax applied should be: c(:, i)=xcorr(103, 181). c(:, i)=xcorr(x, y) estimates the cross-correlation sequence of a random process through Equation 1:

Equation 1

$$R_{xy}(m) = E(x_{n+m}y_n^*) = E(x_n y_{n-m}^*)$$

, where x_n and y_n are jointly stationary random processes, $-\infty < n < \infty$, and E is the expected value operator. c(:, i)=xcorr(x, y) returns the cross-correlation sequence in a length 2*N-1 vector, where N (N>1) is the length of (x, y). For instance, input vectors x and y for cross-correlation of FFID9005 were 88 and 161 which made the length N equaled: N=161-88+1=74 and the length vector: 2*N-1= 2*74-1= 147.

To get the value and the index of the maximum correlation, use MATLAB syntax:

```
[value, index]=max(c)
```

To get the time shift between two successive traces, use MATLAB command:

```
t=index(i)-index(i-1).
```

Figure 50 is an example of MATLAB script used for cross-correlation of the data recorded at the first depth level. 7 cross-correlations were done with changed time windows for calculation since there were 7 dynamite sources. The parameter i corresponds to trace number varied from 1 to 7. The traces were all cross-correlated to a single trace that had the best developed first arrivals.

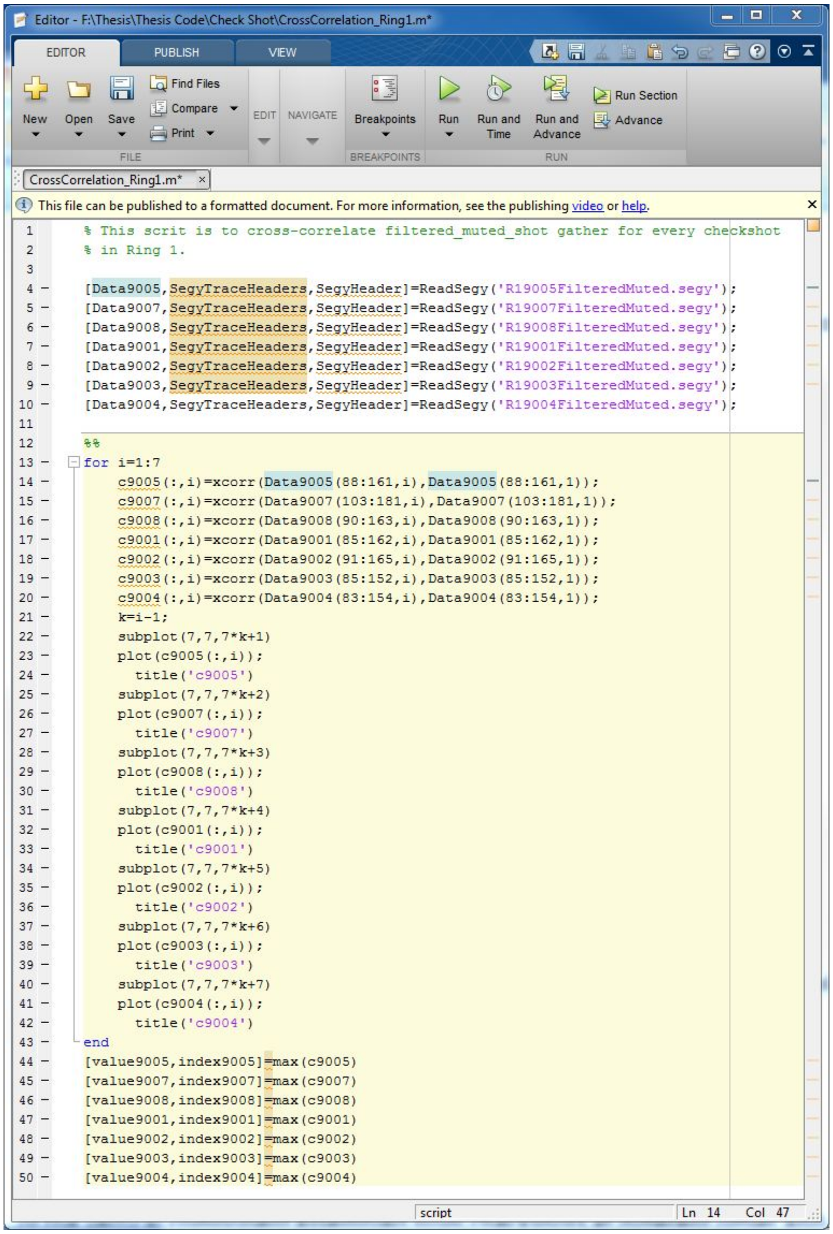

This file can be published to a formatted document. For more information, see the publishing video or help.

```
% This scrit is to cross-correlate filtered_muted_shot gather for every checkshot
% in Ring 1.

[Data9005,SegyTraceHeaders,SegyHeader]=ReadSegy('R19005FilteredMuted.segy');
[Data9007,SegyTraceHeaders,SegyHeader]=ReadSegy('R19007FilteredMuted.segy');
[Data9008,SegyTraceHeaders,SegyHeader]=ReadSegy('R19008FilteredMuted.segy');
[Data9001,SegyTraceHeaders,SegyHeader]=ReadSegy('R19001FilteredMuted.segy');
[Data9002,SegyTraceHeaders,SegyHeader]=ReadSegy('R19002FilteredMuted.segy');
[Data9003,SegyTraceHeaders,SegyHeader]=ReadSegy('R19003FilteredMuted.segy');
[Data9004,SegyTraceHeaders,SegyHeader]=ReadSegy('R19004FilteredMuted.segy');

%%
for i=1:7
    c9005(:,i)=xcorr(Data9005(88:161,i),Data9005(88:161,1));
    c9007(:,i)=xcorr(Data9007(103:181,i),Data9007(103:181,1));
    c9008(:,i)=xcorr(Data9008(90:163,i),Data9008(90:163,1));
    c9001(:,i)=xcorr(Data9001(85:162,i),Data9001(85:162,1));
    c9002(:,i)=xcorr(Data9002(91:165,i),Data9002(91:165,1));
    c9003(:,i)=xcorr(Data9003(85:152,i),Data9003(85:152,1));
    c9004(:,i)=xcorr(Data9004(83:154,i),Data9004(83:154,1));
    k=i-1;
    subplot(7,7,7*k+1)
    plot(c9005(:,i));
      title('c9005')
    subplot(7,7,7*k+2)
    plot(c9007(:,i));
      title('c9007')
    subplot(7,7,7*k+3)
    plot(c9008(:,i));
      title('c9008')
    subplot(7,7,7*k+4)
    plot(c9001(:,i));
      title('c9001')
    subplot(7,7,7*k+5)
    plot(c9002(:,i));
      title('c9002')
    subplot(7,7,7*k+6)
    plot(c9003(:,i));
      title('c9003')
    subplot(7,7,7*k+7)
    plot(c9004(:,i));
      title('c9004')
end
[value9005,index9005]=max(c9005)
[value9007,index9007]=max(c9007)
[value9008,index9008]=max(c9008)
[value9001,index9001]=max(c9001)
[value9002,index9002]=max(c9002)
[value9003,index9003]=max(c9003)
[value9004,index9004]=max(c9004)
```

Figure 50: MATLAB script used for cross-correlation of the data recorded at the first depth level.

Appendix E

Source offset determination

Source offset was determined based on the scheme shown in Figure 51 in which a pair of source-receiver was plotted in a UTM coordinate system. For vertically drilled borehole all sensors had the same UTM-Northing and Easting the same as the wellhead. The offset of source-receiver was simply calculated by the following Equation 2:

Equation 2

$$offset^2 = (X_{source} - X_{wellhead})^2 + (Y_{source} - Y_{wellhead})^2$$

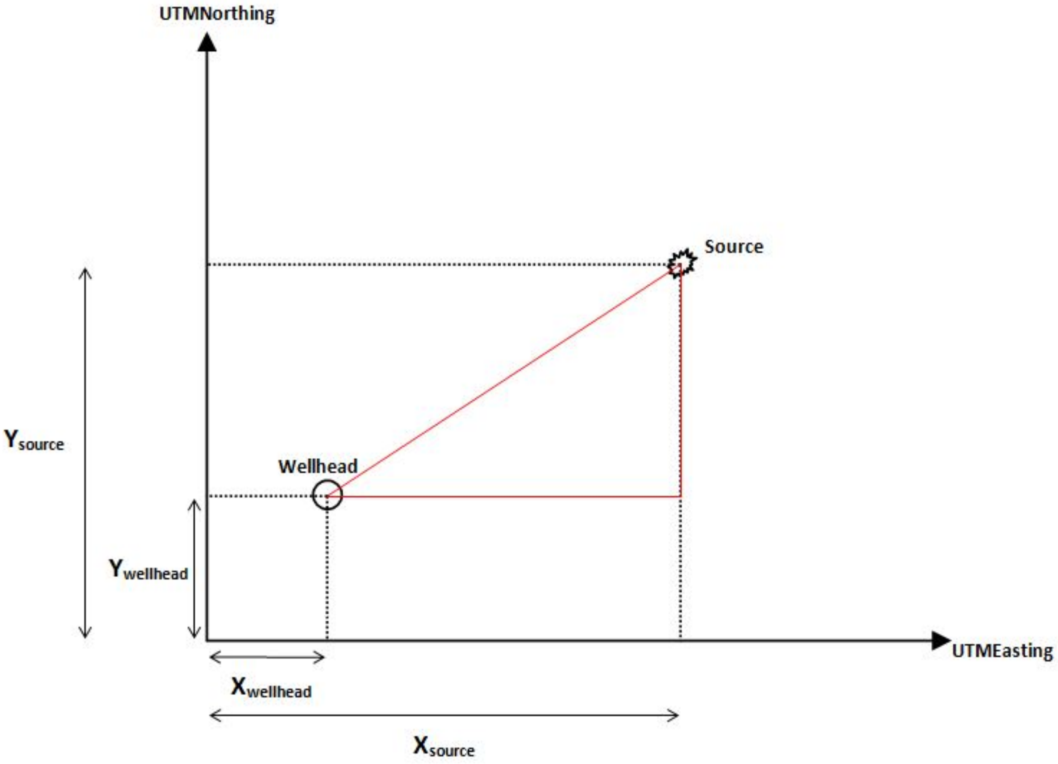

Figure 51: Determination of source-receiver offset.

Shot angle determination

The calculation basics of shot angle can be described by the model shown in Figure 52 which assumes subsurface is horizontal, isotropy, and homogeneous medium where wave is propagating straight and all refractions or multiples are absent. The shot angle was dependent on offset and receiver depth, and was determined by the following Equations 3 and 4.

Equation 3

$$\tan(shot\ angle) = (Z_{source} - Z_{receiver})/offset$$

Equation 4

$$shot\ angle = \tan^{-1}(Z_{source} - Z_{receiver})/offset$$

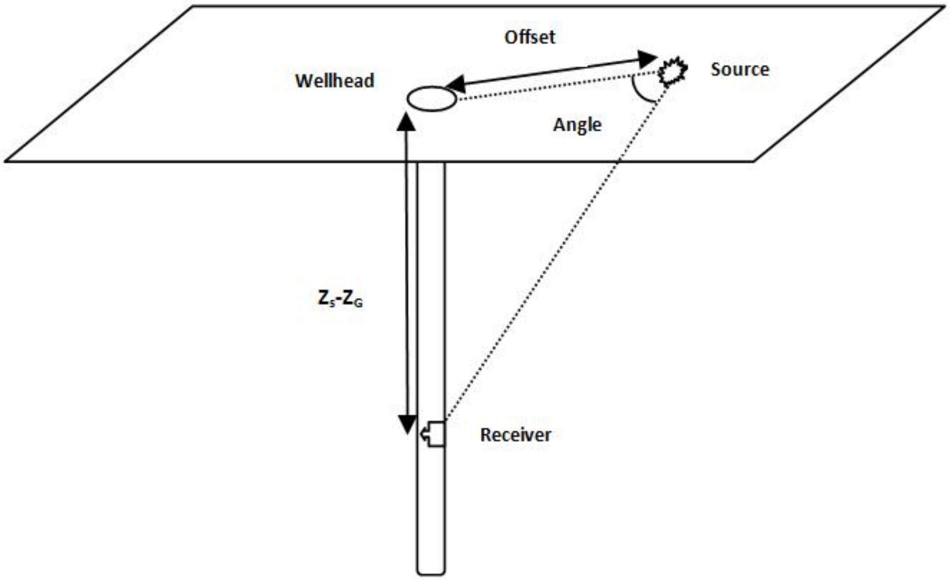

Figure 52: Determination of shot angle.

Real rock velocity determination

Shot angle determines the direction of wave-front propagation if we assume the wave is propagating straight. Figure 53 illustrates the spatial relationship of wave-front propagation and apparent velocity measured from sensors. The model assumes subsurface is horizontal, isotropy and homogeneous medium. Apparent velocity V_a corresponding to the blue line is faster than real wave velocity V_p corresponding to the red. In fact there is a sin relationship between the two types of velocities as the following Equation 5.

Equation 5

$$V_p = V_{apparent} \sin(shot\ angle)$$

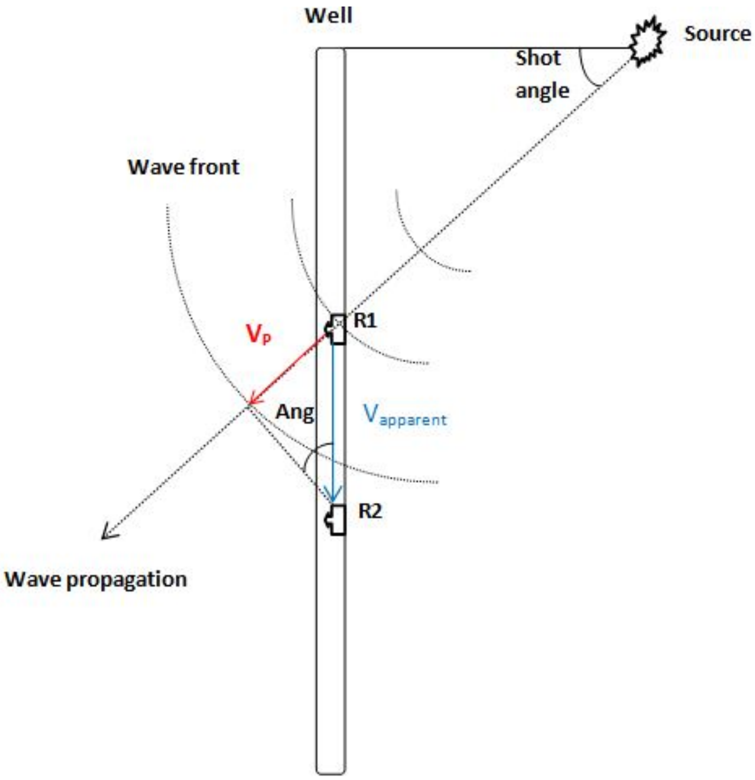

Figure 53: Determination of real rock velocity from apparent velocity (Schematic).

Appendix F

Interval velocity determination

For reflections from a sequence of flat, parallel layers and small offsets, the interval velocity in the nth layer $V_{\text{nth-layer}}$ can be recursively extracted from the stacking velocities V_n, using Dix equation (Equation 6) .

Equation 6

$$V_{nth-layer} = \left(\frac{V_n^2 t_n - V_{n-1}^2 t_{n-1}}{t_n - t_{n-1}}\right)^2$$

, where V_{n-1} and V_n are the stacking velocities from the datum to reflector above and below the layer and t_{n-1} and t_n are reflection arrival times in two way.

Layer thickness determination

The layer thickness can be determined using Equation 7 by simply multiplying interval velocity and one way travel time within that layer.

Equation 7

$$Thickness_{nth-layer} = V_{nth-layer}(t_n - t_{n-1})/2$$

, where $V_{\text{nth-layer}}$ is the interval velocity of the nth layer, and $(t_n\text{-}t_{n-1})/2$ is the one way travel time within that layer.

Appendix G

NMO correction of VSP

Figure 54 shows a single-layer model of borehole seismic waves in horizontal, homogeneous and isotropy medium in which ray paths of seismic waves are straight. Two types of waves are illustrated in this model that are direct arrival and reflected wave. The following Equations 8 and 9 can be obtained from the model:

Equation 8

$$(x-y)^2+d^2=l^2$$

Equation 9

$$(x-2y)^2+z^2=\left(l-\sqrt{(d-z)^2+y^2}\right)^2$$

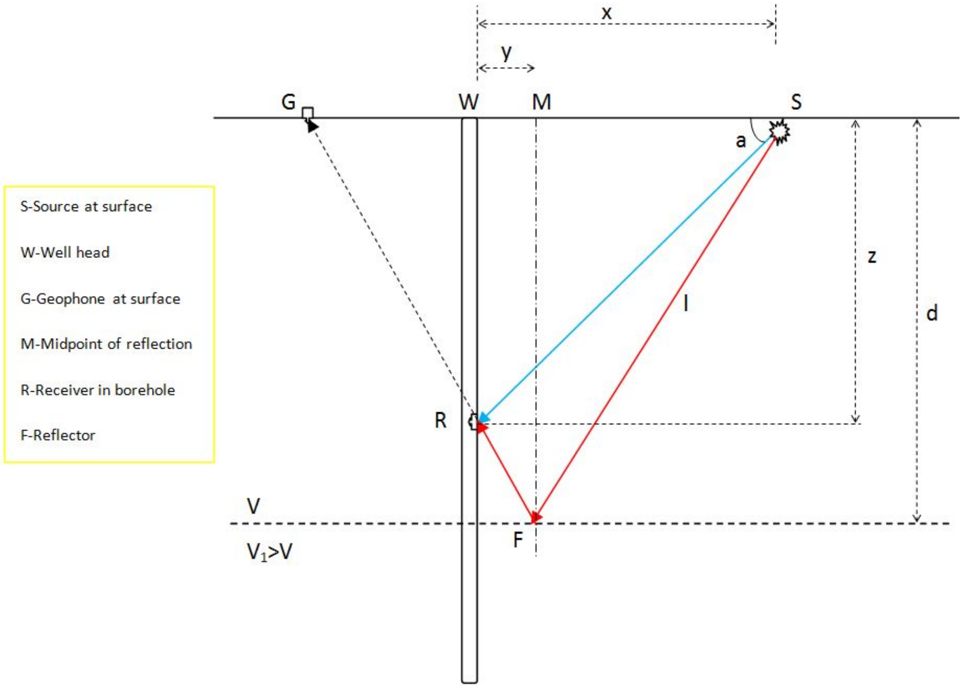

Figure 54: Schematic ray paths in borehole. Blue: direct arrival. Red: Reflection. x: source offset from well head. y: distance between well head and midpoint. z: depth of borehole receiver. d: depth of reflector. l: distance between source and reflection point.

The NMO correction (C_1) needed to convert offset direct arrival time (t_d) to zero-offset direct arrival time (t_{0d}) recorded by the borehole receiver in the model can be calculated as Equation 10 and 11, with t_d determined from picking the first break.

Equation 10

$$t_{od} = t_d \times {}^{z}/_{x}$$

Equation 11

$$C_1 = t_d - t_{od} = t_d(1 - {}^{z}/_{x})$$

The NMO correction (C_2) to convert reflected arrival time (t_r) to zero-offset reflected arrival time (t_{0r}) recorded by the borehole receiver in the model can be calculated as Equation 12 through 14:

Equation 12

$$t_r = \left(1 + \sqrt{(d-z)^2 + y^2}\right)/v$$

Equation 13

$$t_{or} = (2d - z)/v$$

Equation 14

$$C_2 = t_r - t_{or}$$

The total NMO correction needed to convert borehole-recorded reflections to surface-recorded reflections should be the sum of C_1 and C_2.